CONTROLLED INTERFACIAL ADSORPTION OF AUNW ALONG 1-NM WIDE DIPOLE ARRAYS ON LAYERED MATERIALS AND THE CATALYSIS OF SULFIDE OXYGENATION

by

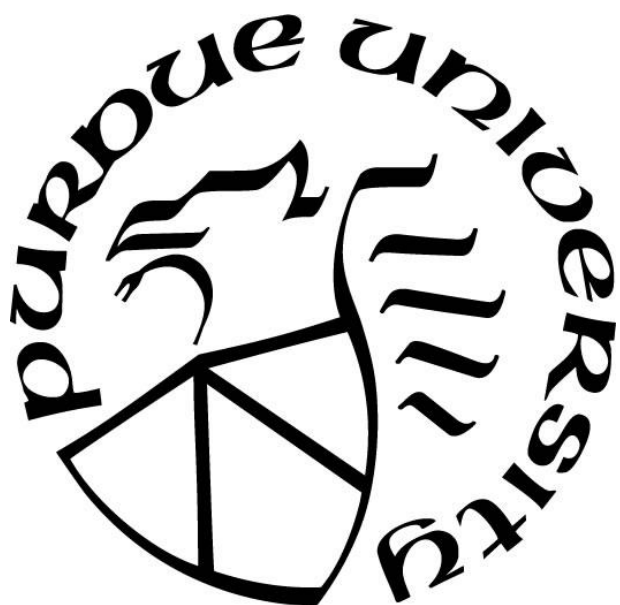**Ashlin G. Porter**

A Dissertation

Submitted to the Faculty of Purdue University

In Partial Fulfillment of the Requirements for the degree of

Doctor of Philosophy

Department of Chemistry

West Lafayette, Indiana

May 2019

THE PURDUE UNIVERSITY GRADUATE SCHOOL
STATEMENT OF COMMITTEE APPROVAL

Dr. Shelley Claridge, Chair

    Department of Chemistry

Dr. Tong Ren

    Department of Chemistry

Dr. Suzanne Bart

    Department of Chemistry

Dr. Mingji Dai

    Department of Chemistry

Approved by:

    Dr. Christine Hrycyna

        Head of the Graduate Program

I dedicate this to my parents Kayleen Logan and Jerre Porter. You both were my first teachers and never let me give up on obtaining my goals and dreams.

ACKNOWLEDGMENTS

My first acknowledgement is to my research advisor, Professor Shelley Claridge. I personally want to thank Dr. Claridge for her patience and guidance throughout graduate school. From her mentorship, I gained scientific and instrumentation knowledge. She also facilitated my development as an effective communicator and writer. I appreciate all the time she spent instructing me. I would also like to express a fond thank you to Dr. Tong Ren for his mentorship, support and advice during graduate school.

Past and current Claridge Group members also contributed to my success in graduate school. I would like to thank past members Dr. Shane Russell and Dr. Jae Jin Bang who provided excellent advice and input. Special thanks to Dr. Russell who introduced me to calculations. I would also like to thank current members Erin Lang, Laura Williams, Jeramiah Bechtold, Tyler Hayes, Tyson Davis, and Anni Shi who I worked with the past several years. I would also like to thank Dr. Eileen Judkins, Dr. Sarah Tyler, Dr. Tim Cook, Dr. Sean Natoli, Dr. Dylan Thompson, Susannah Cox Banziger and Derrick Hall. Special thanks to my undergraduate student Tianhong Ouyang who I have worked closely with these past two years. I thoroughly enjoyed working with Tianhong and wish him best wishes in his future endeavors. Thank you to David McMillin for his technical assistance in the laboratory. I would also like to thank Hanfeng Hu, Dr. Xuemei Liu, Adharsh Raghavan, Dr. Sarju Adhikari, Dr. Bin Liu, and Professor Yu Xia who all were a pleasure to collaborate with throughout my graduate school career.
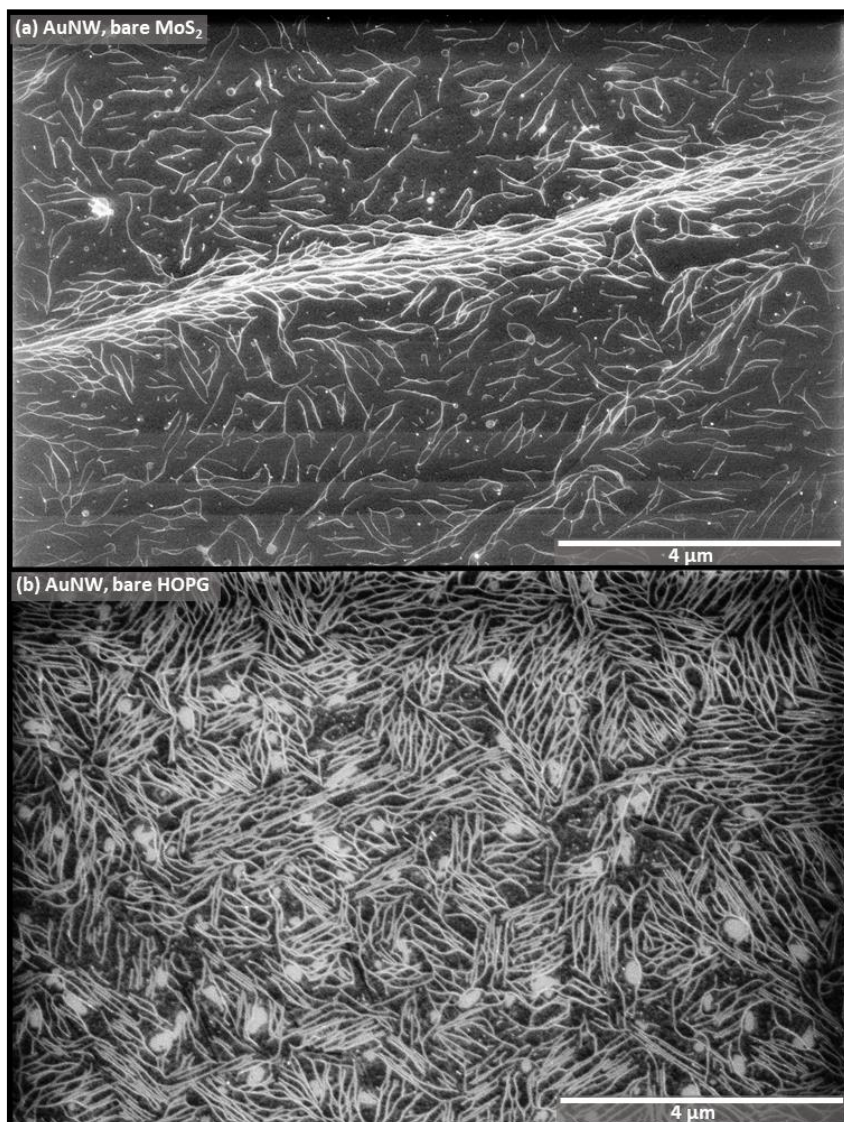
I am sincerely thankful to my mom, dad and sisters, Shelby and Chelsea and her husband Troy Laughlin who provided love, support and encouragement while attending graduate school. I would also like to thank my grandparents, family members and close friends for their support. I would also like to thank Jorge Ramirez Velasco, Neha Agrawal, and Milata Abraham for their friendship during graduate school. Finally, I would like to thank Mark Romanczyk and his family for their love and support.

TABLE OF CONTENTS

(a) AuNW, bare MoS₂

4 µm

(b) AuNW, bare HOPG

4 µm

PUBLICATIONS

Dalton Transactions

ROYAL SOCIETY OF CHEMISTRY

PAPER

Check for updates

Heptamolybdate: a highly active sulfide oxygenation catalyst†‡

Ashlin G. Porter,[a] Hanfeng Hu,[a] Xuemei Liu,[b] Adharsh Raghavan,[a] Sarju Adhikari,[a] Derrick R. Hall,[a] Dylan J. Thompson,[a] Bin Liu,[a] Yu Xia*[a] and Tong Ren ⓘD *[a]

The sulfide oxygenation activities of both heptamolybdate ($[Mo_7O_{24}]^{6-}$, $[1]^{6-}$) and its peroxo adduct $[Mo_7O_{22}(O_2)_2]^{6-}$ ($[2]^{6-}$) were examined in this contribution. $[Mo_7O_{22}(O_2)_2]^{6-}$ was prepared in a yield of 65% from $(NH_4)_6[Mo_7O_{24}]$ (**1a**) upon treatment of 10 equiv. of H_2O_2 and structurally identified through single crystal X-ray diffraction study. $(nBu_4N)_6[Mo_7O_{22}(O_2)_2]$ (**2b**) is an efficient catalyst for the sequential oxygenation of methyl phenyl sulfide (MPS) by H_2O_2 to the corresponding sulfoxide and subsequently sulfone with a 100% utility of H_2O_2. Surprisingly, $(nBu_4N)_6[Mo_7O_{24}]$ (**1b**) is a significantly faster catalyst than **2b** for MPS oxygenation under identical conditions. The pseudo-first order k_{cat} constants from initial rate kinetics are 54 M^{-1} s^{-1} and 19 M^{-1} s^{-1} for **1b** and **2b**, respectively. Electrospray ionization mass spectrometry (ESI-MS) investigation of **1b** under the catalytic reaction conditions revealed that $[Mo_2O_{11}]^{2-}$ is likely the main active species in sulfide oxygenation by H_2O_2.

Introduction

The oxygenation of organic sulfides is a transformation key to medicinal chemistry,[1] petroleum desulfurization,[2] and nerve agent detoxification.[3–5] Highly relevant to the latter two applications are both the reaction rates and the use of inexpensive oxidants and catalysts. Hydrogen peroxide and *tert*-butyl hydroperoxide (TBHP) are among the desired oxidants because of their low costs and environmentally friendly nature.[6] Hydrogen peroxide is the most studied oxidant, and can be activated with a variety of transition metal based homogeneous catalysts. Among a plethora of catalysts reported,[7] homo- and hetero-polyoxometalates (POMs) stand out due to both the ease of preparation and their chemical robustness.[8–10] Recent examples of sulfide oxygenation catalyzed by both POMs and related species include the degradation of mustard agent simulants,[11–13] oxygenation of thioanisole with $(Bmim)_2[Mo_6O_{19}]$ (Bmim = 1-butyl-3-methylimidazolium),[14] conversion of 2-chloroethyl ethyl sulfide to its sulfoxide using $H_3PW_{12}O_{40}$ embedded in a MOF,[15] and the selective formation of sulfoxide as the precursor of vinyl glycine.[16] Contributions from our laboratory include the early demonstration of excellent chemical selecti-

vity and efficient use of H_2O_2 in sulfide oxygenation using $[\gamma\text{-}SiW_{10}O_{34}(H_2O)_2]^{4-}$,[17] its subsequent heterogenization in amine functionalized MCM-41,[18] and the recent discovery of peroxo-dimolybdate as a highly efficient catalyst.[19]

Heptamolybdate, $[Mo_7O_{24}]^{6-}$ (also known as paramolybdate), is the lowest member of the isopolymolybdate family,[20] and its ammonium salt $((NH_4)_6[Mo_7O_{24}]$, **1a**) is commercially available and inexpensive. While heteropolyoxometallates have attracted intense interest as oxygenation catalysts,[9,10] the role of heptamolybdate as an oxygenation catalyst has been sparingly explored. Noteworthy among a handful of examples using $[Mo_7O_{24}]^{6-}$ as a catalyst are the olefin epoxidation and alcohol oxidation by H_2O_2[21] and the conversion of dibenzothiophene and derivatives to corresponding sulfones by H_2O_2 in ionic liquid.[22] Also noteworthy is the ability of heptamolybdate to promote hydrolysis of phosphoesters.[23] Reported herein are the preparation and structural characterization of a di-peroxo derivative of heptamolybdate, $[Mo_7O_{22}(O_2)_2]^{6-}$ (**2**[6-]), and its activity in promoting sulfide oxygenation by H_2O_2. It was discovered in the process of performing control experiments that the parent heptamolybdate is a far more active catalyst. The reactivity scope, catalytic rates and the nature of the active species under the catalytic conditions were carefully examined.

[a]Department of Chemistry, Purdue University, 560 Oval Drive, West Lafayette, IN 47906, USA. E-mail: yxia@purdue.edu, tren@purdue.edu
[b]College of Chemistry and Chemical Engineering, Xi'an Shiyou University, Xi'an, China

Results and discussion

Synthesis and structural identification of $[Mo_7O_{22}(O_2)_2]^-$ (**2**[6-])

Curious about the nature of the active species in the aforementioned olefin epoxidation and alcohol oxidation reactions cata-

LIST OF TABLES

LIST OF FIGURES

ABSTRACT

Author: Porter, Ashlin, G. PhD
Institution: Purdue University
Degree Received: May 2019
Title: Controlled Interfacial Adsorption of AuNW Along 1-nm Wide Dipole Arrays on Layered
   Materials and the Catalysis of Sulfide Oxygenation
Committee Chair: Shelley Claridge

Controlling the surface chemistry of 2D materials is critical for the development of next generation applications including nanoelectronics and organic photovoltaics (OPVs). Further, next generation nanoelectronics devices require very specific 2D patterns of conductors and insulators with prescribed connectivity and repeating patterns less than 10 nm. However, both top-down and bottom-up approaches currently used lack the ability to pattern materials with sub 10-nm precision over large scales. Nevertheless, a class of monolayer chemistry offers a way to solve this problem through controlled long-range ordering with superior sub-10 nm patterning resolution. Graphene is most often functionalized noncovalently, which preserves most of its intrinsic properties (*i.e.,* electronic conductivity) and allows spatial modulation of the surface.[1–5] Phospholipids such as 1,2-bis(10,12-tricsadiynoyl)-*sn*-glycero-3-phosphoethanolamine (diyne PE) form lying down lamellar phases on graphene where both the hydrophilic head and hydrophobic tail are exposed to the interface and resemble a repeating cross section of the cell membrane.[6,7] Phospholipid is made up of a complex headgroup structure and strong headgroup dipole which allows for a diverse range of chemistry and docking of objects to occur at the nonpolar membrane, these principals are equally as important at the nonpolar interface of 2D materials.[8–10] A key component in the development of nanoelectronics is the integration of inorganic nanocrystals such as nanowires into materials at the wafer scale.[11] Nanocrystals can be integrated into materials through templated growth on to surface of interest as well as through assembly processes (i.e. interfacial adsorption).

In this work, I have demonstrated that gold nanowires (AuNWs) can be templated on striped phospholipid monolayers, which have an orientable headgroup dipoles that can order and straighten flexible 2-nm diameter AuNWs with wire lengths of ~1 µm. While AuNWs in solution experience bundling effects due to depletion attraction interactions, wires adsorb to the surface in a well separated fashion with wire-wire distances (e.g. 14 or 21 nm) matching multiples of the PE template pitch. This suggests repulsive interactions between wires upon interaction with dipole

arrays on the surface. Although the reaction and templating of AuNWs is completed in a nonpolar environment (cyclohexane), the ordering of wires varies based on the hydration of the PE template in the presence of excess oleylamine, which forms hemicylindrical micelles around the hydrated headgroups protecting the polar environment. Results suggest that PE template experience membrane-mimetic dipole orientation behaviors, which in turn influences the orientation and ordering of objects in a nonpolar environment.

Another promising material for bottom-up device applications is MoS_2 substrates due to their useful electronic properties.[12] However, being able to control the surface chemistry of different materials, like MoS_2, is relatively understudied, resulting in very limited examples of MoS_2 substrates used in bottom-up approaches for nanoelectronics devices. Diyne PE templates adsorb on to MoS_2 in an edge-on conformation in which the alkyl tails stack on top of each other increasing the overall stability of the monolayer.[13] A decrease in lateral spacing results in high local concentrations of orientable headgroups dipoles along with stacked tails which could affect the interactions and adsorption of inorganic materials (i.e. AuNW) at the interface.

Here, I show that both diyne PE/HOPG and diyne PE/MoS_2 substrates can template AuNW of various lengths with long range ordering over areas up to 100 μm^2. Wires on both substrates experience repulsive interactions upon contact with the headgroup dipole arrays resulting in wire-wire distances greater than the template pitch (7 nm). As the wire length is shortened the measured distance between wires become smaller eventually resulting in tight packed ribbon phases. Wires within these ribbon phases have wire-wire distances equal to the template. Ribbon phases occur on diyne PE/HOPG substrates when the wire length is ~50 nm, whereas wire below ~600 nm produce ribbon phases on diyne PE/MoS_2 substrates.

Another important aspect to future scientific development is the catalysis of organic reactions, specifically oxygenation of organic sulfides. Sulfide oxygenation is important for applications such as medicinal chemistry,[14] petroleum desulfurization,[15] and nerve agent detoxification.[16–18] Both reaction rates and the use of inexpensive oxidants and catalysts are important for practical applications. Hydrogen peroxide and *tert*-butyl hydroperoxide are ideal oxidants due to being cost efficient and environmentally friendly. Hydrogen peroxide can be activated through transition metal base homogeneous catalysts. Some of the most common catalysts are homo- and hetero-polyoxometalates (POMs) due their chemical robustness.[19–21] Heptamolybdate [Mo_7O_{24}]$^{6-}$ is a member of the isopolymolybdate family and its ammonium salt is commercially available and low

in cost.[22] Heteropolyoxometalates have been widely studied as a catalyst for oxygenation reactions whereas heptamolybdate has been rarely studied in oxygenation reactions.[20,21]

Here I report sulfide oxygenation activity of both heptamolybdate and its peroxo derivate $[Mo_7O_{22}(O_2)_2]^{6-}$. Sulfide oxygenation of methyl phenyl sulfide (MPS) by H_2O_2 to sulfoxide and sulfone occurs rapidly with 100 % utility of H_2O_2 in the presence of $[Mo_7O_{22}(O_2)_2]^{6-}$, suggesting the peroxo adduct is an efficient catalyst. However, heptamolybdate is a faster catalyst compared to $[Mo_7O_{22}(O_2)_2]^{6-}$ for MPS oxygenation and all other sulfides tested under identical conditions. Pseudo-first order k_{cat} constants from initial rate kinetics show that $[Mo_7O_{24}]^{6-}$ catalyzes sulfide oxygenation faster. The significant difference in the k_{cat} suggests differences in the active catalytic species, which was characterized by both UV-Vis and electrospray ionization mass spectrometry. ESI-MS suggest that the active intermediate of $[Mo_7O_{24}]^{6-}$ under catalytic reaction conditions for sulfide oxygenation by H_2O_2 is $[Mo_2O_{11}]^{2-}$. These results show that heptamolybdate is a highly efficient catalyst for H_2O_2 oxygenation of organic sulfides.

CHAPTER 1.   INTRODUCTION TO THE DEVELOPMENT OF BIO INSPIRED NONCOVALENT MONOLAYERS ON LAYERED MATERIALS USED FOR INTERFACIAL ADSORPTION OF INORGANIC NANOCRYSTALS

Controlling the surface chemistry of 2D materials is critical for the development of next generation applications including both nanoelectronics and organic photovoltaics (OPV). Further, next generation nanoelectronics devices require very specific 2D patterns of conductors and insulators with prescribed connectivity and repeating patterns less than 10 nm. Nanoelectronics fabrication is typically performed using a top-down approach where the pattern is written directly onto or transferred to a substrate using optical and electron beam lithographic methods. Microscopic or nanoscopic patterns are engraved by etching and deposition processes.[23] Nanofabrication techniques such as photolithography (sub-20 nm resolution)[24], scanning beam lithography (20 nm) and scanning probe lithography (1 nm) are common tools used for patterning nanoelectronics.[25] A drawback for photolithographic and scanning beam lithographic methods is the lack of resolution below 10 nm, hindering its capabilities to be used for next generation devices.[26] While scanning probe lithography such as STM has 1 nm resolution, it only produces individual nano-structures and remains impractical for micro-scale devices.[26] Controlling the nanoscopic patterning with high fidelity over larger length scales is a limitation for top-down techniques.

1.1   Bottom-up approaches used for patterning

Bottom-up approaches, which rely on interactions between building blocks of molecules to assemble into nano and microstructures, have shown great promise.[27] Self-assembly processes are an example of a bottom-up approach that allows for patterning materials over large length scale with sub-10nm precision. Previous studies have shown that self-assembled monolayers (SAMs) of alkanethiols deposited on Au (111) via micro-contact printing or dip pen lithography can be used for the controlled templating of a variety of materials.[28,29] These structures include mineral crystals and soft matter at the sub µm scale.[28,29] While this technique is cost effective and allows for patterning of materials at the sub µm scale, improvements are still required. Both approaches (*i.e.,* top-down and bottom-up) lack the ability to pattern materials with sub 10-nm precision over large

scales. Furthermore, this downfall poses a difficult challenge in surface science that must be further investigated to develop next generation nanoelectronics and OPV devices. A class of monolayer chemistry (i.e. lying down monolayers) offers a way to solve this problem through controlled long-range ordering with superior sub-10 nm patterning resolution.

1.2   Noncovalent functionalization of 2D materials

Graphene is most often functionalized noncovalently, which preserves most of its intrinsic properties (*i.e.,* electronic conductivity) and allows spatial modulation of the surface.[1–4] Two classes of molecules commonly used for noncovalent functionalization are long alkanes, alkane derivatives,[5,30] and planar aromatic hydrocarbons (pyrenes and anthracene).[1,31] Noncovalent monolayers are commonly formed by spin coating or drop casting of dilute solution. Another method commonly used is the transfer of ordered molecular films from an air-water interface to a solid substrate by vertical dipping (Langmuir-Blodgett) or horizontal dipping (Langmuir-Schaefer).[32,33] Methods like Langmuir-Schaefer transfer are often utilized in the monolayer formation of long alkanes with functionalized headgroups as a means of controlling long-range ordering with sub 10-nm chemical patterning device applications such as nanoelectronics and OPVs.[6,7,34,35]

1.3   Functionalization of 2D materials with lying-down phases in the efforts to template objects at the interface

Long functionalized alkanes, such as octadecylamine, are known to form striped lamellar phases on highly oriented pyrolytic graphite (HOPG) due to the epitaxy between graphene lattice and the alkyl zig-zag.[36,37] Monolayers of octadecylamine can act as a nanotemplate for the immobilization of DNA.[36,38,39] Whereas reports show that 1-dodecanthiol (C12SH) monolayers can be used for the synthesis and assembly of nickel particles on HOPG as a means of ordering arrays of nanoparticles.[40] Furthermore, noncovalent functionalization of graphene with lying down molecules create sub 10 nm periodicities, which can be useful for patterning objects on layered materials.[41] However, the overall robustness of the monolayer is a concern due to noncovalent functionality of the monolayer but can be overcome by using monolayers with ene-yne polymer backbone.[13,34,42–44,45]

1.4   Functionalization of Graphene with lying down monolayers of diynoic acids

Long chain functionalized alkanes such as diynoic acids (*i.e.,* 10,12 pentacosadiynoic acid (10-12 PCDA)) form noncovalent monolayers through a self-assembly process in a head-to-head lying-down phase on layered materials such as graphite.[6,7] Stabilization is due to an epitaxy match between the alkyl zig-zag, the hexagonal graphite lattice and hydrogen-bonded carboxylic acid dimers between adjacent row of headgroups.[7,46–48] These types of assemblies with polar headgroups are arranged in a lamellar structure with a 6 nm pitch. Further, molecules with an internal diyne can be photopolymerized by using UV irradiation.[49–51] The polymerization of diyne creates an ene-yne polymer backbone increasing the overall stability of the monolayer towards solvothermal processing.[34,44]

1.5   Monolayer interactions with their environment

In order for 10-12 PCDA monolayers to be used in patterning materials at the interface, the functionalized headgroups must be accessible to the environment, which implies there must be some range of motion of the headgroup.[41] Studies performed by Whitesides and others have shown differences in the ionization of functionalized groups at the polar-nonpolar interface of the periphery of a standing phase self-assembled monolayer.[52–54] Measurements show that for carboxylic acids $pK_{1/2}$ shifts up by at least 2 pH units compared to the solution pK_a.[41] These results support the idea that the nonpolar interior has a limited ability to stabilize the charged form of the functional headgroup. Similarly laying down monolayers of PCDA on graphite experience a $pK_{1/2}$ at 9.5, which is a 5-unit shift in comparison to acetic acid in solution.[45,35] PCDA monolayers remain protonated throughout most of the pH scale limiting its capabilities to acts as templates for interacting with objects at the interface due to the headgroups limited ionization abilities.[34] However phospholipids within the cell membrane routinely promotes weak acid base chemistry at the nonpolar interface and are known to form similar lying down monolayers on layer materials suggesting an alternative route to templating materials at the interface.[8,9]
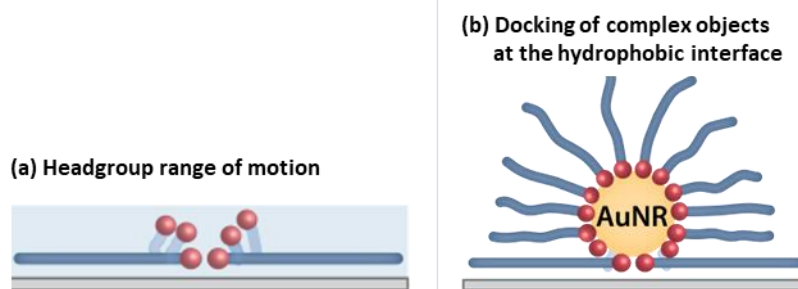
Figure 1.1 (a) Headgroup range of motion is required for the use of noncovalent monolayers for nanoelectronics applications. (b) Illustration of docking of complex objects such as AuNWs at the hydrophobic interface.

1.6   Drawing inspiration from biology in the development of monolayers

The phospholipid bilayer of the cell membrane is a made up of hundreds of structurally different lipids with a chemical orthogonality of approximately 10 nm. The complex phospholipid structure helps mediate transitions between the nonpolar interior and the polar periphery within the cell membrane.[8,9] Nonpolar tails are made up of long chain alkanes followed by a polar headgroup comprised of a polar ester linkage, a phosphate group and a flexible alkyl linkage that terminates with an amine functionality. The headgroup is asymmetric due to the 3-carbon glycerol backbone which shifts in position allowing for the orientation of the headgroup (i.e. phosphate and other headgroup functional groups). Phospholipids with a zwitterionic headgroups have a strong dipole (>20 D) which can reorient in response to electric fields modulating the membrane fluidity and interactions (i.e. docking with complex objects) within the environment.[8–10] These local dipoles have been shown to be important in binding inorganic nanocrystals to lipid bilayers.[55] Overall, the complex headgroup structure and strong headgroup dipole allows for a diverse range of chemistry and docking of objects to occur at the nonpolar membrane, these principals could be envisioned to be useful at nonpolar interface of 2D materials.
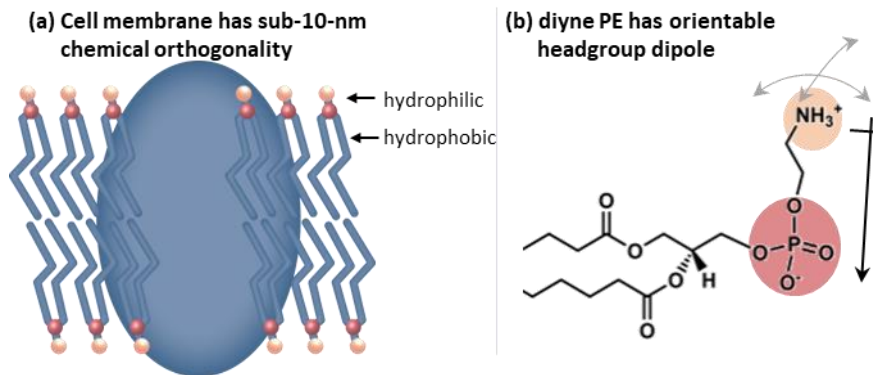
Figure 1.2 (a) Illustration of sub-10-nm chemical orthogonality in the cell membrane. (b) Phospholipid structure and the orientable headgroup dipole.

1.7 Functionalization of graphene with phospholipids

Lying down lamellar phases of phospholipids where both the hydrophilic head and hydrophobic tail are exposed to the interface resemble a repeating cross section of the cell membrane.[46] This lamellar structure creates sub-10 nm chemical patterns (similar to PDCA monolayers) that are ideal for the templating of inorganic materials at length scales compatible for nanoelectronics devices. Phospholipid monolayers are comprised of 1-nm wide functional headgroup rows followed by a 5 nm pitch of nonpolar tails. Previous work done by our group has shown through contact angle measurements that the primary amine of phosphoethanolamine (diyne PE) does not undergo a $pK_{1/2}$ shift.[45] Conversely, the phosphate does experience a $pK_{1/2}$ shift of 5 pH units. Molecular modeling and contact angle measurements suggest that the primary amine protrudes a few angstroms away from the interface while phosphate sits at the nonpolar periphery.[45] The protruding amines solution ionization behavior remains the same which is critical in the development of templating complex objects such as nanowires at the interface.

1.8 Controlling monolayer structure and robustness

Modifications to the phospholipid architecture, such as the head group size and charge, tail length, and diyne position, effect the overall striped phase structure.[41] These modification result in differences in pitch, stability, chemical functionality and ability to act as ligands for crystallization and templating of inorganic materials at the interface. Another set of parameters of laying down monolayers which are critical for the patterning of materials for device applications are long range

ordering, overall stability, and nanoscopic resolution. Monolayers of diyne PE can produce domains up to tens of microns long by using ideal transfer conditions and thermal heating during the transfer process.[44] Domains of this size are stable towards a range of solvents from toluene to water, suggesting diyne PE films can withstand solution processing steps. Additionally, diyne PE domains provide the appropriate scalability and resolution required for device applications.

1.9   Templating inorganic materials

A key component in the development of nanoelectronics is the integration of inorganic nanocrystals such as nanowires into materials at a wafer scale.[11] Nanocrystals can be integrated into materials through templated growth on to surface of interest as well as through assembly processes (i.e. interfacial adsorption). Patterning inorganic crystals through interfacial adsorption is advantageous for several reasons such as larger set of synthetic protocols available to use (i.e. synthetic procedures with elevated temperatures) and higher degree of control over diameter, length, and ligand shell of the inorganic nanocrystal. Lying down monolayer chemistry is an ideal candidate for improving the controlled interfacial adsorption of inorganic nanocrystals at the wafer scale.

1.10   Solution phase colloidal nanocrystal growth

Colloidal nanocrystal assembly has been widely studied in the literature as a means of organizing functional inorganic materials (*i.e.,* metals or semiconductors) with three-dimensional precision (2-20 nm length scale) at resolution limits comparable to top-down approaches.[11] Decomposition of precursors in the presence of surfactants is effective at controlling the size and shape uniformity of the nanocrystal.[56] One-dimensional structures, such as nanowires, are of interest due to their unique electrical, optical, and magnetic properties.[57,58] Some of the most common core materials used in one-dimensional structures are Au, Ag, CdSe, CdS, CdTe.[11]

1.11   Synthesis of gold nanowires

Gold nanowires (AuNWs) are of great interest for nanoscience and nanotechnology applications due to their high surface area and quantum-confined diameters. AuNWs have been used for Surface-Enhanced Raman Scattering (SERS) substrates, sensors, and transparent electronics.[59–62] There are several examples of organic capped AuNW synthesis that have diameters as small as 2 nm and wire lengths of up to several microns.[57,63–65] AuNWs are produced through the reduction of Au^{3+} ($HAuCl_3 \cdot 3H_2O$) to Au^0 in the presence of a reducing agent (triisopropylsilane) and oleylamine which also acts as the capping ligand.[57,63,64]

1.12   Nanocrystal surface ligands have similarities to noncovalent monolayers

Nanocrystal surface ligands such as oleylamine are similar in both structure and chain length to molecules used in noncovalent monolayers which could be advantageous in controlled templating of AuNW on noncovalent monolayers. The capping ligands are important in stabilizing the wire post- synthesis and the protective layer around the nanocrystal is similar to organic-inorganic interfaces of self-assembled surfactants on crystalline surfaces such as thiols on gold.[66–68] Oleylamine ligands form an inverted micelle around the surface, whereas excess oleylamine molecules interdigitate between adjacent wires. This phenomenon results in wires packing into a hexagonal array with an average wire-wire distance of around 5.5-9.5 nm, matching that of phospholipid template pitch.[57,61,63,64,69]
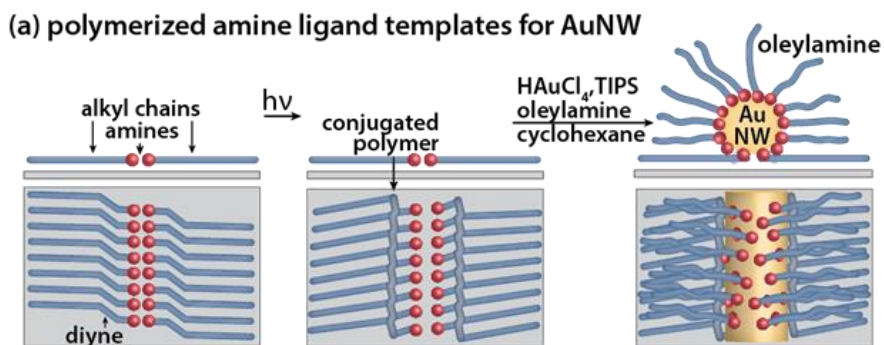
Figure 1.3 Illustration of interfacial adsorption of AuNW on noncovalent monolayers.

1.13   MoS$_2$ is another promising material for nanoelectronics

Another promising material for bottom-up device applications is MoS$_2$ substrates due to their useful electronic properties.[12] However, being able to control the surface chemistry of different materials, like MoS$_2$, is relatively understudied, resulting in very limited examples of MoS$_2$ substrates used in bottom-up approaches for nanoelectronics devices.[70,71] Alkyl chain adsorption enthalpy is lower on MoS$_2$ compared to graphite due to a greater mismatch in the MoS$_2$ lattice structure (3.16 Å) and C-C bond length (2.54 Å) in relation to graphite lattice (2.46 Å).[13] Noncovalent monolayers bound weakly to the surface are more instable towards solution processing steps limiting their capabilities to be used in practical applications.[72] Previously, our group has observed that diyne PE templates adsorb on to MoS$_2$ in an edge-on conformation in which the alkyl tails stack on top of each other. Edge-on stacking increases the stability of the monolayer due to chain-chain interactions between the two layers, resulting in a more resistant template towards solution processing. Edge-on adsorption results in half the distance in the lateral spacing between adjacent headgroups compared to the lateral spacing of diyne PE on graphite.[13] A decrease in lateral spacing results in high local concentrations of orientable headgroups dipoles along with stacked tails could affect the interactions and adsorption of inorganic materials (i.e. AuNW) at the interface.

1.14   Conclusion

One of the main limiting factors hindering the development of next generation nanoelectronics is the patterning of materials at the sub-10 nm scale in scalable and in cost-effective means. Many different approaches have been developed and used such as bottom-up and top-down approaches, however both techniques have limitations. One promising approach is functionalization of 2D materials such as graphene or MoS$_2$ as a means of templating materials at interface. A class of phospholipids with an internal diyne produce striped phases with patterns of 6 nm and domains sizes of up several microns long which is essential for practical application. This is an advantage over most of the literature on 2D monolayers which focus on relatively small areas of the surfaces. Being able to control the interfacial adsorption of inorganic materials to surfaces is an important challenge in device applications. However biological systems routinely dock complex objects at the cell membrane surfaces via phospholipid. Similarly lying down

monolayers of phospholipids on layered materials also have capabilities to control the assembly of complex objects such as AuNW.

CHAPTER 2.   1-NM-WIDE HYDRATED DIPOLE ARRAYS REGULATE AUNW ASSEMBLY ON STRIPED MONOLAYERS IN NONPOLAR SOLVENT

A version of this chapter has been submitted for publication in *Chem*

2.1   Introduction

Nanoscale patterning of interfaces with inorganic nanostructures is increasingly important in device fabrication and other applications.[11,73–84] Controlling interfacial adsorption of anisotropic nanostructures, which can become trapped in undesired binding geometries (e.g. a rod adsorbing misaligned with a striped template), remains a significant challenge in bottom-up approaches to device fabrication. However, biological systems routinely control docking of complex objects at the cell membrane surface, utilizing phospholipids and other membrane constituents.[9] For phospholipids, strong dipoles (~25 D) in zwitterionic headgroups can reorient in response to local electric fields, modulating membrane fluidity and directing interactions with the environment. [8,10] Local dipole array polarization has been shown to impact binding of inorganic nanocrystals to lipid bilayers in aqueous environments.[55]

Interestingly, 2D materials are often functionalized noncovalently[2,41,85] with motifs including striped phases of horizontally-oriented amphiphiles.[1,2,37,86] Striped phases resemble repeating cross-sections of the cell membrane,[41] suggesting a mechanism for directing orientation of anisotropic objects, such as rods, at the interface (Figure 2.1). Diynes including 10,12-pentacosadiynoic acid (10,12-PCD-COOH) assemble into lying-down lamellar phases with paired headgroups on highly oriented pyrolytic graphite (HOPG) and graphene, creating 1-nm-wide stripes of headgroups with pitches (ca. 5–7 nm) prescribed by alkyl chain length.[6,7,47,87–90] Photopolymerization of the diyne produces an ene-yne polymer backbone, which has been extensively utilized in molecular electronics studies,[6,87,91] but also stabilizes the monolayer against solvent exchange.[34,35,44,45,84,92]
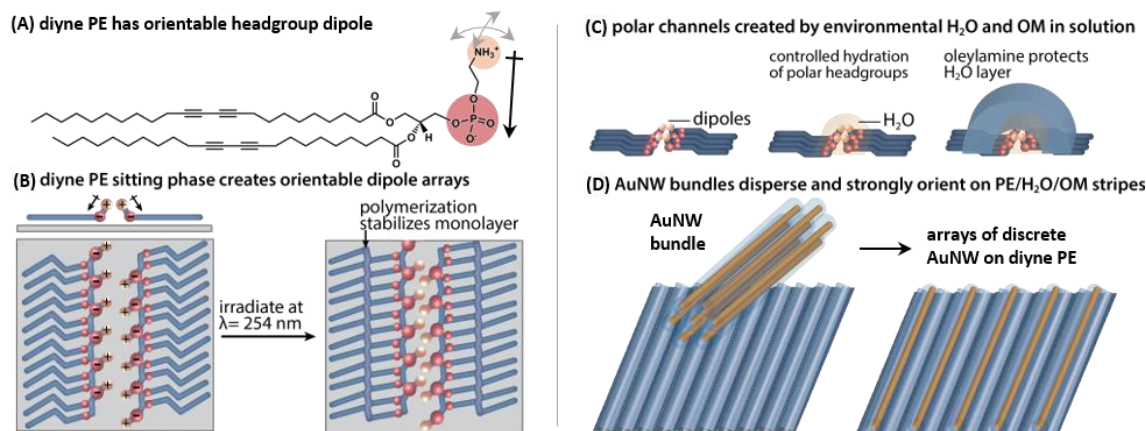
Figure 2.1 Illustration of AuNW assembly on phospholipid striped phases. (a) Structure of diyne PE, illustrating flexibly oriented dipole. (b) Schematic of sitting phase of diyne PE and photopolymerization of diyne to stabilize noncovalently adsorbed monolayer. (c) Illustration of environmental hydration to create water layer around PE headgroups, and inverse micelle of oleylamine that forms around water layer in AuNW growth solution. (d) Illustration of well-separated AuNW arrays that form on striped diyne PE templates from AuNWs that form bundles in solution.

Recently, we have found that in striped monolayers of diyne phospholipids (e.g. diyne phosphoethanolamine, Figure 2.1a), the terminal ammonium functional group protrudes slightly from the surface, forming a 'sitting' geometry (Figure 2.1b).[45] This protrusion means that the zwitterionic phosphate/ammonium headgroup can adopt a variety of orientations, forming orientable 1D dipole arrays. Aligned molecular domains can be >10 μm in edge length, depending on molecular structure and monolayer preparation methods.[44,93] Such arrays suggest the possibility of controlled interactions with inorganic nanostructures in the environment, particularly in polarizing anisotropic structures such as wires to impact orientation and alignment at an interface.

Here, we show that striped phases of phospholipids with 1-nm-wide rows of orientable headgroup dipoles can precisely orient and order narrow, flexible gold wires (Au diameter 1.5–2 nm), with lengths (>1 μm) substantially exceeding the template pitch (~6.8 nm). Arrays created in this way can extending over areas >100 μm^2. In the nonpolar solvent (cyclohexane) used here, ordering of AuNWs on the template depends on template hydration (Figure 2.1c, middle), as well as the presence of excess oleylamine, which forms micelles on the striped surface (Figure 2.1c, right) The protected polar environment immediately surrounding the headgroups would provide a reasonable means of enabling collective dipole orientation phenomena similar to those in the

membrane periphery. Overall, these findings suggest new bioinspired principles for orienting and ordering long, flexible nanoscale objects over microscale areas (Figure 2.1d), based on collective molecular interactions in a nanostructured template.

2.2   Results and Discussion

2.2.1   AuNW synthesis and assembly on striped diyne PE templates

Striped templates of 1,2-bis(10,12-tricosadiynoyl)-sn-glycero-3-phosphoethanolamine (diyne PE) were prepared via Langmuir-Schaefer (LS) conversion,[7,34,44,45,87,94] using a thermally regulated transfer stage we have reported previously[44] to achieve areas with typical ordered domain edge lengths > 1 μm. Expected lamellar periodicities for such monolayers are ~6.8 nm (Figure 2.2a), consistent with periodic structures observed in AFM images after transfer (Figure 2.2b).
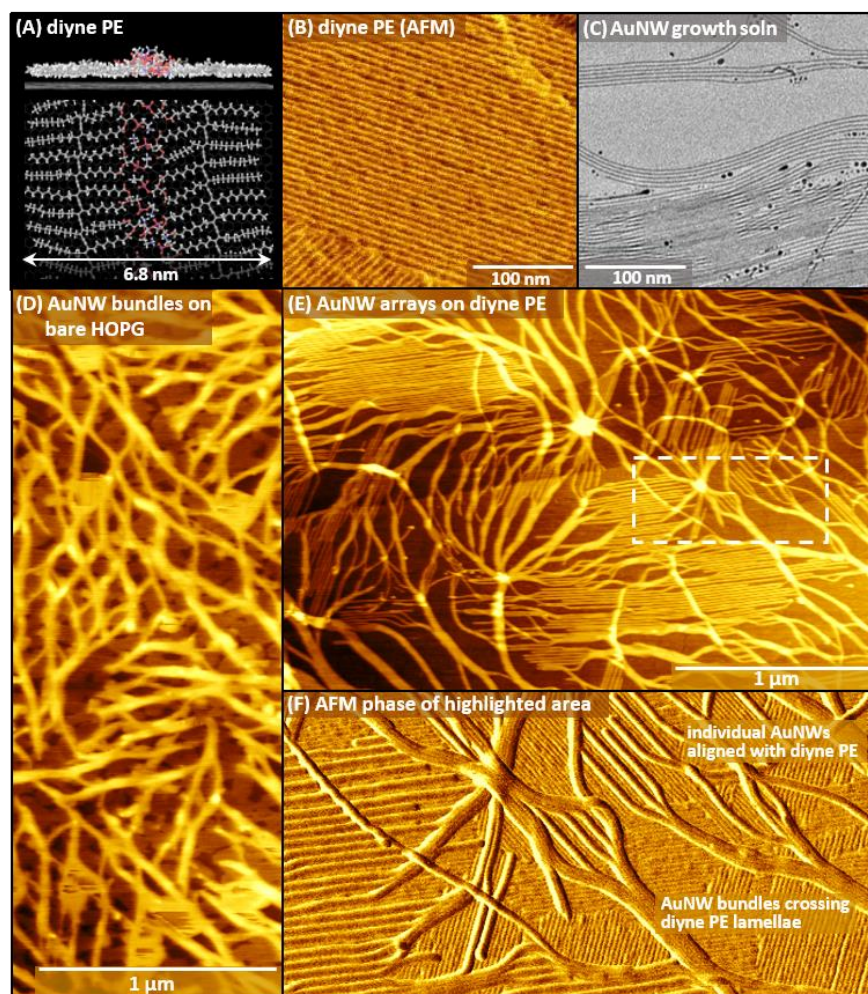
Figure 2.2 Images of striped phase and AuNW structures, and templated AuNW assembly.(a) Side and top view molecular models and (b) AFM phase image of diyne PE lamellar phase on HOPG. (c) TEM image of AuNW growth solution comprising both wires and spheres. (d) AuNW bundles deposited on HOPG. (e,f) AuNW bundles and arrays of discrete AuNW on diyne PE template.

AuNWs were grown using a variation on literature procedure for ultranarrow AuNW synthesis,[57,63,64] using solutions of $HAuCl_4 \cdot 3H_2O$, triisopropylsilane (TIPS), and oleylamine (OM) in cyclohexane. Solutions were aged for 12 h to allow for AuNW growth (Figure 2.2c, see Experimental Methods for more detailed synthetic protocols). Similar procedures (typically using hexane as a solvent) have been shown previously to result in growth of AuNWs with diameters of 1.5–2 nm similar to those shown here, which form hexagonally-packed bundles in solution based on depletion attraction interactions between AuNW ligand shells.[57,61,63,64,69] Lengths can be

modified through choice of concentration or growth times; unless otherwise stated, AuNWs in templated deposition experiments reported here have average lengths of 902 ± 336 nm.

Bare HOPG substrates exposed to AuNW solution for 2 h exhibit bundles of wires (Figure 2.2d), consistent with previous reports.[61,95] Excess OM from the growth solution appears to adsorb to the substrate, forming standing phases in regions between some bundles. On diyne PE templates, very different AuNW alignment is observed (Figure 2.2e), with μm^2 areas of precisely-aligned individual wires in addition to areas of bundles. Higher-resolution AFM phase images (figure 2.2F) illustrate that wires are well-separated in areas in which the wire long axes are aligned with the stripe direction of the template. Center-to-center distances (d_{cc}) are 14 nm, 21 nm, or larger multiples of the template periodicity (6.8 nm) — substantially larger than reported dcc values for wires bundling in solution due to depletion attraction (d_{cc} = 5.5–9.7 nm).[65,69] Deposition on simple amine templates produces both bundling and d_{cc} values ~7 nm, similar to the template pitch (see Supporting Information).

Probing the early stages of wire adsorption and assembly (Figure 2.3) using diyne PE templates with large ordered domains, and diluted AuNW growth solution (41× dilution in cyclohexane, or ~27 µg Au/mL cyclohexane, for images shown here) reveals that adsorption proceeds rapidly, with 8 ± 1 µm AuNW/μm^2 substrate after 1 min exposure to AuNW solution (Figure 2.3a). Within the first 15 min of exposure, surface density of wires increases to 30 ± 5 µm AuNW/μm^2 substrate (Figure 2.3e), with average center-to-center distances of 27.5 ± 11.2 nm. SEM images (Figure 2.3b) illustrate that such ordering can extend over areas >100 μm^2. See appendix A for additional SEM images at higher magnification.
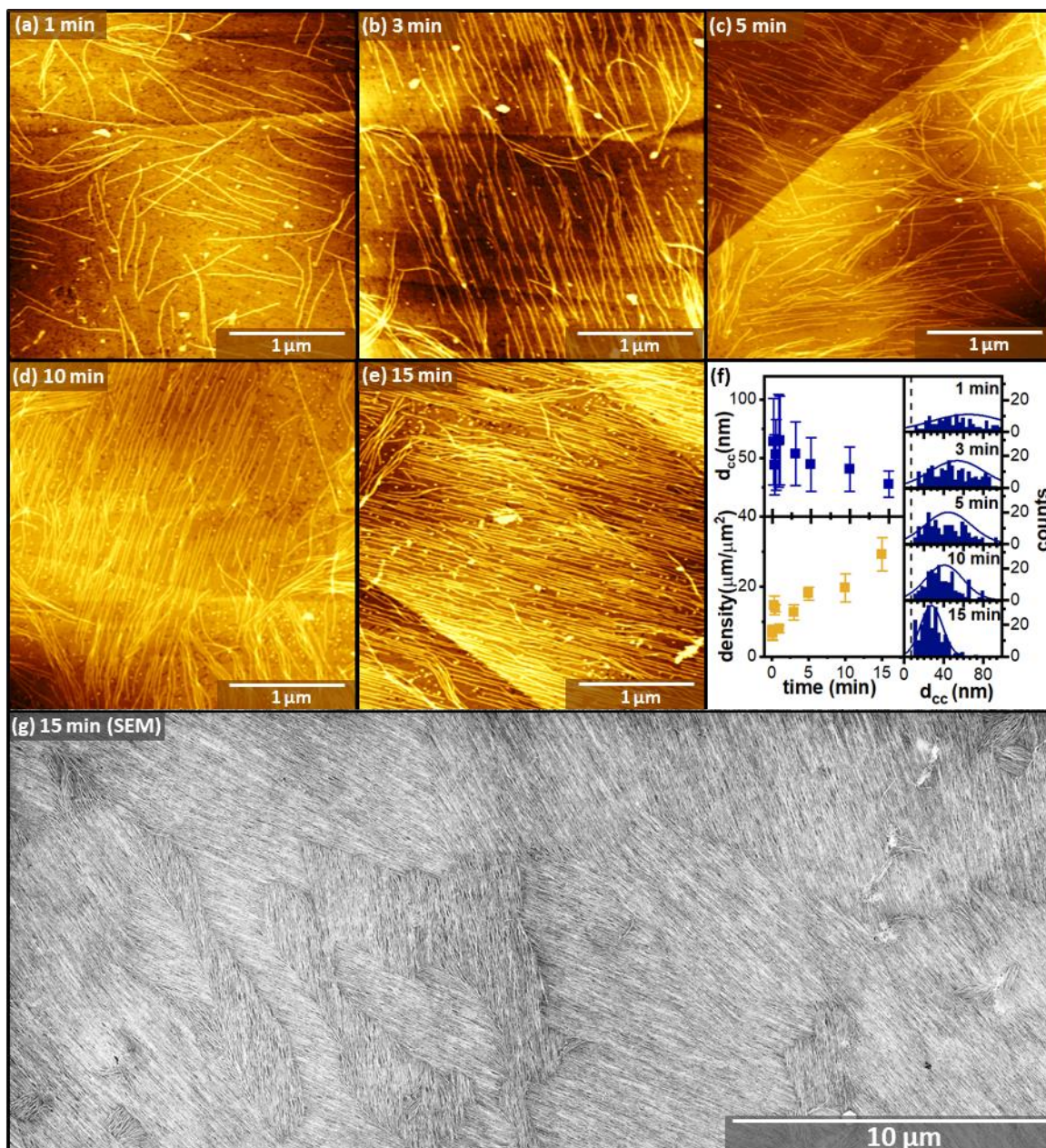
Figure 2.3 Images of AuNW assembly on diyne PE templates at early time points. AFM images of AuNW bundles deposited on diyne PE templates for (a) 1 min, (b) 3 min, (c) 5 min, (d) 10 min, and (e) 15 min. (f) Time distributions of center-to-center distances and AuNW surface densities. (g) Large-area SEM image illustrating AuNW alignment

2.2.2   Dependence of ordering on template hydration

We observed systematic variations in AuNW assembly with environmental humidity (vide infra). To understand likely geometries of water hydrating PE headgroups in the lab environment (before insertion into the AuNW/cyclohexane solution), we performed molecular dynamics

simulations. Hydration limits for PE from natural sources range from ~20-40 wt %,[96,97] or ~8–16 water molecules per headgroup. Minimized molecular models (Figure 2.4a–e) illustrate side and top views of diyne PE on HOPG with 1 to 16 water molecules per diyne PE headgroup. At H2O:diyne PE ratios <4:1, water forms small clusters along the headgroups after minimization, while at ratios ≥4, the water forms a contiguous channel connecting the headgroups.

2.2.2.1   Formation of OM inverse micelles around hydrated headgroups

The presence of hydration shells around diyne PE headgroups in the laboratory environment would not guarantee continued hydration once the template was brought into contact with the AuNW/cyclohexane growth solution However, the AuNW growth solution also contains 32 mM OM; inverse hemicylindrical micelles of OM around the headgroups would represent a reasonable mechanism for maintaining headgroup hydration in the growth solution.

AFM images acquired in a liquid cell illustrate differences in topography for striped PE templates with varying degrees of hydration, placed in either pure cyclohexane (Figure 2.4f–h and dashed bars in histograms in figure 2.4l–n) or 32 mM OM in cyclohexane (Figure 2.4i–k, and solid bars in histograms). At all three humidity levels, exposure to pure cyclohexane results in faint striped topographic features of ~0.2 ± 0.05 nm. Exposure to cyclohexane containing 32 mM OM produces well-resolved, taller topographic features at all humidity levels, with heights that increase with humidity: $\Delta h_{0\%} = 0.34 \pm 0.16$ nm, $\Delta h_{15\%} = 0.51 \pm 0.16$ nm, and $\Delta h_{50\%} = 1.28 \pm 0.55$ nm. At 50% r.h., surface topography in the presence of OM ligands also becomes less regular, with hemispherical structures visible in addition to hemicylindrical micelles, presumably larger clusters of water passivated by OM.
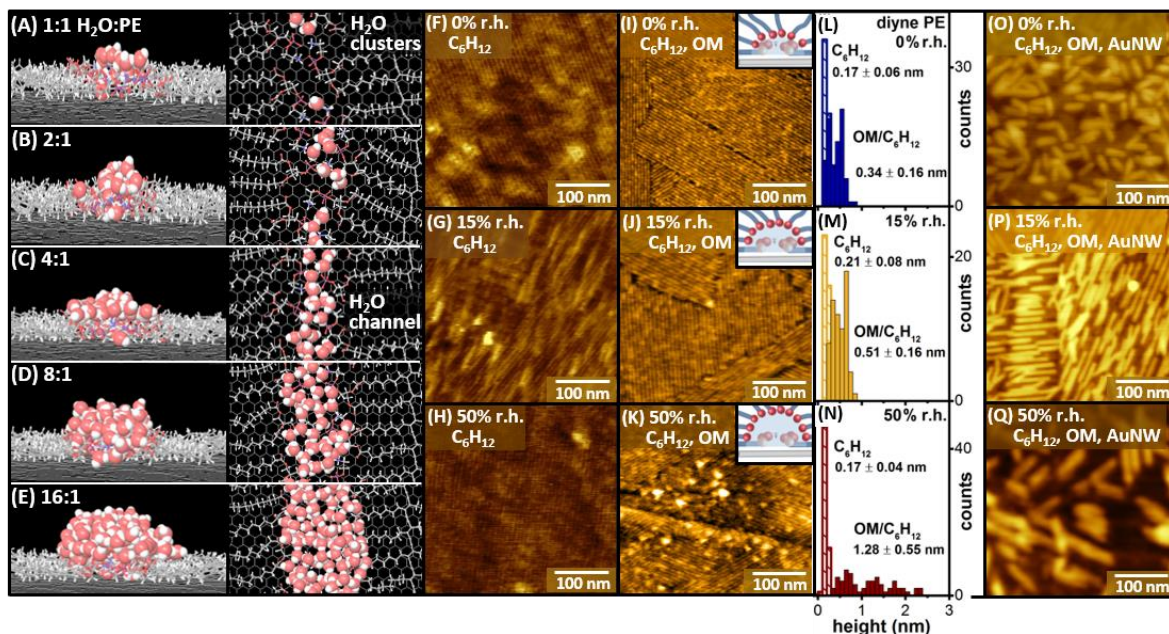
Figure 2.4 AuNW assembly on diyne PE with varying environmental humidity. (a-e) Minimized molecular models of hydrated diyne PE on HOPG with H2O:diyne PE ratios of 1:1 to 16:1, shown as side views (left) and top views (right). (f-k) Liquid cell AFM images of templates held at (f,i) 0%, (g,j) 15%, or (h,k) 50% r.h. prior to immersion in (f-h) pure cyclohexane or (i-k) 32 mM OM in cyclohexane. (l-n) Lamellar height distributions for templates immersed in pure C_6H_{12} (dashed bars) and OM/C_6H_{12} (solid bars). (o-q) Ambient AFM images of AuNW assembly on diyne PE templates maintained at (o) 0% r.h., (p) 15% r.h., or (q) 50% r.h. prior to exposure to AuNW solution.

2.2.2.2 Impact of hydration on AuNW ordering

We examined the impact of template hydration on AuNW ordering, using relatively short wires (average lengths 50–100 nm) with typical lengths substantially shorter than the template domain size, maximizing the extent to which local interactions with the template determine alignment. If diyne PE templates are equilibrated under vacuum (~0% r.h.) prior to being placed in contact with the AuNW solution, randomized wire orientations are observed (Figure 2.4o), consistent with a process in which AuNW adsorb to the template and cannot reorient. Equilibration at 10-20% r.h. produces dense, highly oriented AuNW coverage (Figure 2.4p). Equilibration at high humidity (~50% r.h.) reduces wire adsorption (Figure 2.4q).

Overall, this suggests that water molecules around the headgroups contribute to AuNW ordering, either by modulating the strength of the phospholipid headgroup dipoles or facilitating reorientation of the dipoles to interact with AuNWs during adsorption. Conversely, excess water appears to limit AuNW–template interactions.

2.2.3 Dependence of orientation on headgroup dipoles

Next, we tested whether other molecules with zwitterionic headgroups induced strong AuNW orientational ordering and center-to-center distances > 7 nm. From the standpoint of headgroup dipoles, PE (Figure 2.5a) represents an exceptional case: in standing phases (e.g. the cell membrane), the small size of the terminal primary amine enables formation of H-bonding networks between PE headgroups, increasing their lateral interaction strength (by ~7.2 kcal/mol·H-bond, based on $CH_3NH_2 \cdots HPO_4(CH_3)_2$) in comparison with PC.[74–76]   In aligning polarizable AuNWs, strong interactions with headgroup dipoles should be correlated with stronger nanowire ordering; ordering should also occur independent of whether the positive or negative end of the dipole was positioned further from the substrate. In these experiments, we again used shorter nanowires to maximize the extent to which the template controlled wire alignment.
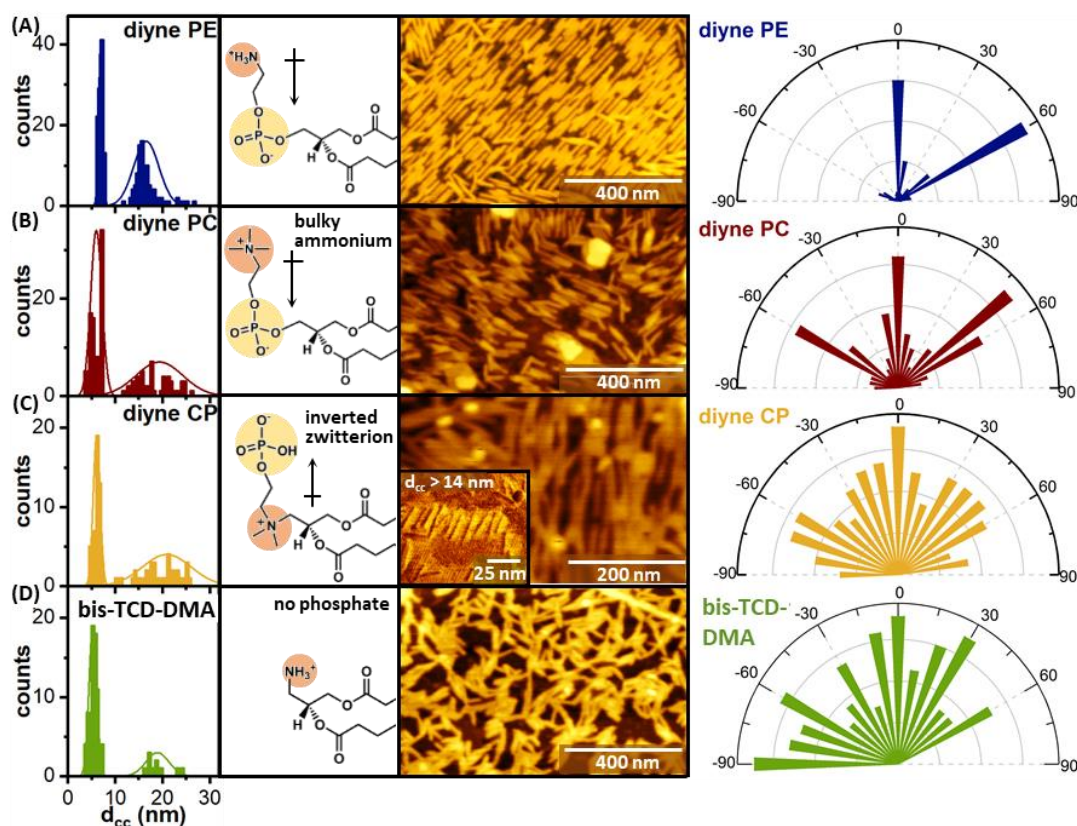
Figure 2.5 AuNW assembly on other striped amphiphilic templates. Histograms of dcc values (left), molecular structures (center left), AFM images (center right), and windrose plots of wire alignment (right) for the following molecules (a) diyne PE, (b) diyne PC, (c) diyne CP, and (d) bis-TCD-DMA.

Diyne phosphocholine (diyne PC) terminates in a bulky quaternary ammonium group, which decreases dipole interaction strength relative to PE. Striped phases of diyne PC produce a large fraction of arrays with d_{cc} = 14 nm (Figure 2.5b); AuNW orientation (quantified in windrose plots) and ordering is weaker than that achieved on diyne PE templates (Figure 2.5a), consistent with somewhat decreased dipole interaction strength.

Next, we examined whether AuNW adsorption required a positive charge to protrude from the interface, by synthesizing a diyne choline phosphate (diyne CP) lipid, with the quaternary ammonium at the base and a terminal phosphate. This molecule also promotes a high degree of AuNW adsorption (Figure 2.5c), meaning that protruding positive charges are not a requirement for AuNW adsorption. Again, wire arrays with large center-to-center distances are evident (figure 2.5c inset).

Additionally, we synthesized an amphiphile including all elements of the PE headgroups above, apart from the phosphate, eliminating the orientable zwitterion. Templates assembled from this molecule, 3-(dimethylamino)propane-1,2-diyl bis(tricosa-10,12-diynoate) (bis-TCD-DMA), produce wire adsorption without the large center-to-center distances characteristic of assembly on templates with headgroup dipoles. Lower degrees of orientational order were also observed (Figure 2.5d), which we rationalize based on the larger relative importance alkyl chain interactions in the adsorption, in the absence of strong dipole interactions.

Thus, strong orientational ordering and large d_{cc} values appear to be primarily associated with molecules containing an orientable zwitterionic headgroup dipole. These effects are stronger for diyne PE, in comparison with other headgroups comprising bulkier substituents.

2.3   Proposed mechanism for separation of AuNWs on diyne PE templates

AuNWs of this type are known to form bundles in organic solvents due to depletion attraction interactions. In our experiments, they also form such bundles both on bare HOPG (Figure 2.2d), and in areas of diyne PE templates in which the AuNW axis does not align with the template axis (Figure 2.2e,f). Thus, the separation of the wires in areas of alignment with the template suggests a repulsive interaction between wires that develops as they adsorb to the template and align with rows of phospholipid headgroups. The interactions of charged particles and dipoles in nonpolar media are not entirely well-understood.[98] However, the Bjerrum length for interactions of elementary charged particles in pure cyclohexane is 25–30 nm,[98] suggesting that

dipole and/or electrostatic interactions over the observed wire–wire separation distances (14–28 nm) are feasible.

To understand likely phospholipid headgroup dipole orientation in the absence of perturbations (e.g. an adsorbing AuNW), we performed molecular dynamics simulations (Figure 2.6a). Rows of diyne PE were simulated in the presence of a layer of explicit water extending 5 Å from the headgroups, with a force field dielectric constant of 2.0 in the surrounding medium, to simulate the cyclohexane solvent environment between the stripes of headgroups. Oleylamine ligands are not treated explicitly in the models, but dielectric constants for long alkyl chains (e.g. ε dodecane = 2.0) are similar to those for cyclohexane.

These simulations suggest that in the absence of perturbation by an external field, headgroup dipoles orient at large azimuthal angles relative to the lamellar median (69° ± 13°; lamellar median direction marked with dashed grey line in windrose plot), and adopt relatively large elevation angles with respect to the substrate (52° ± 23°; substrate plane marked with dashed grey line in windrose plot). Large elevation angles for the array of headgroup dipoles would be expected to contribute to transverse polarization of AuNWs adsorbing to the interface.

Because longitudinal polarization of AuNWs is typically stronger than transverse polarization,[99] we also examined the impact of a dipole in the environment on rows of diyne PE headgroup dipoles (Figure 2.6b). When two point charges positioned outside the edge of the HOPG surface and 1 nm above the HOPG surface are used to simulate a polarized AuNW, PE headgroup dipoles polarize along the lamellar axis (19° ± 8°), and more parallel to the substrate (16° ± 8°). Overall, this points to the capacity for diyne PE headgroups to form aligned dipole arrays coupled with objects (e.g. AuNWs) in the environment.
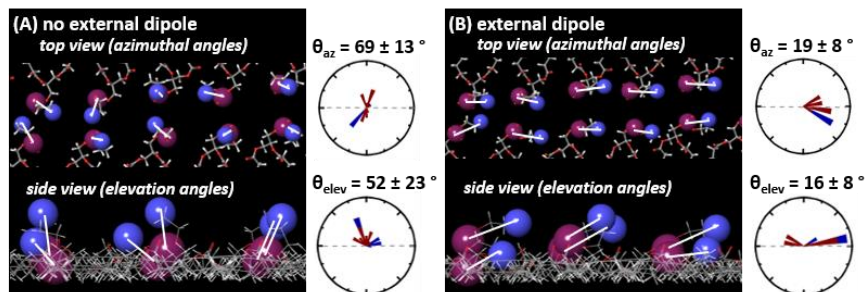
Figure 2.6 Diyne PE headgroup dipole orientation. Molecular dynamics simulations of PE headgroup dipole orientation (a) in absence of external dipole, and (b) in presence of external dipole simulating polarized AuNW.

2.4   Conclusion

Here, we find that striped phases of diyne phosphoethanolamine presenting nm-wide dipole arrays are capable of precisely orienting and straightening flexible, μm-long gold wires with diameters < 2 nm. Creating oriented nanocrystal lattices with spacings dictated by template chemistry rather than ligand shell thickness has potential utility in controlling plasmon coupling and other physical properties.

More broadly, the findings presented here suggest design principles for creating flexible surface templates in which ligands respond collectively to their environment to facilitate oriented binding of an anisotropic object. In biology, phospholipids operate in a relatively polar environment at the membrane periphery. Here, they confer similar utility in nonpolar environments common in inorganic nanocrystal synthesis. The capability of template phospholipids to strongly orient AuNWs depends on the presence of small numbers of water molecules on the surface and the availability of excess simple surfactants in solution. This suggests a minimal environment that may be necessary to recreate collective functions of the polar membrane periphery in a nonpolar environment.

2.5   Experimental Methods

2.5.1   Materials

4-Pentyn-1-amine, silver nitrate, N-bromosuccinimide, copper chloride dihydrate, potassium hydroxide, hydroxylamine hydrochloride, ethylamine, sulfuric acid, sodium thiosulfate, ammonium hydroxide, oleylamine (technical grade, 70%), triisopropylsilane (TIPS, 98%), 3-dimethylamino-1,2-propandiol, N,N'-dicyclohexylcarbodiimide (DCC), 4-(dimethylamino)pyridine (DMAP), sodium iodide, trimethyl phosphite, 2-bromoethanol, trimethylsilyl chloride, anhydrous acetonitrile (MeCN), iodine,   and molecular sieves (4Å) were purchased from Sigma Aldrich (Saint Louis, MO) and used as received. 1-Eicosyne and tricosa-10-12-diynoic acid was purchased from GFS Chemicals (Columbus, OH) and used as received. Methanol, diethyl ether, dichloromethane (DCM), acetone, dimethylformamide (DMF), ethyl acetate, pyridine, ammonium chloride, sodium bicarbonate, sodium sulfate, magnesium sulfate, and sodium chloride were purchased from Fisher Scientific (Fair Lawn, NJ) and used as received. Cyclohexane (HPLC grade), dry cyclohexane (99.5% extra dry, Acroseal), and gold tetrachloroauric acid trihydrate (ACS reagent grade) were purchased from Acros Organics (Fair Lawn, NJ) and used as received. Silica gel was purchased from Machery Nagel (Bethlehem, PA) and used as received. 1,2-bis(10,12-tricosadiynoyl)-sn-glycero-3-phosphoethanolamine (diyne PE, > 99% purity) and 1,2-bis(10,12-tricosadiynoyl)-sn-glycero-3-phosphocholine (diyne PC, >99% purity) was purchased from Avanti Polar Lipids (Alabaster, AL).

2.5.2   Instrumentation

^{1}H NMR spectra were acquired using an INOVA Varian 300 MHz spectrometer with a Varian 5-mm 4-nucleus/BB Z-gradient probe (Scientific Instruments, Palo Alto, CA). All atomic force microscopy images were acquired using a Veeco (Bruker Instruments, Billerica, MA) MultiMode AFM with NanoScope V controller or an Agilent (Agilent, Palo Alto, CA) 5500 AFM.

2.5.3   Synthesis of 1-bromo-1-eicosyne

Synthesis of 1-bromo-1-eicosyne was adapted from a previously published procedure[100] described briefly here. In a typical reaction, 1-eicosyne (3.6 mmol) was added to acetone (18 mL), followed by the addition of silver nitrate (0.36 mmol) and N-bromosuccinimide (3.96 mmol). The reaction mixture was stirred for 3 h under ambient conditions, then diluted with 100 mL of hexanes

and filtered. The filtrate was reduced in volume and passed through a small silica plug with hexanes. The product was reduced in volume to afford the final product as a colorless oil (typical yield 75%).

2.5.4   Synthesis of 4,6-pentacosadiynamine

4-pentyn-1-amine (1.92 mmol) was dissolved in a 1 M KOH (aqueous, 1.8 mL) in a round-bottom flask. In a separate vial, methanol (10 mL) was added to hydroxylamine hydrochloride (0.18 mmol). In a second vial, copper chloride dihydrate (0.46 mmol) was dissolved in ethylamine (3 mL). The mixtures in the first and second vials were sequentially added to the round-bottom flask, and the reaction mixture was then cooled to -78 ˚C. Subsequently, a solution of 1-bromo-eicosyne (1.82 mmol) dissolved in THF (3 mL) was added dropwise. The reaction mixture was allowed to warm to room temperature and the reaction continued at that temperature for 24 h. If the solution turned blue, additional aliquots of hydroxylamine hydrochloride were added. The reaction was then quenched by addition of a 10% aqueous solution of sulfuric acid. Crude product was extracted with diethyl ether (3×50 mL) and then washed with water (3×50 mL) and sodium thiosulfate brine (3×50 mL). The organic layer was subsequently dried over anhydrous Na_2SO_4, filtered, and the ether removed by rotary evaporator. The product was purified on a silica column with a mobile phase of 9:1 $CHCl_3$:MeOH followed by 2% ammonium hydroxide in 9:1 $CHCl_3$:MeOH.

2.5.5   Synthesis of 3-(dimethylamino)propane-1,2-diyl bis(tricosa-10,12-diynoate)

Synthesis of bis-TCD-amine was adapted from previous literature.[101] Filtered 10,12-TCDA (3.54 mmol) was dissolved in 20 ml of DCM. 3-dimethylamino-1,2-propandiol (1.68 mmol), DMAP (0.79 mmol), and DCC (0.73 mmol) where added to the solution while stirring. The reaction was stirred at room temperature for 3 h without exposure to light. The reaction was filtered to removed precipitated dicyclohexylurea, followed by washing twice with 1 M HCl to remove excess DMAP. The organic layer was then collected; water was removed with sodium sulfate, and the remaining liquid was concentrated using rotary evaporation. No further purification was required.

2.5.6   Synthesis of 1,2-bis(10,12-tricosadiynoyl)-sn-glycero-3-choline phosphate

Synthesis of diyne CP was adapted from literature protocol.[101] Bis-TCD-amine (2.28 mmol) from the previous synthetic step above was dissolved in 2:1 DCM:MeOH (6 mL) solution. 2-bromoethanol (11.4 mmol) was added followed by diisopropylethylamine (4.33 mmol). The reaction mixture was stirred at 40 ˚C for 18 h. The reaction mixture was further diluted with DCM and washed with 1 M HCl twice. The organic layer was dried with sodium sulfate and concentrated. The product was purified via silica column with a mobile phase of 10% MeOH in DCM. The product isolated from the reaction described above (0.34 mmol) was dissolved in 3.4 mL of 5:1 DCM:pyridine solution and stirred over an acetone/dry ice bath. In a second round-bottom flask, I_2 (1.36 mmol) was dissolved in 1.4 mL of DCM, after which the solution was placed in an acetone/dry ice bath. Trimethyl phosphite (1.36 mmol) was added slowly to the I_2 solution; the solution was stirred until it became colorless. The I_2 solution was then added slowly to the first round-bottom flask. The reaction mixture was stirred for 30 min and was subsequently allowed to warm to room temperature. The reaction mixture was then diluted with 50 mL of DCM and washed with 1 M HCl twice. The organic layer was dried over sodium sulfate and concentrated. This material (0.30 mmol) was dissolved in anhydrous MeCN. Catalytic amounts (5%) of NaI were added to the mixture. Trimethylsilyl chloride (1.8 mmol) was slowly added to the mixture at room temperature. The reaction was stirred for an addition 30 min under reflux and then cooled to room temperature. The reaction mixture was concentrated, and methanol was added to the reaction and stirred for 30 min at room temperature. The reaction mixture was concentrated and purified using a silica column with a mobile phase of 35% MeOH: ammonium hydroxide (5:1) in DCM.

2.5.7   Procedure for Langmuir-Schaefer (LS) transfer of amphiphile monolayers

LS deposition was performed using a Kibron (Helsinki, Finland) MicroTrough XL. For transfer of single chain amphiphiles, 12 µL of a 0.75 mg/mL solution of the amphiphile in chloroform was deposited onto a subphase of deionized water at 30 °C. The trough was equilibrated for 15 min, to allow the solvent from the spreading solution to evaporate; the trough barriers were then slowly swept inwards at a rate of 6 mm/min. A freshly cleaved HOPG substrate was heated to 45 °C using a custom-built thermally controlled dipping attachment reported previously.[44] When the desired packing density condition for transfer was achieved based on motion of the barriers (75 Å^2/chain for the 4,6-PCD-NH$_2$), the HOPG substrate was lowered

horizontally into contact with the subphase at a speed of 2 mm/min. Substrates utilized for direct imaging of lamellae were prepared at 3 mN/m (4,6-PCD-NH$_2$) to maximize visibility of lamellar boundaries. After 4 min in contact with the liquid interface, the HOPG was slowly lifted out of contact with the subphase at 2 mm/min.

For phospholipid monolayers, deposition was performed by spreading 40 µL of 0.50 mg/mL solution of phospholipid of choice in chloroform on a subphase of 5 mM MnCl$_2$ at 30 °C. After deposition, the trough was allowed to equilibrate for 30 min, in order to allow the solvent from the spreading solution to evaporate. Transfer was carried out at a surface pressure of 30 mN/m (diyne PE and diyne PC), 16.5 mN/m (diyne CP), or 8 mN/m (Bis-TCD-NH$_2$). Freshly cleaved HOPG was heated to 50 °C using the thermally controlled dipping attachment, then lowered into contact with the subphase at 2 mm/min. The HOPG was left in contact with the interface for 2 min and then withdrawn from the interface using the automated dipper.

All samples were dried with N$_2$ prior to further processing. Diacetylene-functionalized amphiphilic monolayers prepared as described above were then photopolymerized for 1 h via irradiation under a 254-nm 8-W UW lamp with approximately 4 cm between sample and lamp.

2.5.8   AuNW growth

AuNW synthetic procedures were adapted from literature protocols.[57,63,65,69] In a typical reaction for long wires, 2.5 mg of HAuCl$_4$·3H$_2$O was added to 1.8 mL of dry cyclohexane, followed by 84 µL of oleylamine. Molecular sieves were added to the reaction mixture to remove water. The solution was mixed briefly at room temperature using a vortexer. Triisopropylsilane (120 µL) was added and the solution was mixed again. The reaction mixture was immediately sealed and transferred to a humidity-controlled environmental chamber, and maintained at ambient temperature for 12 h, unless otherwise stated. After the desired aging time the growth solution was diluted 41x (75uL in 2.5 mL cyclohexane). For wire assembly, HOPG substrates were lowered into contact with the growth solution. HOPG substrates were lifted out of contact with the solution, washed with 1 mL cyclohexane each, and dried with N$_2$. Similar experimental procedures were followed for the synthesis of shorter wires, with the exception that the amount of cyclohexane in the growth solution was increased to 12 mL; these solutions were not diluted further prior to substrate exposure for AuNW assembly. All substrates were stored at 4 ˚C following wire deposition.

2.5.9 Extraction of nanostructures from AuNW growth solution

Solution-phase reaction products (*i.e.* AuNWs, AuNSs) were harvested by centrifugation at 6000 rpm for 30 min in a 1:1 cyclohexane/ethanol solvent mixture. This procedure was repeated twice in order remove excess oleylamine and silane. After the final wash, the pellet was redispersed in cyclohexane and stored at 4 ˚C prior to TEM imaging.

2.5.10 AFM imaging in ambient conditions.

AFM imaging was performed under ambient conditions using either a Veeco (Bruker Instruments, Billerica, MA) MultiMode AFM or Agilent (Agilent, Palo Alto, CA) 5500 AFM. Imaging was performed in tapping mode with Bruker RFESP-75 tips (nominal force constant 3 N/m and radius of curvature <10 nm). Tip broadening was corrected using the equation

$$w_0 = w_{exp} - 2(h * [2r_0 - h])^{1/2}$$

where w_0 is the corrected width, w_{exp} is the experimentally measured width, and r_o is the AFM tip radius of curvature.

2.5.11 AFM imaging in liquid

Liquid cell imaging was performed using an Asylum Cypher ES. Imaging was performed in tapping mode with Mikromasch (Sofia, Bulgaria) XCN12/Cr-Au tips (nominal resonant frequency 67 kHz). All samples were exposed to an environment with the relative humidity conditions stated in the manuscript for 8 h prior to imaging. The sample was immediately placed in the AFM and covered with a 100 µL droplet of cyclohexane (dry) or oleylamine (32 mM) in dry cyclohexane. Samples were imaged in attractive mode to prevent damage to lamellar domain structure.

2.5.12 Characterizing wire properties via image processing

AuNW average lengths, surface coverage, relative orientation, and curvature from AFM images were determined utilizing a Ridge Detection algorithm[102] implemented previously in an Image J plugin, with outputs of the algorithm further modified using custom scripts. AuNW curvature was determined by taking the ratio of wire length to the distance between the wire's two furthest points, which was then mapped onto a range of 0-1, with values close to 0 indicating low degrees of curvature. After the curvature was established, the wires with values greater than 0.05 were eliminated, and the relative angles between wires was calculated through the use of the

representative vector. Surface densities of AuNW (μm of AuNW contour length per $μm^2$ of substrate area) were determined by using the ridge detection algorithm to identify the contour length of each wire visible within an image. Inter-wire spacings were measured from Gwyddion line scans and compiled into histograms. At least 3 images (typically 3 μm x 3 μm) were analyzed for each data point graphed; at least 175 center-to-center distances were measured for each histogram.

2.5.13 TEM Imaging

All TEM imaging was performed on a Tecnai G2 20 (Thermo Fisher Scientific, Hillsboro, OR) with an accelerating voltage of 200 kV and a lanthanum hexaboride (LaB6) filament. TEM samples were prepared by depositing 6 µL of re-dispersed gold nanowire solution on a 200 mesh C/Cu grid (Ted Pella, Redding, CA). The solution was wicked from the grid after 10 s.

2.5.14 SEM Imaging

High resolution imaging of surface-templated AuNW arrays under high magnification was performed using a Teneo VS SEM (FEI Company, Hillsboro, OR) at a working distance of ~5.0 mm using the in-column Trinity detector T3. Beam currents in the range of 0.20-0.80 nA were selected for best resolution image acquisition through a 32 µm diameter aperture with an accelerating voltage of 5.00 kV. All substrates were affixed to standard SEM pin stub specimen mounts with conductive carbon tape. To further enhance substrate–mount conductivity, a small amount of colloidal silver paint (PELCO®, Ted Pella, Inc.) was applied along the perimeter of the HOPG from the face down to the pin stub.

2.5.15 Energy minimization

Software packages Maestro and Macromodel (Schrödinger, Cambridge MA) were used, respectively, to visualize molecular structures and to perform force field minimizations. Models of lamellar structures were minimized using the OPLS_2005 force field, with normal cutoffs for van der Waals, electrostatic and hydrogen bonding interactions. Minimizations were performed using the Polak-Ribiere conjugate gradient (PRCG) algorithm and gradient method with 50000 runs and a convergence threshold of 0.05.

CHAPTER 3.   TEMPLATING OF AUNW RIBBON PHASES ON 1-NM WIDE DIPOLE ARRAYS ON HOPG AND MOS₂

3.1   Introduction

Controlling the patterning of materials at the interface of layered materials like graphene and other layered inorganic materials such as dichalcogenides of molybdenum is critical in the development of next generation nanoelectronics. Unlike graphene which is a semimetal, transition metal dichalcogenides (TMDs) possess a tunable bandgap that is advantageous for several applications such as flexible, wearable transparent electronics,[103–106] optoelectronic devices,[107,108] and digital electronic switches due the material's superior electronic[109,110] and optical properties.[111–113] TMD-based electronic devices are immune to short-channel effects due to their van der Waals epitaxial structure and lack of dangling bonds.[114] Noncovalent functionalization of MoS_2 is less widely studied in part due to the low enthalpy adsorption of alkyl chains on the substrate and the weak epitaxial matching between the substrate lattice and C-C bond distance.[13,72] However, some of the noteworthy reports have shown oriented growth of gold nanowires on MoS_2[115] as well as the self-assemble networks of oleylamine which result in doping of the MoS_2 thin-film.[71] Therefore, mastering molecular assembly and adsorption of specific materials (i.e. dopants) with specific patterns can allow for controlled interactions between the dopant and the substrate.

Recently, we found that diyne phosphoethanolamine (diyne PE) form striped lamellar phases on layered materials such as HOPG and MoS_2.[13,45] Monolayers of diyne PE on HOPG typically adsorb with both chains in contact with the substrate increasing the overall van der Waals interactions. Moreover, diyne PE monolayers on MoS_2 adsorb with an edge-on orientation where only one chain is in contact with the substrate enabling chain-chain interactions between the two layers of tails. This edge-on adsorption could result in differences the adsorption of AuNWs.

Here, we illustrate the importance of functionalization of MoS_2 for the adsorption of AuNWs at the interface. Functionalization of both MoS_2 and HOPG with diyne PE results in long range ordering of AuNW over areas >100 μm^2. As the AuNW wire length is shorten below 600 nm packing on diyne PE/MoS_2 becomes tighter resulting in ribbon phases with wire-wire distances of 7 nm. Ribbon phases start to appear on diyne PE/HOPG substrates when the wire length is around 50 nm, however ribbon phases are more predominate on diyne PE/MoS_2. These results

suggest that the difference in monolayer conformation and possibly the substrate polarizability differences may be the cause for the differences in the templated assembly of AuNW.

3.2   Results and Discussion

3.2.1   Adsorption of AuNWs on functionalized and unfunctionalized HOPG and MoS$_2$

AuNWs were grown from previously reported procedures.[57,63,64] Typically, AuNW growth solutions were aged for 12 h followed by dilution (34x dilution in cyclohexane) and exposure to both functionalized MoS$_2$ and HOPG with diyne PE monolayers and unfunctionalized HOPG and MoS$_2$ substrates for 15 minutes to compare templating properties (Figure 3.1). AuNW adsorption on bare MoS$_2$ (Figure 1a) is limited which may be due to the low alkyl chain adsorption enthalpy on MoS$_2$. SEM image (see appendix B, Figure B.1a, b) illustrate that AuNW tend to adsorb to the step edges of the substrate which is consistent with other previous reports. AuNW adsorb to a much greater extent and in bundles on bare HOPG (Figure 3.1b) which has been previously reported by our group. AFM height images show that excess oleylamine adsorbs to both exposed substrates (figure 3.1a ,b) (*i.e.* MoS$_2$ and HOPG).

Figure 3.1c illustrates that wires adsorb to a greater extent on functionalized MoS$_2$ compared to unfunctionalized MoS$_2$ suggesting that functionalization of MoS$_2$ is important to the adsorption of AuNWs because it facilitates interactions between the surface and the AuNW. Upon functionalization of HOPG and MoS$_2$ with diyne PE (Figure 3.1c, d) bundled wires from solution appear to unpack when the long axis of the wire is in alignment with the lamellar axis on both substrates. AuNW also appear to straighten with an overall increase in ordering compared to that of unfunctionalized substrates. The diyne PE template possibly acts as a ligand allowing for wires to adsorb to the surface in a more controlled fashion contributing to the straightening and ordering of the wire. We have previously reported that the strong headgroup dipole of diyne PE on HOPG can reorient collectively in response to an external stimulus (i.e. AuNW) and the nanochannel of water surrounding the headgroup helps in modulating the strength possibly. Upon polarization wires may experience a repulsive interaction resulting in wires templating with wire-wire distances greater than the template pitch (7 nm). Diyne PE dipole arrays on MoS$_2$ substrates when in contact with AuNW experience a similar effect resulting in wire-wire distances (d_{cc}) greater than the template pitch which is similar to d_{cc} values for wires on diyne PE/HOPG (Figure 3.1e). Early time

points (appendix B, Figure B.2) suggests that wires template faster to diyne PE/MoS$_2$ within the first five minutes however at 10 minutes the surface coverage of wires on diyne PE/MoS$_2$ and diyne PE/HOPG are very similar. Suggesting that wire adsorption is rapid on both substrates.
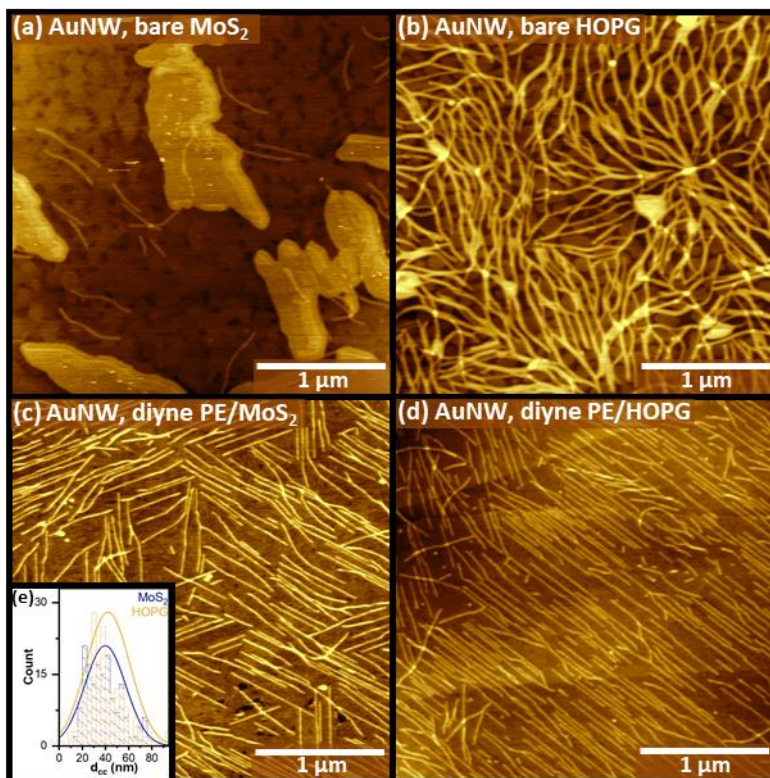
Figure 3.1 AFM height images showing AuNW adsorption after 15 minute exposure on (a) bare MoS$_2$ (b) diyne PE on HOPG (c) diyne PE/MoS$_2$ and (d) diyne PE/HOPG.

3.2.2   Long range AuNW ordering is achieve on both substrates

Striped templates of diyne PE were prepared via Langmuir-Schaefer (LS) conversion using thermal anneal processing during transfer we can achieve domains with edge lengths >1 µm on both HOPG and MoS$_2$ substrates (Figures 3.2a, d). SEM images of samples with long range ordering and exposure time of 15 minutes illustrate that AuNW assemble on diyne PE templates similarly on the macroscopic level for both substrates. Large area SEM images illustrate that templated surfaces can order AuNW over >100 µm^2 for both substrates (Figure 3.2b, e), corresponding to many millions of molecules. AuNW assembly on diyne PE/HOPG samples (Figure 3.2f, e) do have more ordering however that could be due to slightly larger domain sizes

and higher degree of ordering on HOPG compared to MoS_2 (Figure 3.2b, c). Nevertheless, both substrates template AuNWs over macroscopic areas all while having molecular-scale control.
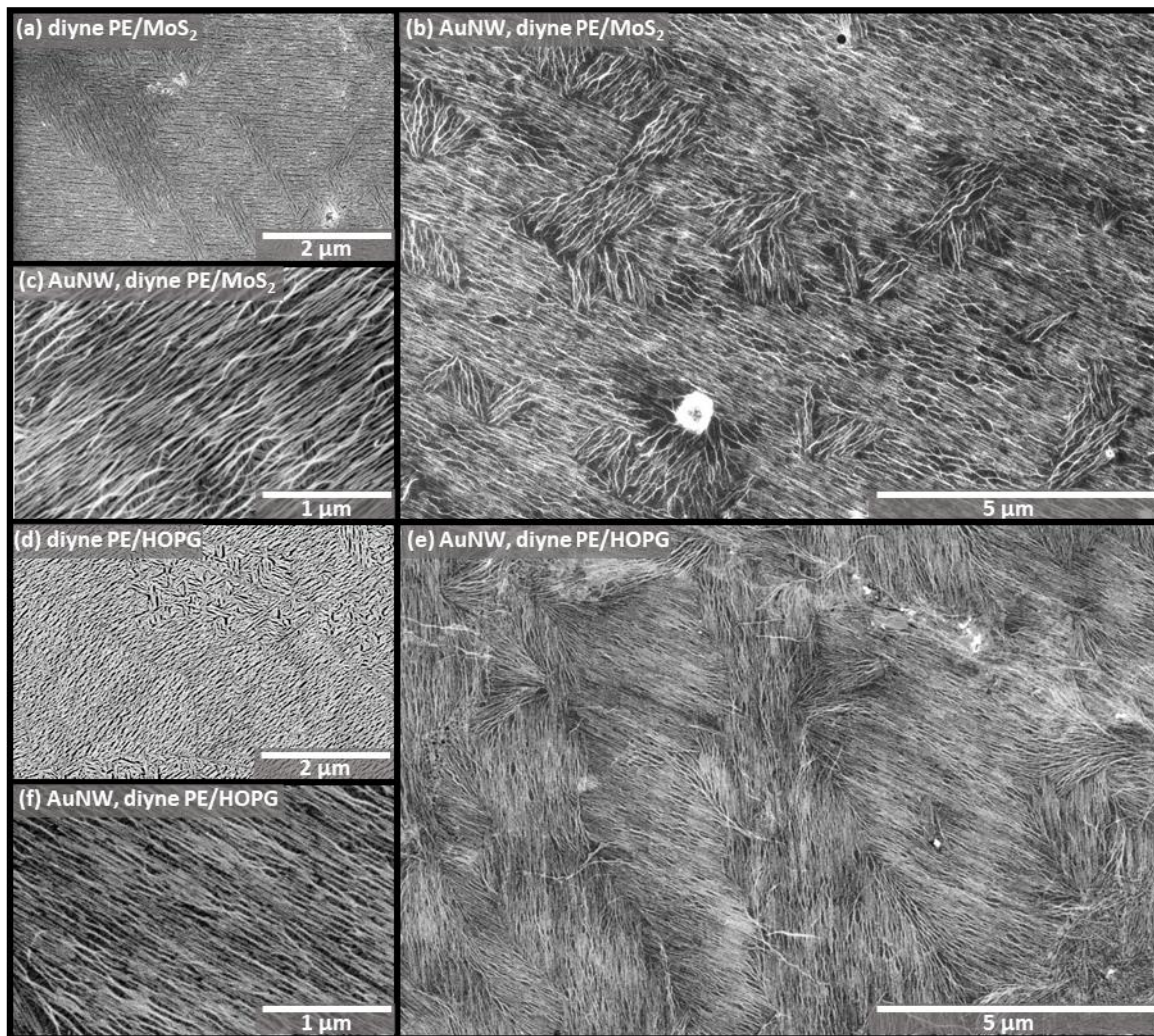
Figure 3.2 SEM images of AuNW assembly on diyne PE templates. (a) SEM of diyne PE/MoS_2 (b) high resolution SEM of AuNW on diyne PE/MoS_2 (c) large-area SEM image of AuNW on diyne PE/MoS_2 (d) SEM of diyne PE/HOPG (e) Large area SEM of AuNW on diyne PE/HOPG (f) high resolution SEM of AuNW on diyne PE/HOPG.

3.2.3   AuNW ribbon phase assemble on diyne PE/MoS_2 substrates

Upon further dilution (200x) of the growth solution prior to substrate (diyne PE/MoS_2) exposure at varying early time points, SEM images (figure 3.3) reveal that AuNW initially adsorb to the surface with large d_{cc} spacings however, over time AuNW form ribbon phases on the surface. Diyne PE/MoS_2 substrates exposed to growth solutions for 1 minute (figure 3.3a) reveal individual

wires with relatively high surface (see appendix Figure B.3 for large area SEM). After a 5 minute exposure ribbon phases are present on the surface (Figure 3.3b), high resolution SEM images (Figure 3.3c) shows that the wires are tightly packed within each ribbon phase and that wire arrays are following the underlaying lamellar axis. AuNW with an average wire length of 804 ± 259 nm produce ribbon phases under dilute conditions (200x) however, ribbon phases are not present at higher concentrations. Ribbon phases were not present at 1 minute exposure times even through surface coverage of wires is relatively high, suggesting that wires do not template to the surface in ribbon phases but rather form after initial adsorption. AuNW on diyne PE/HOPG (appendix Figure B.4) do not adsorb in ribbon phases at any time point tested, rather individual wires adsorb to the surface. Results suggests a possible link between the difference in the polarizability of substrate (i.e. MoS_2/HOPG) and the assembly of AuNW ribbon phases.
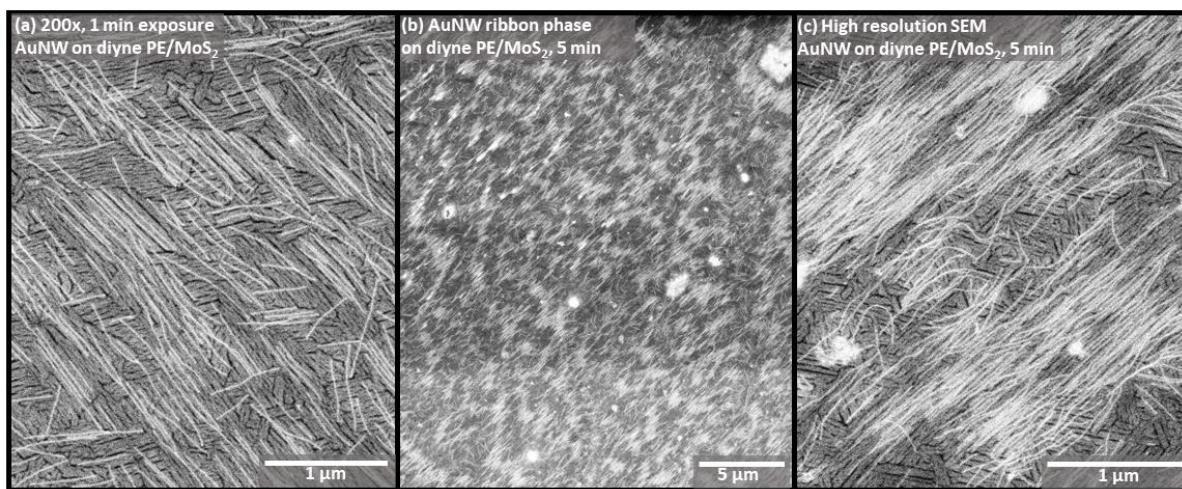
Figure 3.3 SEM image of AuNW assembly on diyne PE/MoS_2 at low concentrations (200x) after (a) 1 or (b) 5 minute exposure. (c) High resolution SEM of AuNW on diyne PE/MoS_2.

3.2.4   AuNW Ribbon Phases are dependent on wire length

To determine whether the polarizability of the wire influences the assembly ribbon phases on diyne PE/MoS_2/HOPG substrates, AuNW of various lengths (ranging from ~800 to 50 nm) were synthesized (Figure 3.4a inset has average wire lengths). Growth solution (1.44-5x) were diluted to a total 34x dilution factor and substrates were exposed to the growth solution for 10 minutes, washed and imaged via AFM and SEM. AuNW with an average wire length of 860 ± 295

nm results in long range ordering (Figure 3.4a, c) with d_{cc} distances greater than 7 nm for both substrates (Figure 3.4 c). Reactions run at a 2x dilution produce wires with an average length of 601 ± 234 nm assemble on the surface with d_{cc} spacing greater than that of the template pitch however the average wire-wire distance is smaller compared to 800 nm length wires (Figure 3.4f-j). Overall wires with length above 600 nm appear to adsorb individually with long range ordering on both diyne PE/MoS$_2$/HOPG substrates. Moreover, wires (<600 nm) appear to polarize upon contact with surface and experience repulsive interactions on both substrates resulting in d_{cc} spacing greater than 7 nm.

Templated wires with an average wire length of 287 ± 87 nm (3x dilution) start to form of ribbon phases on diyne PE/MoS$_2$ surfaces (Figure 3.4k). Ribbon phases are not present on diyne PE/HOPG substrates (Figure 3.4n, o) and wires exhibit larger d_{cc} distances compared to AuNW d_{cc} distances on diyne PE/MoS$_2$ (Figure 3.4h). Substrates exposed to growth solutions with an average wire length of 133 ± 32 nm, experience majority of wires in ribbon phases on diyne PE/MoS$_2$ surfaces (Figure 3.4p, q). Whereas wires once again adsorb individually on diyne PE/HOPG substrates (Figure 3.4s, t). Furthermore, when the wire length is shortened even more (58 ± 16 nm) ribbon phases are present (Figure 3.4u-y) on both substrates (diyne PE/MoS$_2$ and diyne PE/HOPG). The low density of ribbon phases is due to an overall lower density of wires on the surface. However, if the growth solution is not further diluted (34x) prior to substrate exposure the overall ribbon phase density will increase on both substrates.

The overall d_{cc} values decrease as the wire length decreases on both substrates however to a greater extent on diyne PE/MoS$_2$. This decrease in d_{cc} values suggests a decrease in the repulsive interactions between wires upon contact with the diyne PE template. As the wires shorten there could possibly be a decrease in the polarization resulting in differences in templating of wires on the surface. The differences in the monolayer structure on HOPG and MoS$_2$ as well as the polarizability of the substrate could possibly influence the formation of ribbon phases. Diyne PE headgroup dipoles on MoS$_2$ could possibly reorient to a lesser extent compared to HOPG resulting in AuNW ribbon phases. This change may be due to differences in the hydration of the headgroup or due to decreases in the ordering of the headgroup. Both freshly cleaved HOPG and MoS$_2$ have similar contact angles of ~64° and ~69° respectively.[116,117] However the difference in the monolayer structure could possibly result in differences in the wettability of the surface.
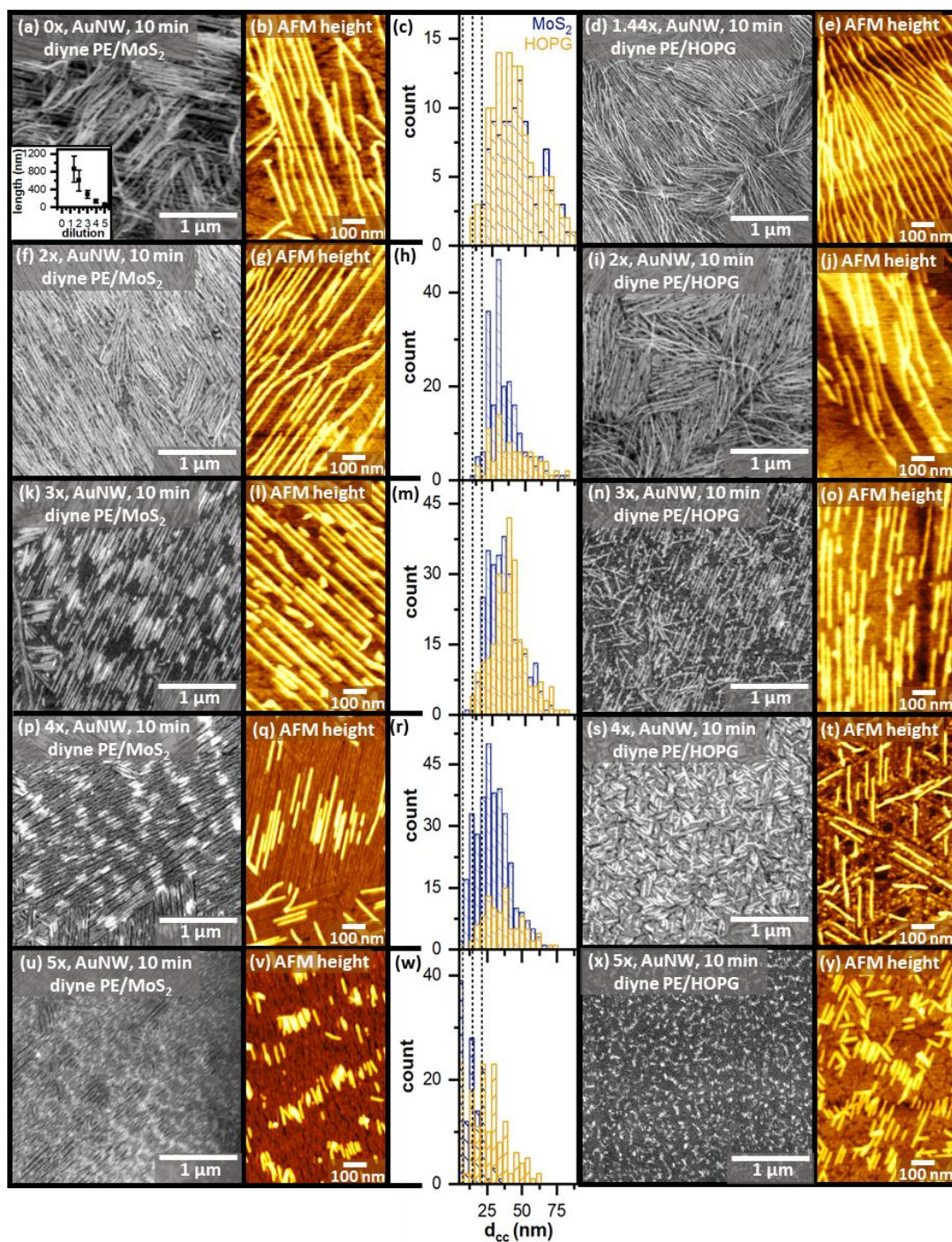
Figure 3.4 SEM images of AuNW assembly on diyne PE/MoS$_2$ with varying wire lengths post 10 minute exposure (a, f, k, p, u). SEM of AuNW assembly on diyne PE/HOPG (d, i, n, s, x). Histograms of d$_{cc}$ values on MoS$_2$ (blue) and HOPG (yellow) for the following wire length (c) 860 ± 295 nm, (h) 601 ± 234 nm, (m) 287 ± 87 nm, (r) 133 ± 32 nm, and (w) 58 ± 16 nm.

AuNW ribbon phases occur on diyne PE/MoS_2 when the wire length is below 300 nm. SEM images (Figure 3.5a, e) illustrate that ribbon phases are present over large areas of the diyne PE/MoS_2 template within 10 minutes of exposure for both 280 nm and 130 nm wires. See appendix B Figure B.5 for large area SEM images. Shorter wires (~130 nm) appear to produce ribbon phases to greater extent compared to wires with an average wire length of 280 nm, which may be due to longer wires experiencing stronger repulsive interactions. High resolution images (Figure 5b, f) show that in both cases the wires within ribbons have aligned ends and have similar lengths. The average ribbon length of 3x dilution is 268 ± 44 nm (Figure 3.5d) which is consistent with the average wire length (287 ± 87 nm) at this concentration. Similarly, shorter ribbon phases (4x dilution) have an average length of 207 ± 36 nm which is slightly longer than the average wire length of 133 ± 32 nm. The ribbon length is indicating that each ribbon is made up of a side by side assembly of wires with none (in the case 3x) to very little (in case of 4x) end to end assembly of wires. In both cases there is more variability in the ribbon-ribbon distances (Figure 3.5c, g) with an average distance of 299 ± 112 nm and 360 ± 132 nm for 3x and 4x respectively. In both cases ribbon-ribbon distances are greater than the average ribbon distance (double the wire ribbon length in the case of 4x) suggesting that dipoles may be the cause of this spacing not just a lack of available surface for the wires to bind between two arrays of wires.
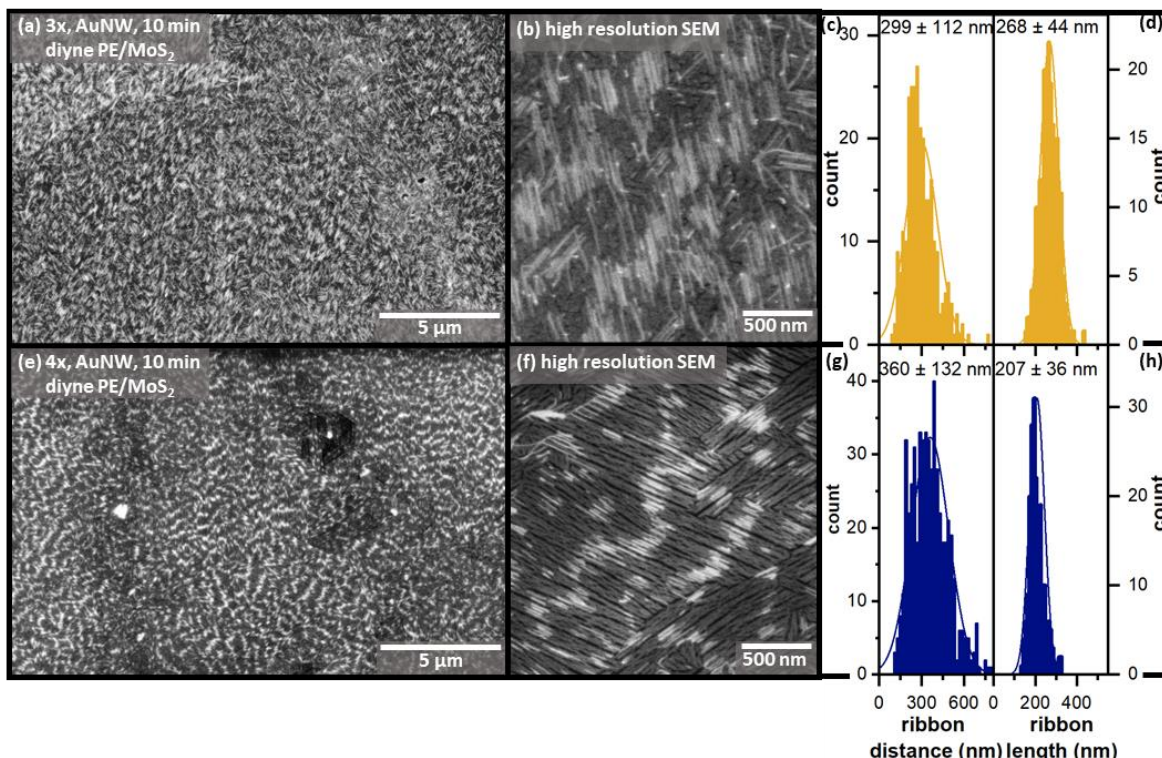
Figure 3.5 AuNW ribbon phase on diyne PE/MoS$_2$ with varying concentrations (3x and 4x) after 10 min exposure to the growth solution. Large area SEM of (a) 3x and (e) 4x, high resolution SEM (b) 3x and (f) 4x, histogram of ribbon distances (c,g), histogram of ribbon length (d,h).

3.2.5 AuNW ribbon phase after long exposure times

Samples that are exposed to growth solutions with wire lengths ranging from 600 to 900 nm (1.44 and 2x) for 60 minutes experience similar d$_{cc}$ distances and slightly higher coverage compared to samples exposed to growth solutions for 10 minutes (see appendix B figure B.6) on both diyne PE/MoS$_2$ and diyne PE/HOPG. However, at 3x dilution the ribbon phases which are present at 10-minutes decrease in quantity which could be due to an increase in surface coverage (appendix B figure B). However, in the case of 4x dilution the ribbon phases appear to be more pronounced after 1 hour (Figure 3.5d). AFM height images of both 10 min and 60 min samples show an overall increase in the density of tight packed arrays on the surface and a decrease in d$_{cc}$ distances with an increased exposure time (Figure 3.5b, c, e). AFM phase image (Figure 3.6f) illustrate that wires within the ribbon phase have d$_{cc}$ values matching that of the template after longer exposure times. Diyne PE/HOPG samples exposed to (4x) growth solutions for 1 hour still result in wires templating to the surface individually with d$_{cc}$ distances greater than that of 7 nm (appendix B figure B.6).
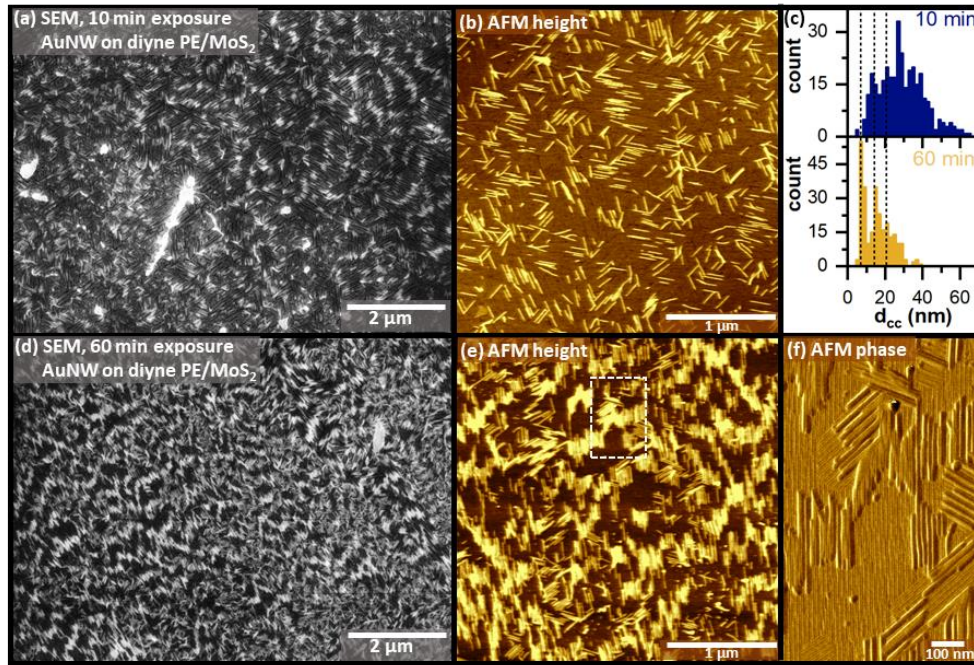
Figure 3.6 AuNW ribbon phases (4x) after 10 minute and 60 minute exposure times. SEM images right (a, d), AFM height images center (b, e), histogram of d_{cc} values top right (c), AFM phase bottom right (f).

3.3   Conclusion

Here, we find that striped phases of diyne PE on MoS_2 and HOPG are capable of ordering and straightening gold nanowires with various lengths. AuNWs form ribbon phases on diyne PE/MoS_2 substrates at wire lengths below 600 nm whereas ribbon phases occur on diyne PE/HOPG substrates at shorter lengths (~50 nm). This may be due to a decrease in the polarizability of the wire as it is shortened. The difference in the monolayer chemistry as well as the difference in the polarizability of the substrates could possibly play an important role in the formation of ribbon phases on the surface. Overall these results show the importance of the monolayer chemistry in efforts to control the assembly of wires overall large scales required for electronic applications.

3.4   Experimental methods

3.4.1   Materials

Oleylamine (technical grade, 70%), triisopropylsilane (TIPS, 98%), manganese chloride, and molecular sieves (4Å) were purchased from Sigma Aldrich (Saint Louis, MO) and used as received. Cyclohexane (HPLC grade), dry cyclohexane (99.5% extra dry, Acroseal), and gold tetrachloroauric acid trihydrate (ACS reagent grade) were purchased from Acros Organics (Fair Lawn, NJ) and used as received. 1,2-bis(10,12-tricosadiynoyl)-sn-glycero-3-phosphoethanolamine (diyne PE, > 99% purity) was purchased from Avanti Polar Lipids (Alabaster, AL). Highly ordered pyrolytic graphite (1 cm x 1 cm) was purchased from MicroMasch (Watsonville, CA). Molybdenum disulfide substrates were purchased from SPI Supplies (West Chester, PA). PElCO conductive liquid silver paint and double coated carbon conductive tape were purchased from Ted Pella, Inc (Redding, CA).

3.4.2   Langmuir-Schaefer (LS) conversion conditions

LS conversion was preformed using MicroTrough XL Langmuir-Blodgett trough (Kibron Inc., Helsinki, Finland). Diyne PE was deposited using 40 µL of a 0.5 mg/ml solution in chloroform was deposited on to a subphase of 5 mM $MnCl_2$ at 30 ℃. After deposition the small amount of chloroform was allowed to evaporate for 30 minutes, trough barriers were slowly moved inward (6.10 mm/min). Once the target surface pressure of 30 mN/m was reached the freshly cleaved HOPG that was heated to 50 ℃ using the thermal controlled dipping attachment was lowered horizontally into contact with the subphase (10 mm/min). The substrate was allowed to be in contact with the subphase for 2 min and then withdrawn from the inferface at the same speed.

LS conversion of diyne PE onto MoS_2 has slightly different conditions then mentioned above, if not mentioned below conditions remain the same. Diyne PE was deposited using 30 ul with an evaporation time of 15 mins. The barriers where moved inward at 8.5 mm/min until a target mean molecular area of 20 $Å^2$/chain was reach. Once reached the surface pressure was maintained (usually around 40 mN/m) freshly cleaved MoS_2 was lowered horizontally into contact with the subphase at speed of 6 mm/min.

All samples were dried with N_2 prior to polymerization. Diyne PE/HOPG samples were then photopolymerized for 1 h via irradiation while diyne PE/MoS_2 substrates where polymerized

for 10 minutes. All samples were polymerized under a 254-nm 8-W UW lamp with approximately a 4 cm distance between the sample and the lamp.

3.4.3   AuNW growth

In a typical reaction 2.5 mg $HAuCl_4 \cdot 3H_2O$ was added to 1.8 ml of dry cyclohexane, followed by 84 µl of oleylamine in the presence of molecular sieves. The solution was placed on a vortex and mixed for several seconds. Triisopropylsilane (120 µl) is added to the solution was once again mixed on the vortex until all the gold is dissolved. The growth solution is the placed in a humidity-controlled environmental chamber (1-10 % RH), and allowed to age for 12 h at ambient temperature. After aging the growth solution is diluted to a total dilution of 34x with dry cyclohexane. For wire assembly, both HOPG and MoS_2 substrates were lowered into contact with the growth solution. Substrates were then lifted out the growth solution and rinsed with 1 ml of cyclohexane and dried with N_2. Wire of varying length where synthesized by increasing the amount of cyclohexane to the reaction. All growth solution regardless of wire length were diluted to a total dilution factor of 34x. All substrates were stored at 4 ^0C following wire deposition.

3.4.4   AFM imaging

AFM imaging was performed under ambient conditions Agilent (Agilent, Palo Alto, CA) 5500 AFM. Imaging was performed in tapping mode with Bruker RFESP-75 and µmasch HQ:NSC18/No Al cantilevers (both having a nominal force constant 3 N/m and radius of curvature <10 nm).

3.4.5   SEM imaging

High resolution imaging of surface-templated AuNW arrays under high magnification was performed using a Teneo VS SEM (FEI Company, Hillsboro, OR) at a working distance of ~5.0 mm using the in-column Trinity detector T3. Beam currents in the range of 0.20-0.80 nA were selected for best resolution image acquisition through a 32 µm diameter aperture with an accelerating voltage of 5.00 kV. All substrates were affixed to standard SEM pin stub specimen mounts with conductive carbon tape. To further enhance substrate–mount conductivity, a small amount of colloidal silver paint (PELCO®, Ted Pella, Inc.) was applied along the perimeter of the HOPG and MoS_2 from the face down to the pin stub.

CHAPTER 4.   HEPTAMOLYBDATE: A HIGHLY ACTIVE SULFIDE OXYGENATION CATALYST

4.1   Introduction

The oxygenation of organic sulfides is a transformation key to medicinal chemistry,[14] petroleum desulfurization,[15] and nerve agent detoxification.[16–18] Highly relevant to the latter two applications are both the reaction rates and the use of inexpensive oxidants and catalysts. Hydrogen peroxide and tert-butyl hydroperoxide (TBHP) are among the desired oxidants because of their low costs and environmentally friendly nature.[118] Hydrogen peroxide is the most studied oxidant, and can be activated with a variety of transition metal based homogeneous catalysts. Among a plethora of catalysts reported,[119] homo- and hetero-polyoxometalates (POMs) stand out due to both the ease of preparation and their chemical robustness.[19–21] Recent examples of sulfide oxygenation catalyzed by both POMs and related species include the degradation of mustard agent simulants,[120–122] oxygenation of thioanisole with $(Bmim)_2[Mo_6O_{19}]$ (Bmim = 1-butyl-3-methylimidazolium),[123] conversion of 2-chloroethyl ethyl sulfide to its sulfoxide using $H_3PW_{12}O_{40}$ embedded in a MOF,[124] and the selective formation of sulfoxide as the precursor of vinyl glycine.[125] Contributions from our laboratory include the early demonstration of excellent chemical selectivity and efficient use of H_2O_2 in sulfide oxygenation using $[\gamma\text{-}SiW_{10}O_{34}(H_2O)_2]^{4-}$,[126] its subsequent heterogenization in amine functionalized MCM-41,[127] and the recent discovery of peroxo-dimolybdate as a highly efficient catalyst.[128]

Heptamolybdate, $[Mo_7O_{24}]^{6-}$ (also known as paramolybdate), is the lowest member of the isopolymolybdate family,[22] and its ammonium salt $((NH_4)_6[Mo_7O_{24}]$, 1a) is commercially available and inexpensive. While heteropolyoxometallates have attracted intense interest as oxygenation catalysts,[20,21] the role of heptamolybdate as an oxygenation catalyst has been sparingly explored. Noteworthy among a handful of examples using $[Mo_7O_{24}]^{6-}$ as a catalyst are the olefin epoxidation and alcohol oxidation by H_2O[129] and the conversion of dibenzothiophene and derivatives to corresponding sulfones by H_2O_2 in ionic liquid.[130] Also noteworthy is the ability

of heptamolybdate to promote hydrolysis of phosphoesters.[131] Reported herein are the preparation and structural characterization of a di-peroxo derivative of heptamolybdate, $[Mo_7O_{22}(O_2)_2]^{6-}$ (2^{6-}), and its activity in promoting sulfide oxygenation by H_2O_2. It was discovered in the process of performing control experiments that the parent heptamolybdate is a far more active catalyst. The reactivity scope, catalytic rates and the nature of the active species under the catalytic conditions were carefully examined.

4.2   Results and Discussion

4.2.1   Synthesis and structural identification of $[Mo_7O_{22}(O_2)_2]^-$ (2^{6-})

Curious about the nature of the active species in the aforementioned olefin epoxidation and alcohol oxidation reactions catalyzed by heptamolybdate,[129,132] we first sought to identify the predominant species produced upon treatment of $[Mo_7O_{24}]^{6-}$ with H_2O_2. Hence, an aqueous solution of $(NH_4)_6[Mo_7O_{24}]$ (**1a**) was treated with 10 equiv of H_2O_2 in the presence of 2.5 equiv guanidinium (CH_6N^{3+}) chloride, and $(NH_4)_4(CH_6N_3)_2[Mo_7O_{22}(O_2)_2]$ (**2a**) was isolated as yellow crystalline materials in a yield of 65% upon slow evaporation of the reaction mixture. X-ray diffraction study verified the above-mentioned formula of 2a with lattice water molecules. Compared to the parent ion $[Mo_7O_{24}]^{6-}$, one of the terminal oxos on both the Mo3 and Mo5 centers were replaced by a peroxo group in forming the di-peroxo heptamolybdate anion $[Mo_7O_{22}(O2)_2]^{6-}$, as shown in Figure 1. Both of the peroxo-bound molybdenum centers (Mo3 and Mo5) are seven-coordinated. The pentagonal bipyramidal arrangement of coordination is frequently observed in peroxo complexes. The bond lengths of the peroxo moiety in **2a** are 1.44(2) and 1.34(2) Å, respectively, falling in the expected range for Mo/W peroxo compounds.[133]
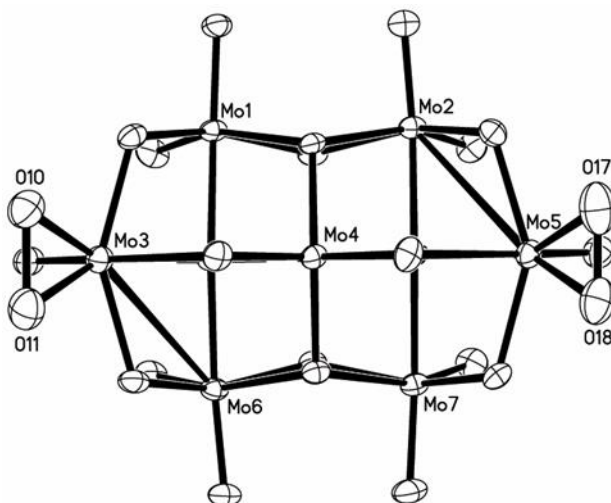
Figure 4.1 Structural plot of $[Mo_7O_{22}(O_2)_2]^{6-}$ in **2a**. Counter ions and lattice water molecules were omitted for clarity; the CIF has been deposited with the Cambridge Crystallographic Data Centre (CCDC 1839304).

4.2.2   Sulfide oxygenation activity of $[Mo_7O_{22}(O_2)_2]^{6-}$ and $[Mo_7O_{24}]^{6-}$

Upon the structural identification of the di-peroxo species $[\textbf{2}]^{6-}$, its activity in facilitating H_2O_2 oxygenation was examined with methyl phenyl sulfide (MPS, also known as thioanisole) as the substrate. With **2b** $((Bu_4N)_6[Mo_7O_{22}(O_2)_2])$ at 1 mol% loading and the use of two equiv of H_2O_2, MPS was completely consumed in 10 min as indicated by GC analysis (Table 4.1), demonstrating the efficacy of $[\textbf{2}]^{6-}$ in promoting H_2O_2 oxygenation. Furthermore, full conversion of MPS to sulfone (MPSO$_2$) was accomplished in 5h in the same reaction, indicating a 100% utility of active oxygen in H_2O_2. Previously, our laboratory reported that a divacant lacunary silicotungstate, $[\gamma\text{-}SiW_{10}O_{34}(H_2O)_2]^{4-}$, catalyzes H_2O_2 oxygenation of organic sulfides with a 100% utility of H_2O_2.[126] However, the catalytic reaction with divacant silicotungstate is significantly slower than those with **2b** even in the presence of the best co-catalyst, and the preparation of divacant silicotungstate is laborious. Clearly, **2b** is a simple and yet much more efficient catalyst for H_2O_2 oxygenation.

Encouraged by the performance of **2b**, the activity of heptamolybdate was examined in a control experiment. Similar to the conditions used with **2b**, MPS was treated with two equiv of H_2O_2 in the presence of 1 mol% $(Bu_4N)_6[Mo_7O_{24}]$ (**1b**). Surprisingly, **1b** is significantly faster than **2b**, consuming almost all MPS in 2 min with 100% consumption achieved in under 5 min (Table

1). It is clear from Table 4.1 that **1b** is also significantly faster than **2b** in converting sulfoxide (MPSO) to sulfone (MPSO$_2$).

Table 4.1 Sulfide oxidation of MPS catalyzed by **1b** and **2b**.

Time (min)	Catalyst	MPS (%)	MPSO (%)	MPSO$_2$ (%)
2	1b	1	71	28
	2b	37	60	3
5	1b	0	46	54
	2b	4	81	14
8	1b	0	40	59
	2b	1	79	20
10	1b	0	38	62
	2b	0	69	30
15	1b	0	29	71
	2b	0	56	44
30	1b	0	12	88
	2b	0	34	66
60	1b	0	2	98
	2b	0	16	84
120	1b	0	1	99
	2b	0	2	98
180	1b	0	1	99
	2b	0	1	99
240	1b	0	0	100
	2b	0	1	99
300	1b	0	0	100
	2b	0	0	100

[a] Each reaction was carried out with 0.50 mmol MPS, 1.0 mmol H$_2$O$_2$, and 0.0050 mmol **1b/2b** (1 mol% loading) in 5 mL CH$_3$CN at room temperature.

The fast oxygenation facilitated by **1b** also prompted further exploration into whether the oxygenation occurs in a stepwise fashion. The reaction was conducted at a reduced level of catalyst loading (0.2 mol% with respect to MPS), and the distribution of products was monitored with GC.

The resultant speciation curves are shown in Figure 4.2, which indicates the presence of MPSO$_2$ (*ca.* 20%) at the time of full consumption of MPS around 10 min. Clearly, the oxygenation catalyzed by **1b** is not step-wise. It is also apparent from Figure 4.2 that there is no observable induction period.
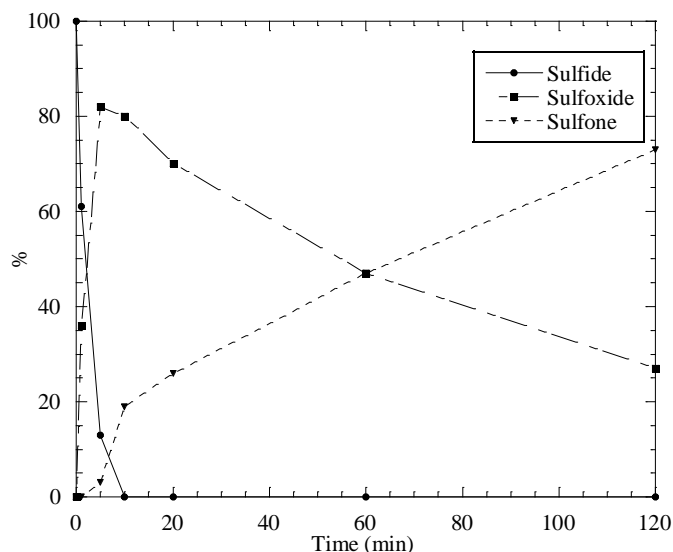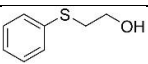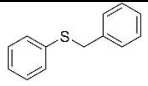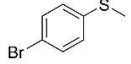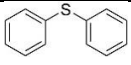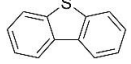
Figure 4.2 Speciation curve of H$_2$O$_2$-oxygenation of MPS catalyzed by 1b conducted with 0.50 mmol MPS, 1.0 mmol H$_2$O$_2$ and 0.0010 mmol 1b in 5 mL CH3CN at room temperature.

4.2.3 Catalytic oxygenation of other organic sulfides with [Mo$_7$O$_{24}$]$^{6-}$

Oxygenation of organic sulfides is relevant to current technologies such as the preparation of chiral sulfoxides in medicinal chemistry,[134] chemical degradation of *V*-type nerve agents,[135] and deep desulfurization of fossil fuels.[15] Hence, the proficiency of **1** in facilitating deep oxygenation was tested using a variety of sulfide substrates including DBT (dibenzothiophene), and results are collected in Table 4.2. All entries in Table 4.2 are equal in catalyst loading (0.1 mol%) and use of two equiv of H$_2$O$_2$ except DBT. It is clear from Table 4.2 that the fastest conversions to sulfone were accomplished within one hour for PTE (phenyl thioethanol) and BPS (benzyl phenyl sulfide), which are the most electron-rich among the substrates listed. Electron poor 4BT (4-bromothioanisole) and PPS (phenylsulfide) required longer reaction times to fully convert. Plausibly, the faster electrophilic oxygenation of the more electron rich sulfides resulted in a faster formation of sulfone. Being the most sterically hindered substrate DBT required a much longer

conversion time and H_2O_2 in 100% excess. DBT and its methyl derivatives, known as refractory sulphides, are the primary targets of fuel desulfurization,[15] and **1** could be a relevant catalyst. In addition, oxygenation of sulphides catalyzed by **2b** were carried out under the same conditions as those for reactions with **1b** and the times required for complete conversion to the corresponding sulphone (Table 4.2) are much longer than those with **1b**, consistent with the result of MPS oxygenation.

Table 4.2 Oxygenation of additional sulfides with **1b** and **2b** [a]

Sulfide	Abbreviation	H_2O_2 equiv	**1b** t/hr [b]	**2b** t/hr [b]
	PTE	2	1	2
	BPS	2	1	3
	4BT	2	2	4
	PPS	2	3.5	7
	DBT[c]	4	9	36

[a] The reaction was carried out with 0.5 mmol sulfide, 1.0 mmol H_2O_2 and 0.1 mol% **1b** / **2b** in 5 mL MeCN at 22 °C
[b] Time for complete conversion to sulfone.
[c] 4 equiv of H_2O_2 was used for the DBT reaction

4.2.4   Initial rate kinetics

Given the extraordinary efficiency of both $[\mathbf{1}]^{6-}$ and $[\mathbf{2}]^{6-}$ in promoting sulfide oxygenation and a potentially complex reaction mechanism due to their multinuclear nature, the reaction rate dependence on catalyst concentration was investigated based on the initial rate method. While both MPS (1.21 mM) and H_2O_2 (23 mM) were present in large excess in order to maintain pseudo first order conditions, the concentration of **1b** was varied from 0.003 mM to 0.036 mM (0.25 to 3.0 mol% loading with respect to MPS), and that of **2b** from 0.024 mM to 0.12 mM (2.0 to 10 mol% with respect to MPS). Monitoring the disappearance of MPS at 290 nm, the k_{obs} at a specific catalyst concentration was determined by fitting the first 15 min trace using a first order equation ($\ln(Abs)$ versus t), and the resultant k_{obs} vs. [cat] plots are shown in Figure 4.3 for both **1b** and **2b**. It is clear from Figure 4.3 that fitting both k_{obs} vs. [cat] data sets yielded excellent linear correlations,

and the slopes yielded k_{cat} values of 54 M^{-1}sec^{-1} and 19 M^{-1}sec^{-1} for **1b** and **2b**, respectively. Consistent with the data presented in Table 4.1, k_{cat}(**1b**) is significantly larger than k_{cat}(**2b**). Previously, k_{cat} for the same H_2O_2 oxygenation of MPS was reported to be about 11 M^{-1}min^{-1} for $[\{MoO(O_2)_2\}_2(\mu\text{-}O)]^{2-}$ by our laboratory[128] and 9.3 M^{-1}sec^{-1} for $[SeO_4\{\mu\text{-}WO(O_2)_2\}_2]^{2-}$ by Kamata *et al.*,[136] which were among the fastest oxygenation catalysts based on molybdates/tungstates. Clearly, heptamolybdate offers the advantage of being a superior catalyst without the requirement of elaborate synthesis.
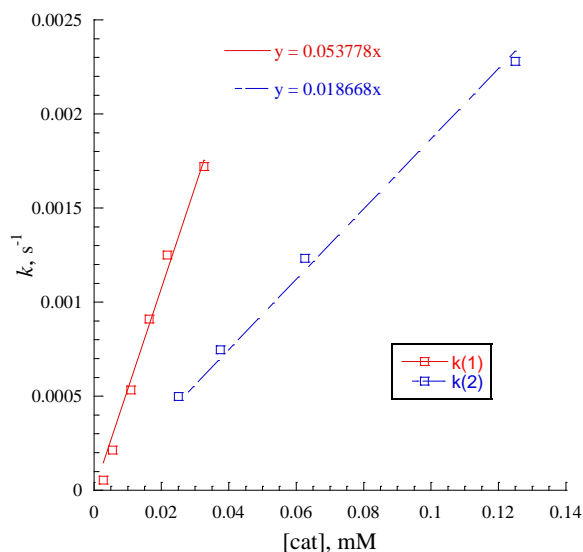
Figure 4.3 Rate dependence on the concentrations of **1b** (red) and **2b** (blue) under pseudo-first order conditions.

The significant contrast in k_{cat} between $[\mathbf{1}]^{6-}$ and $[\mathbf{2}]^{6-}$ may signal a difference in the active catalytic species. To gain an insight into the nature of possible active species, UV-vis spectra of **1b** and **2b** as pure compounds and in the presence of H_2O_2 in large excess were examined, and the results are shown in Figure 4.4. Compound **1b** (blue solid, **A**) has a broad peak with a λ_{max} of 220 nm, while compound **2b** displays a sharper peak with a λ_{max} of 252 nm (red solid, **C**). Upon the addition of H_2O_2 (232 equiv) to **1b** and a five min incubation time, the broad peak at 220 nm disappeared and a weaker, broader peak appeared at a λ_{max} of 330 nm (blue dash, **B**). Interestingly, the addition of H_2O_2 (232 equiv) to **2b** only led to a slight intensification of the 252 nm peak, but no new features. Clearly, while both **1b** and **2b** catalyze oxygenation reactions efficiently, the active species generated in the presence of excess H_2O_2 are different. More importantly, the treatment of **1b** with excess H_2O_2 does *not* result in **2b** *in acetonitrile*.

Figure 4.4 Absorption spectra in acetonitrile of **1b** before (**A**, 1.75 mM) and after the addition of 232 equiv of H_2O_2 (**B**); **2b** before (**C**, 3.27 mM) and after the addition of 232 equiv of H_2O_2 (**D**).

4.2.5   Identification of intermediates through mass spectrometry

It became clear from both the kinetics and UV-vis studies that the active intermediate is not the same for **1b** and **2b**. Hence, the *in situ* nano-electrospray ionization mass spectrometric (nanoESI-MS) technique[137,138] was utilized to identify the active intermediate(s) for both [**1**]$^{6-}$ and [**2**]$^{6-}$ under three sets of experimental conditions: (**I**) **1b** and **2b** alone in acetonitrile; (**II**) **1b** and **2b** with H_2O_2 in large excess in acetonitrile and (**III**) **1b** and **2b** with MPS and H_2O_2 in large excess, i.e. the conditions of a typical catalytic reaction.

The negative mode ESI-MS spectrum of neat **1b** in acetonitrile (Figure C.1 in appendix C) features major ion fragments $[Mo_4O_{13}]^{2-}$ (*m/z* 295.9), $[Mo_3O_{10}]^{2-}$ (*m/z* 225.0) and $[Mo_5O_{16}]^{2-}$ (*m/z* 368.4), while the parent ion $[Mo_7O_{24}]^{6-}$ (*m/z* 175.9) was not detected. Previously, Walanda *et al.* studied the aqueous solution of isopolyoxomolybdates using ESI-MS and reported the omnipresence of the $[Mo_mO_{3m+1}]^{2-}$ type ions and the detection of parent ion $[Mo_7O_{24}]^{6-}$ at pH = 6.[139] Our detection of $[Mo_3O_{10}]^{2-}$, $[Mo_4O_{13}]^{2-}$ and $[Mo_5O_{16}]^{2-}$ despite the difference in solvent conditions indicates a similar fragmentation pattern of $[Mo_7O_{24}]^{6-}$ in acetonitrile. The absence of the parent ion peak likely reflects the fragility of $[Mo_7O_{24}]^{6-}$ in a non-aqueous media. The negative mode ESI-MS spectrum of neat **2b** (Figure C.2 in appendix C) contains a noteworthy fragment corresponding to $[Mo_2O_{11}]^{2-}$ (*m/z* 183.8), and it does not display any of the significant ion fragment peaks identified for **1b**.
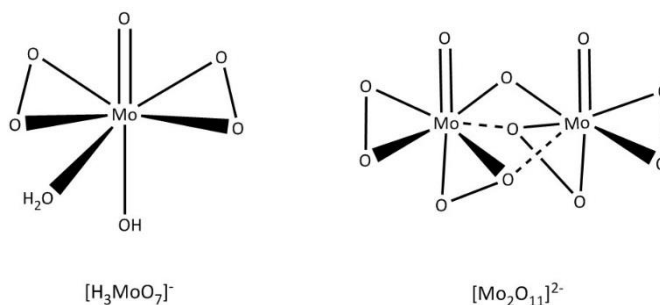
Figure 4.5 Peroxy-intermediate derived from $[Mo_7O_{24}]^{6-}$

The negative mode ESI-MS spectrum of **1b** in the presence of 100-fold H_2O_2 was acquired to gain insight into the interaction between H_2O_2 and isopolymolybdate species, as well as the likely resultant species. Strikingly but unsurprisingly, most of the afore-mentioned $[Mo_mO_{3m+1}]^{2-}$ type ions vanished with $[Mo_4O_{13}]^{2-}$ remaining as the only observable member. The spectrum (Figure 4.5a) features three main ions at *m/z* values of 183.8, 191.8 and 210.8, which correlate respectively to the $[Mo_2O_{11}]^{2-}$, $[HMoO_6]^-$ and $[H_3MoO_7]^-$. Interestingly, the $[Mo_2O_{11}]^{2-}$ ion (see figure 4.5) was previously prepared and characterized as an active catalyst for H_2O_2 oxygenation by our laboratory.[128] The appearance of both $[H_3MoO_7]^-$ (Scheme 1) and $[HMoO_6]^-$ is also noteworthy, as the former is a member of the Mimoun species, i.e. $M(=O)(\eta^2\text{-}O_2)_2(H_2O)_2$ (M = Cr, Mo and W),[140,141] and the latter is its dehydrated form. As shown in Figure B.3, collision-induced dissociation (CID) of the ion at *m/z* 210.8 ($[H_3MoO_7]^-$) produced a loss of water (-18 Da), further corroborating the aforementioned assignments of $[HMoO_6]^-$ and $[H_3MoO_7]^-$. It is noteworthy that the $[Mo_2O_{11}]^{2-}$ peak also appeared in the ESI-MS spectrum of **2b** in the presence of H_2O_2 (Figure B.4), but in significantly reduced abundance (BPI = 32.7%). The *in situ* ESI-MS technique was finally extended to the catalytic oxygenation of MPS, namely a solution containing MPS and H_2O_2 in 1:1 mole ratio and 1mol% of **1b**. Similar to the spectrum obtained in **II**, the predominant species observed are $[HMo_2O_{11}]^-$, $[HMoO_6]^-$ and $[H_3MoO_7]^-$ with respective BPIs of 49.4%, 31.7% and 19.4% shown in Figure 4.5b. Interestingly, the most abundant species (BPI = 100%) from experiment **III** is $[Mo_4O_{13}]^{2-}$ (*m/z* 295.9), which is also present in spectrum **II** but at a much lower abundance (BPI = 16.7%, see Figure 4.5a). For comparison purpose, ESI-MS spectrum of **2b** under catalytic conditions was also taken (Appendix C Figure C.5), which reveals the presence of $[H_3MoO_7]^-$ and $[HMo_2O_{11}]^-$ similar to the case of **1b** at relatively low BPI percentages of 6.99 and

20.06%, respectively. This result indicated that the lower activity of **2b** is likely due to the insufficient production of $[Mo_2O_{11}]^{2-}$ ion.

a)

Ion Observed	m/z	% BPI
$[Mo_2O_{11}]^{2-}$	183.8	100
$[HMoO_6]^-$	191.8	64.79
$[H_3MoO_7]^-$	210.8	37.56
$[Mo_4O_{13}]^{2-}$	295.9	16.74

b)

Ion Observed	m/z	% BPI
$[HMoO_6]^-$	191.8	31.66
$[H_3MoO_7]^-$	210.8	19.38
$[Mo_4O_{13}]^{2-}$	295.9	100
$[HMo_2O_{11}]^-$	369.9	49.41
$[Mo_6O_{19}]^{2-}$	440.3	11.69
$[HMo_3O_{10}]^-$	447.7	12.72
$[HMo_4O_{13}]^-$	591.6	10.06
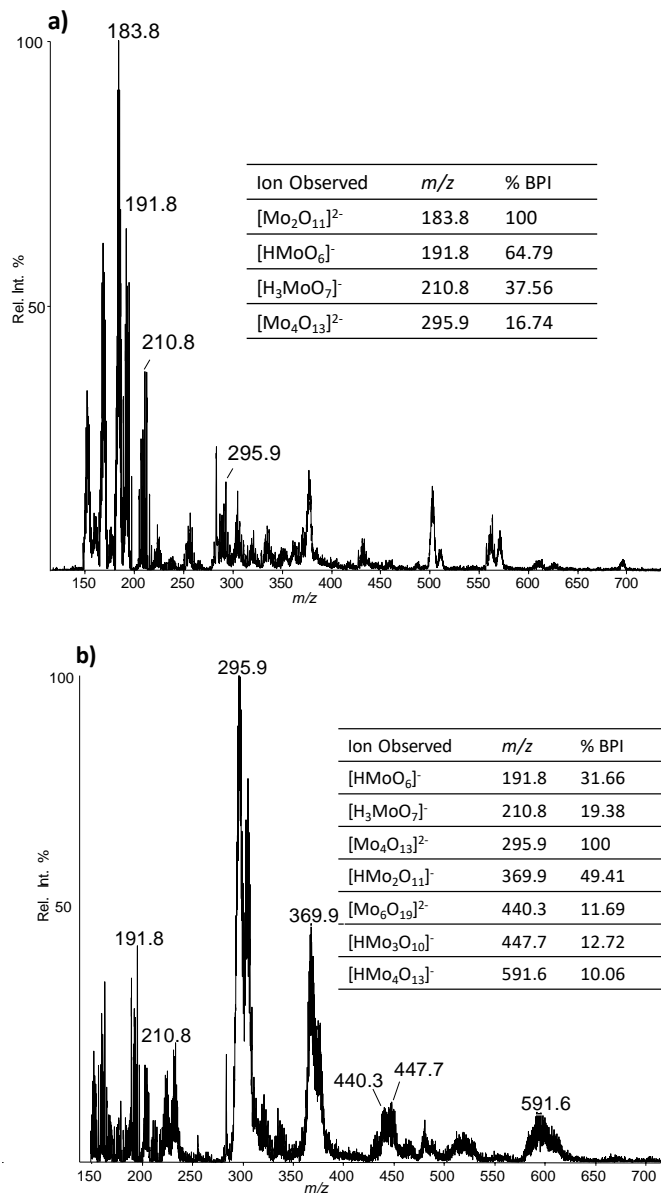
Figure 4.6 NanoESI mass spectra of **1b** (a) 1 min after the addition of H_2O_2; (b) 1 min after the addition of both H_2O_2 of MPS.

4.3   Conclusion

It has been shown in this contribution that commodity chemical heptamolybdate is a highly efficient catalyst for hydrogen peroxide oxygenation of organic sulfides in terms of both the

reaction rate and the hydrogen peroxide utility (100%). Electrospray ionization mass spectrometry studies revealed that the heptamolybdate ion undergoes significant fragmentation under the catalytic reaction conditions. One of the major ions detected in ESI-MS, $[Mo_2O_{11}]^{2-}$, has been identified as the main active species based on the consideration of catalytic rates. Our success herein will hopefully encourage further applications of ESI-MS and other MS techniques[142,143] in polyoxometallate catalysis.

4.4 Experimental Methods

4.4.1 Materials and Instrumentation

Acetonitrile, ammonium heptamolybdate tetrahydrate and guanidine hydrochloride were purchased from Sigma Aldrich. Tetra-*n*-butylammonium bromide was purchased from Alfa Aesar. Methyl phenyl sulfide, phenyl sulfide, benzyl phenyl sulfide, 4-bromothioanisole, phenylthioethanol and dibenzothiophene were purchased from ACROS Organics. Hydrogen peroxide (30%) was purchased from Macron Fine Chemicals and standardized via iodometric titration. Oxygenation reaction samples were analyzed using an Agilent 7890A GC system equipped with a flame ionization detector. The separation of substrate and products was achieved using an Agilent HP-5 column with dimensions of 30 m x 0.320 mm with 25 micron film thickness. Reaction progress was monitored at 290 nm via UV-Vis spectroscopy on a JASCO V-670 Spectrophotometer.

4.4.2 Synthesis of (n-Bu$_4$N)$_6$[Mo$_7$O$_{24}$] (1b)

Ammonium heptamolybdate tetrahydrate (500 mg, 0.405 mmol) was dissolved in water (4 mL). In a separate round bottom flask tetrabutylammonium bromide (0.789 g, 2.43 mmol) was dissolved in water (4 mL). The two solutions were mixed together and stirred for 10 minutes, with a white precipitate forming immediately. The precipitate was allowed to settle in the vial and collected by filtration and dried. Yield: 81% based on Mo.

4.4.3 Synthesis of (n-Bu$_4$N)$_6$[Mo$_7$O$_{22}$(O$_2$)$_2$]·nH$_2$O (2b)

Ammonium heptamolybdate tetrahydrate (2.472 g; 2.0 mmol) was dissolved in 20 mL water, to which were slowly added with stirring 2.0 mL 30% hydrogen peroxide (20 mmol) and tetrabutylammonium bromide (4.832 g, 15 mmol) in 10 mL water. After 30 min, the yellow

precipitate was collected by filtering through a sintered glass filter, washed with 20 mL water, and air dried to afford powder samples 3.98 g of 2b (yield 78% based on Mo). Elemental analysis calcd (%) for $C_{96}H_{216}N_6Mo_7O_{26}$: C, 45.4; H, 8.6; N, 3.3; Mo, 26.4. Found (%):C, 43.8; H, 9.0; N, 3.1; Mo, 25.6. IR for 1 (KBr, cm^{-1}): 3394 (s), 2964 (m), 2940 (m), 2874 (m), 1647 (m), 1483 (m), 1460 (m), 1381 (m), 1348 (w), 1281 (w), 1152 (w), 1158 (w), 1069 (w),1030 (w), 1004 (w), 949 (m), 922 (s), 903 (s), 852 (s), 797 (vs), 730 (s), 657 (vs), 583 (s), 556 (s).

4.4.4   Catalytic conversion of sulfide

The catalyst (**1b**⁄**2b**) (0.005 mmol, 1 mol%) was dissolved in 5 mL of acetonitrile. Substrate sulfide (0.5 mmol) and internal standard 1,2-dichlorobenzene (0.4 mmol) were added to the reaction solution. H_2O_2 (1 mmol) was added to the solution drop wise, and the solution turned yellow. In the case of DBT additional equivalents of H_2O_2 (2 mmol total) were added in order to achieve complete conversion. Aliquots were taken at different time periods, quenched using MnO_2, and analyzed using GC.

4.4.5   Initial rate kinetics of **1b** and **2b**

Standard acetonitrile solutions utilized were prepared for **1b** at 1.75 mM, **2b** at 3.27 mM, MPS at 39 mM, and hydrogen peroxide at 0.37 M. Solutions for kinetic studies were prepared combining 200 µL of MPS and a specific volume of **1b** in a quartz cuvette, the volume of which was adjusted to 3.22 mL with additional acetonitrile. The reaction was initiated by the addition of 200 µL of the H_2O_2 stock solution. The absorbance of the solution at 290 nm was measured every 20 seconds for 30 minutes. The initial *in situ* concentrations upon the addition of H_2O_2 to the cuvette are 2.43 mM for MPS, 23 mM for H_2O_2, with a range of concentrations for **1b** (0.027-0.0326 mM) or **2b** (0.025-0.125 mM).

4.4.6   Nano-electrospray ionization mass spectra of 1b and 2b

For a typical measurement, a 5 mL solution of **1b** or **2b** (0.005 mmol in acetonitrile), 59 µL of MPS (0.5 mmol in acetonitrile) and 51 µL of H_2O_2 (0.5 mmol in acetonitrile) were combined. These same concentrations and volumes were used for the neat **1b/2b** (Experiment **I**) and **1b/2b** plus H_2O_2 (Experiment **II**) spectra collected**.** An aliquot (5 µL) was removed and promptly diluted in 1 mL acetonitrile, then sprayed using a home-built nano-ESI source.[137] All ESI-MS experiments for **1b** were performed in the negative ion mode on a 4000 QTRAP triplequadrupole/linear ion

trap mass spectrometer (Sciex, Toronto, Canada). The characteristic parameters of the MS during this study were set as follows: spray voltage, 1500 V; curtain gas, 5 psi; declustering potential (DP), 20 V. Mass analysis was achieved by using Q3 as a linear ion trap at a scan rate of 1000 Da/s. Data shown here were typically averages of 50 scans. ESI-MS experimental conditions for **2b** are provided in the supplementary information. Data acquisition, processing, and instrument control were performed using Analyst 1.6 software.

APPENDIX A. CHAPTER 2 SUPPORTING INFORMATION

A version of this appendix was submitted for publication as Supplementary Information in *Chem.*

A.1 AFM images comparing AuNW assembly on diyne PE, 4,6-PCD-NH$_2$, and bare HOPG.

In the main manuscript, Figure 2 shows AFM images of AuNWs assembled on a diyne PE template and on bare HOPG. Here, we additionally show results of assembling AuNWs on 4,6-PCD-NH$_2$, which lacks a headgroup dipole. Line scans across groups of wires on diyne PE and 4,6-PCD-NH$_2$ in the bottom panel illustrate that the local center-to-center distance on diyne PE is 15 nm (approximately 2x the template pitch, while the center-to-center distance on 4,6-PCD-NH$_2$ is 7 nm (similar to the template pitch). On bare HOPG, bundles of wires are observed; in some cases, filled vacancies between wire bundles appear to be domains of standing phase OM.
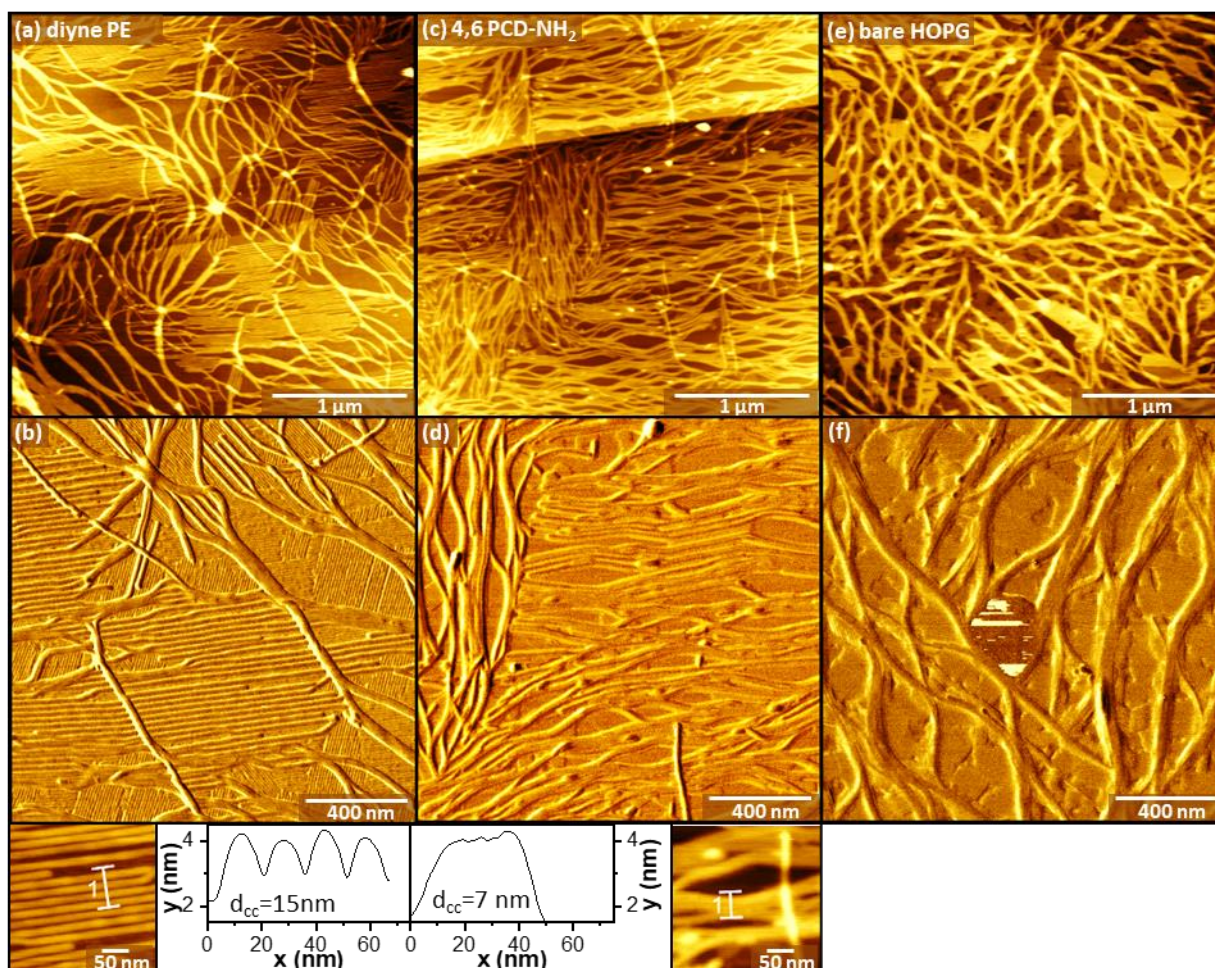
Figure A.1 Comparison of long AuNW assembly on template substrates. AFM images of AuNW assembled on (a,b) a striped diyne PE template, (c,d) a 4,6-PCD-NH$_2$ template, and (e,f) bare HOPG. Line scans taken from images (a) and (b) illustrate the difference in center-to-center distance for wires assembled on diyne PE and 4,6-PCD-NH$_2$.

A.2   SEM images of AuNW assembled on diyne PE templates

In the main manuscript, Figure 2.3g shows an SEM image of AuNWs assembled on a diyne PE template. Here se show the original image at larger scale (Figure A.1.2), as well as higher-resolution images (Figures A.1.3 and A.1.4) of similar areas that illustrate the separation of the AuNWs on the surface, as well as the difference in AuNW grouping when the AuNW long axes are aligned along vs. across the template stripe direction.
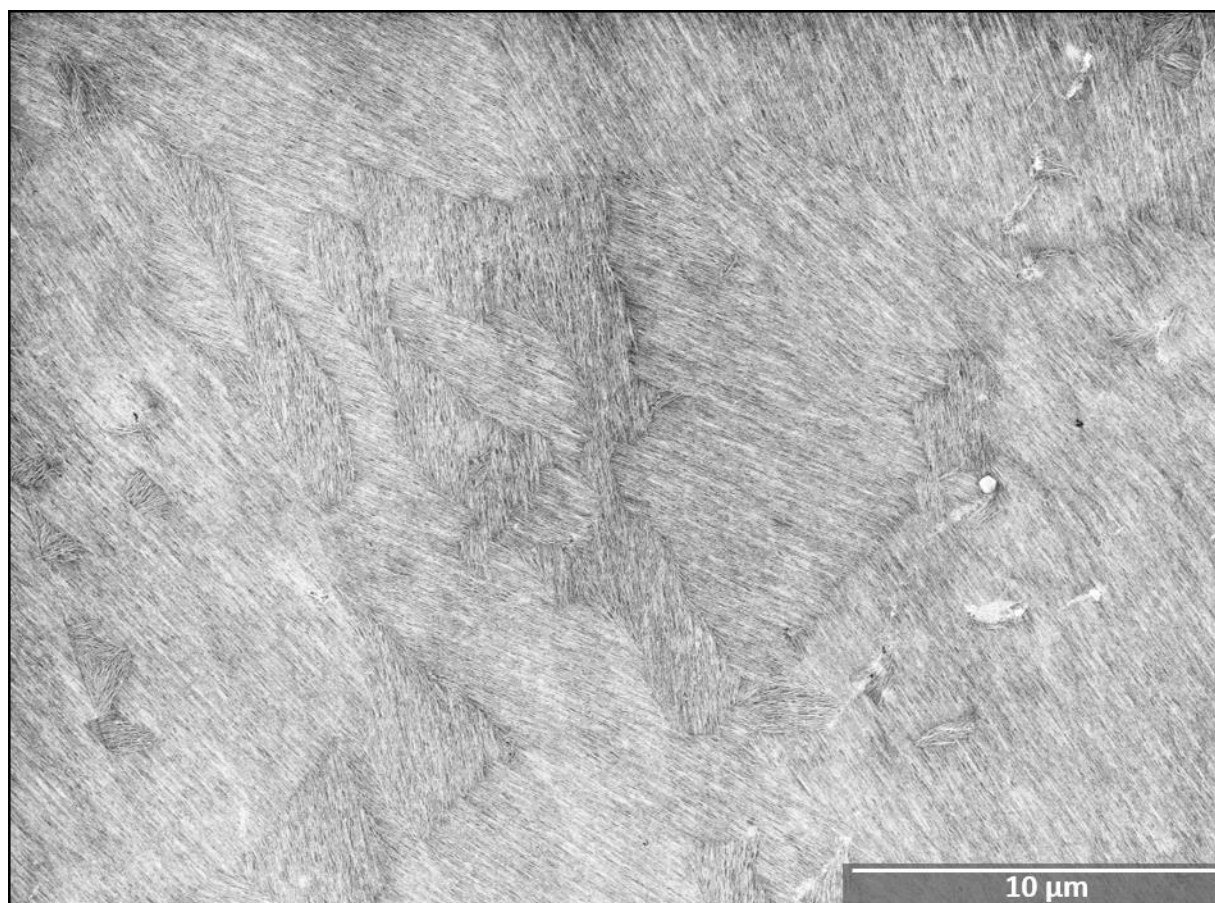
Figure A.2 Large-area SEM image of AuNWs assembled on diyne PE template.
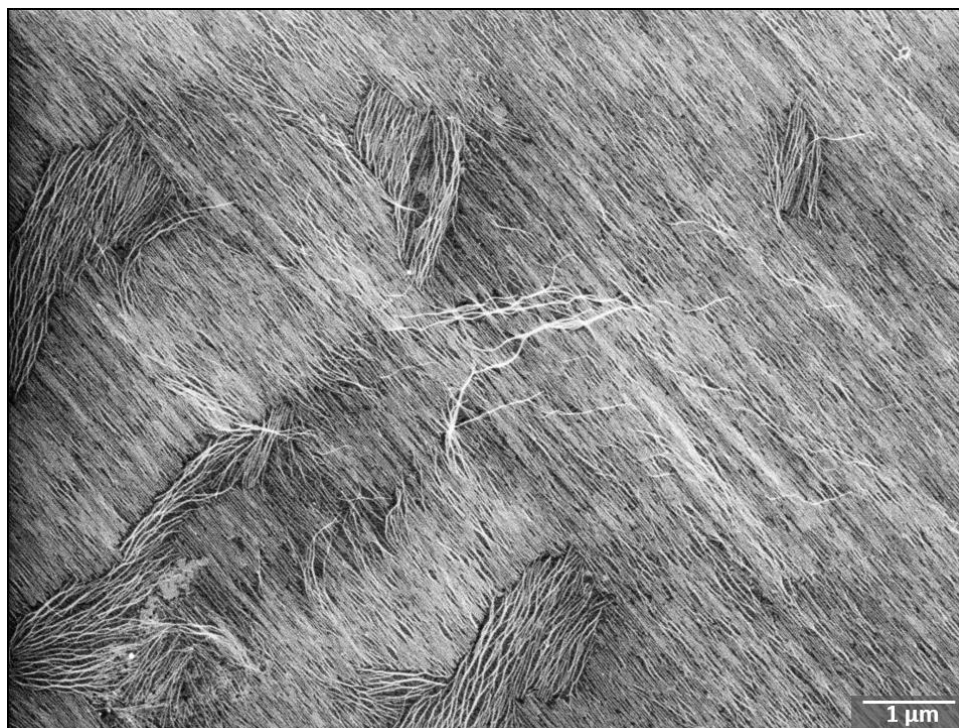
Figure A.3 Higher-resolution SEM image of AuNW on diyne PE.
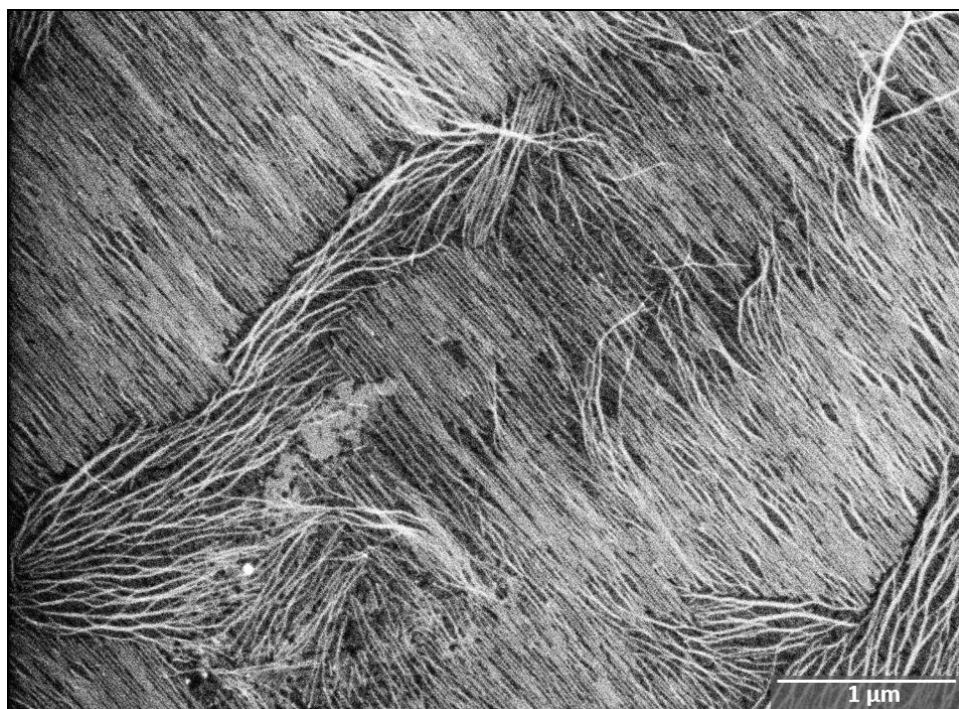
Figure A.4 High-resolution SEM image of AuNW on diyne PE illustrating differences in wire grouping when wires align with or across the template stripe direction.

APPENDIX B. CHAPTER 3 SUPPORTING INFORMATION
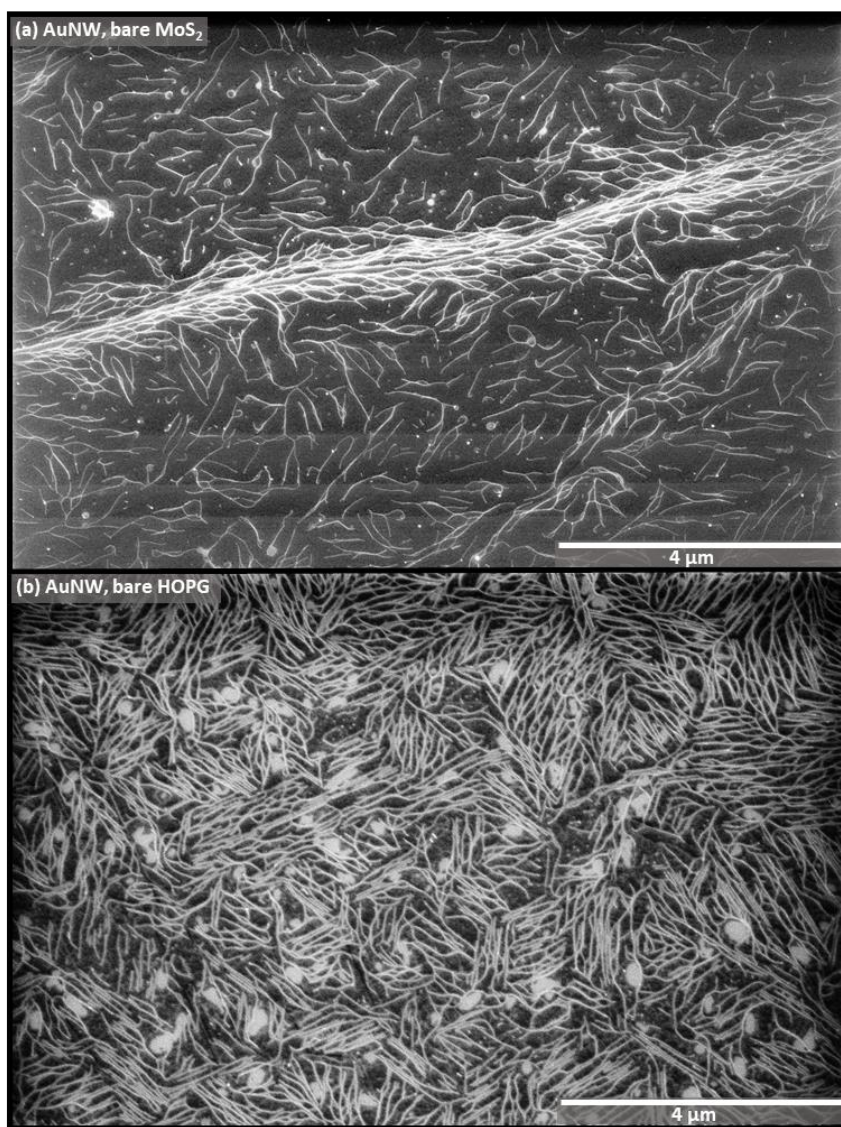
Figure B.1 SEM images of AuNW growth solution exposed to (a) bare MoS_2 and (b) bare HOPG.
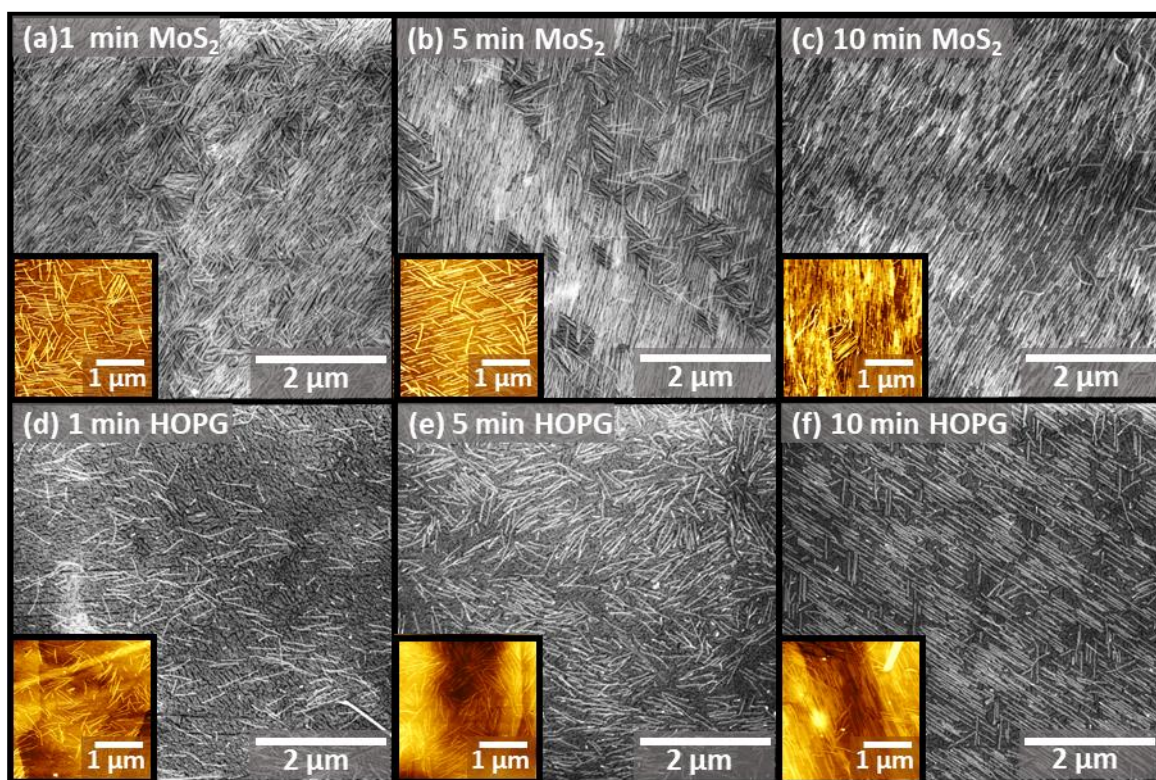
Figure B.2 AuNW adsorption at 1 min, 5 min, and 10 min exposures on both diyne PE MoS$_2$ and HOPG.

Figure B.3 SEM image of AuNW adsorption at 200x dilution with 1-minute exposure on diyne PE/MoS$_2$.

(a) 200x, 5 min exposure PE/HOPG

4 µm
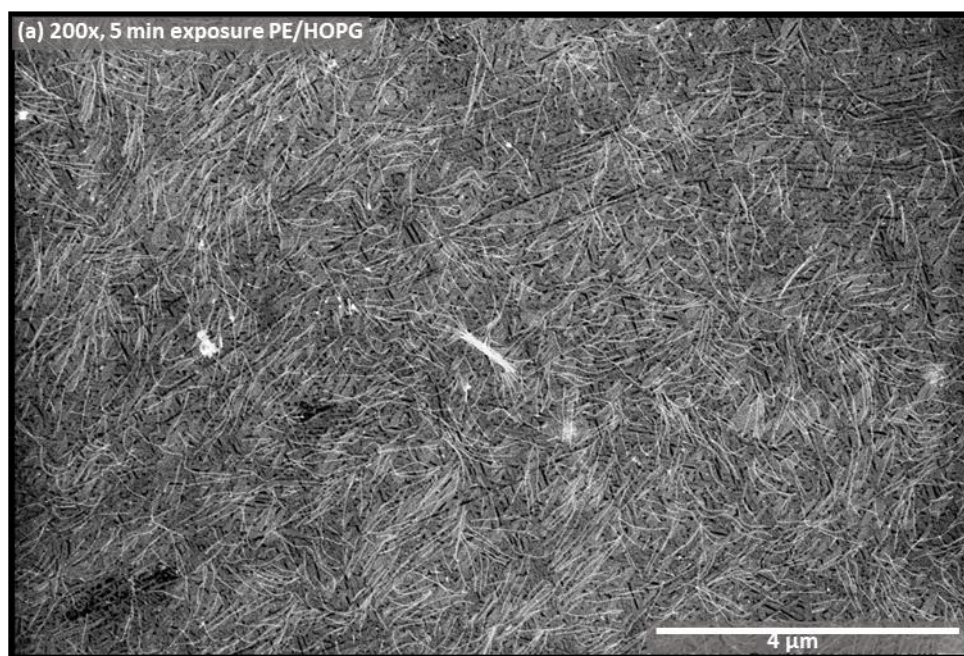
Figure B.4 SEM image of AuNW on diyne PE/HOPG at 200x dilution after a 1 minute exposure.
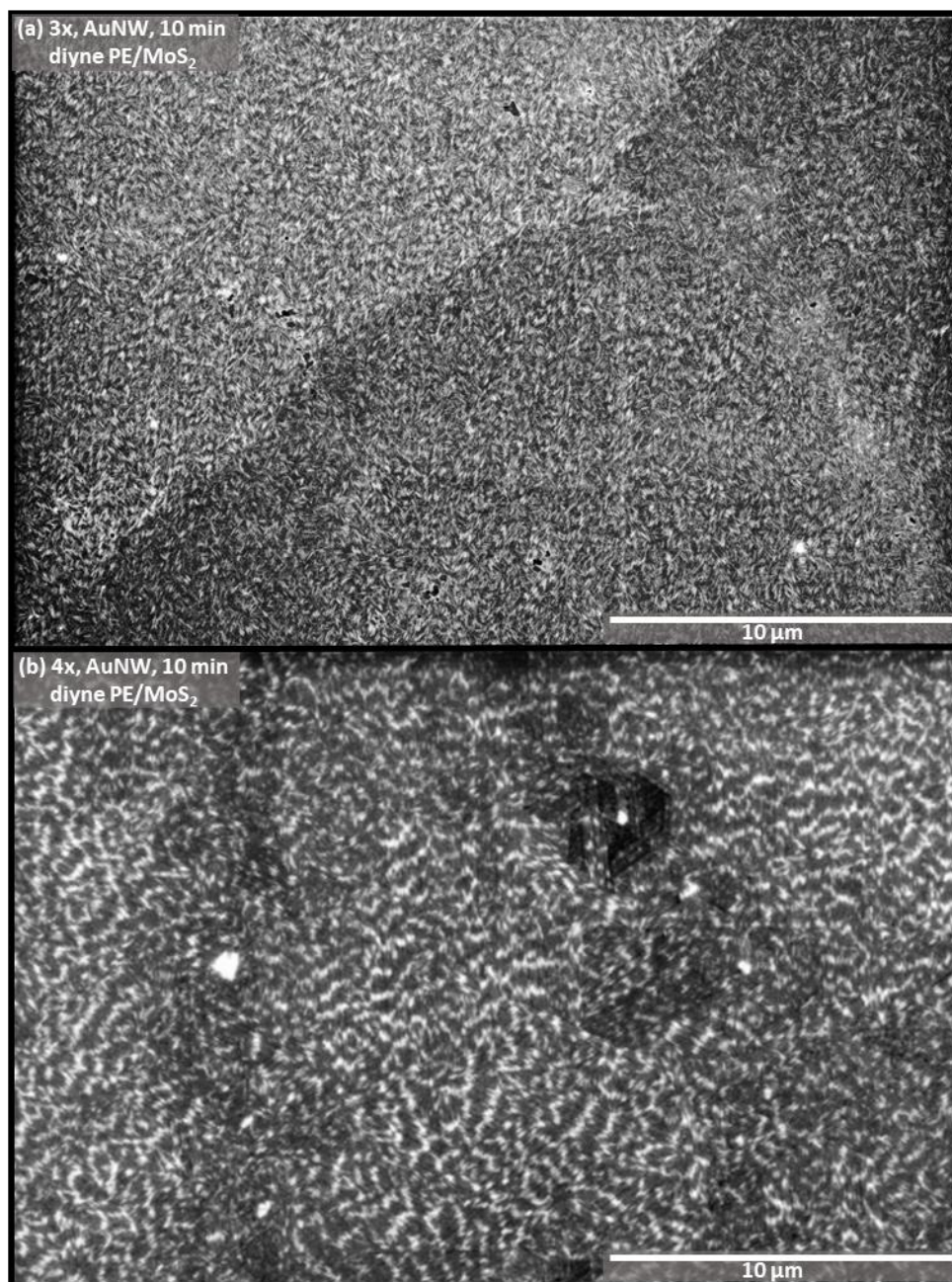
Figure B.5 Large area SEM images of AuNWs on diyne PE/MoS_2 at 3x dilution (a) and 4x dilution (b).
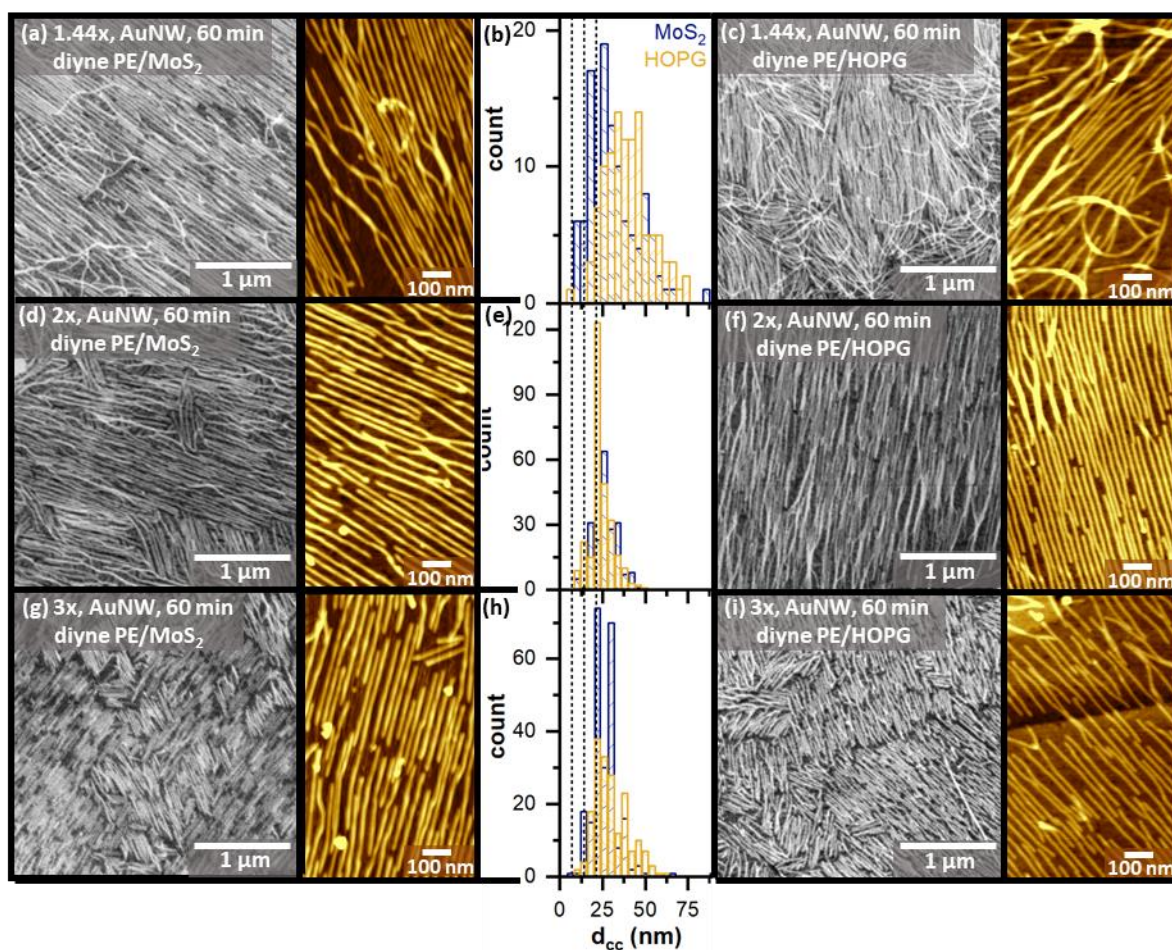
Figure B.6 Images of AuNW assembly on diyne PE/MoS$_2$ after 10 minutes at 1.45 x (a), 2x (d), and 3x (g). Wire-wire distances at various dilutions factors 1.45x (b), 2x (e), and 3x (h). Images of AuNW assembled on diyne PE/HOPG after 10 minutes 1.45 x (c), 2x (f), and 3x (i).

APPENDIX C. CHAPTER 4 SUPPORTING INFORMATION
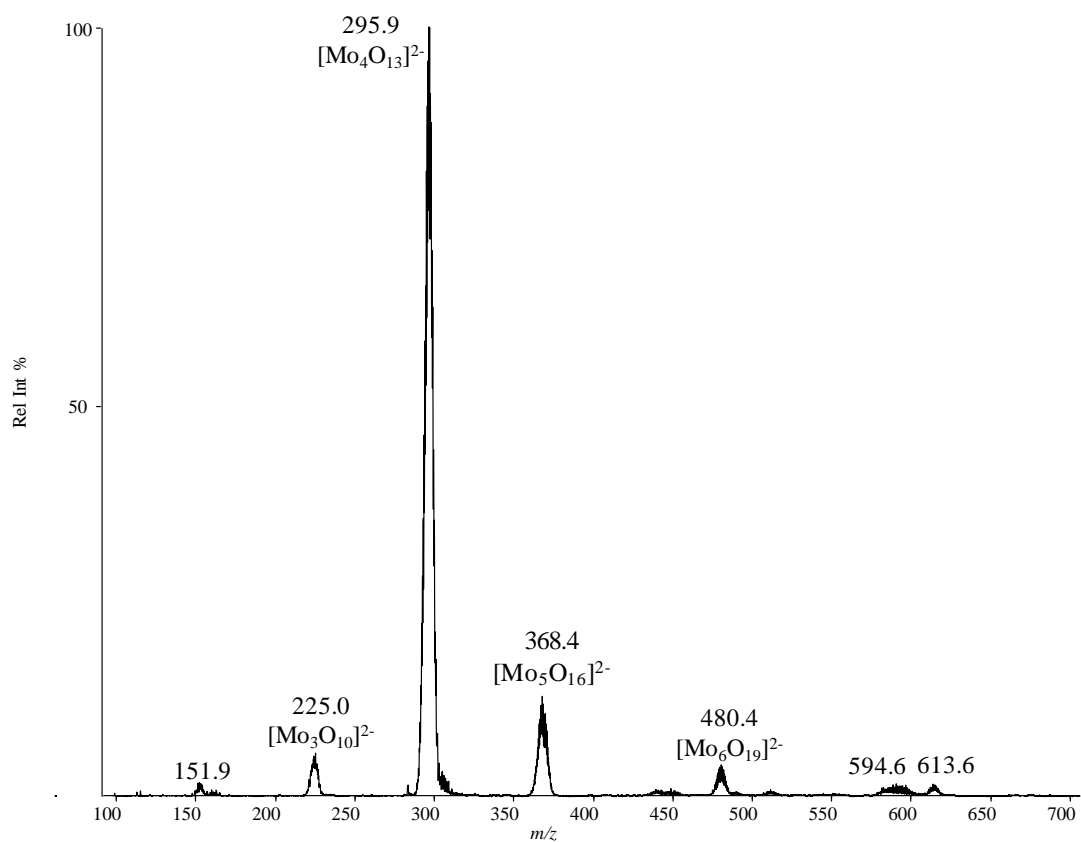
Figure C.1 NanoESI mass spectrum of $[Mo_7O_{24}]^{6-}$ (0.034 nmol) in MeCN solution in the negative ion mode.

Ion Observed	m/z	% BPI
$[Mo_2O_{11}]^{2-}$	183.8	11.85
$[H_3Mo_2O_{13}]^{2-}$	204.0	6.33
$[Mo_6O_{23}]^{3-}$	317.2	21.91
$[Mo_9O_{33}]^{4-}$	349.0	100
$[Mo_9O_{37}]^{4-}$	363.0	56.82
$[Mo_5O_{17}]^{2-}$	377.0	39.61
$[Mo_5O_{21}]^{2-}$	406.9	33.60
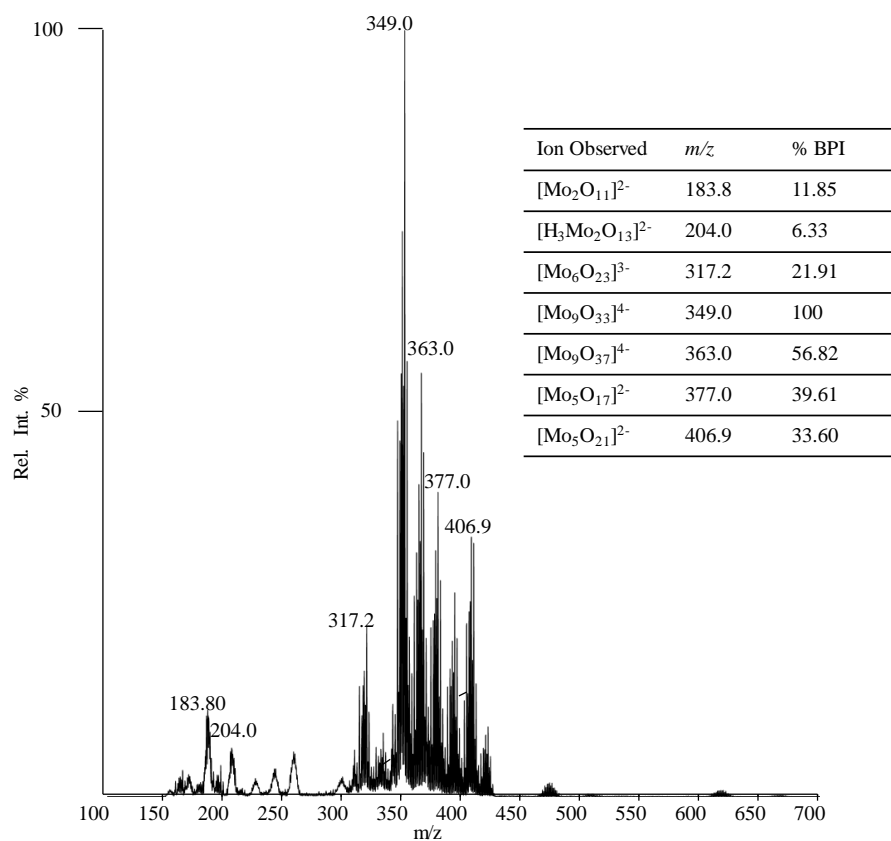
Figure C.2 NanoESI mass spectrum of $[Mo_7O_{22}(O_2)_2]^{6-}$ **2b** (0.034 nmol) in MeCN solution in the negative ion mode.
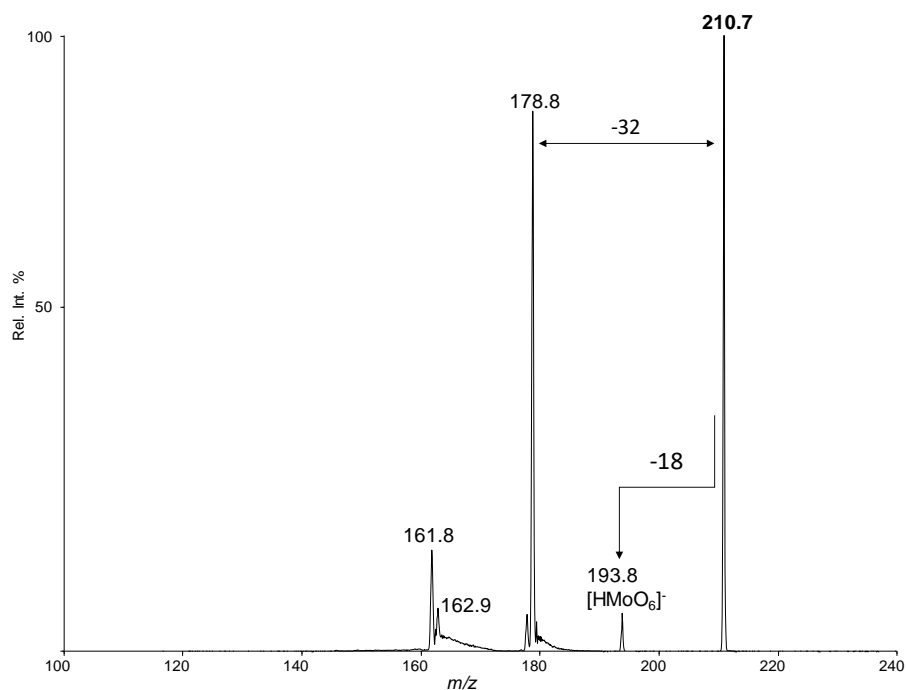
Figure C.3 Tandem mass spectrum of the peak at *m/z* 210.7 via collision-induced dissociation from Figure 5b. Collision-induced dissociation (CID) was performed using beam type CID. Beam-type CID was performed by precursor ion selection in Q1, ion acceleration for fragmentation in q2 collision cell and followed by fragment analysis in Q3 linear ion trap. Collision energy (CE) of 25 V was used for analysis. m/z range of 100-1000 Da was used.

Ion Observed	m/z	% BPI
$[Mo_2O_{11}]^{2-}$	183.8	100
$[HMoO_6]^-$	191.8	38.72
$[H_3MoO_7]^-$	210.8	6.99
$[Mo_6O_{23}]^{3-}$	317.2	8.40
$[Mo_9O_{33}]^{4-}$	349.0	40.4
$[HMo_2O_{11}]^-$	369.9	20.06
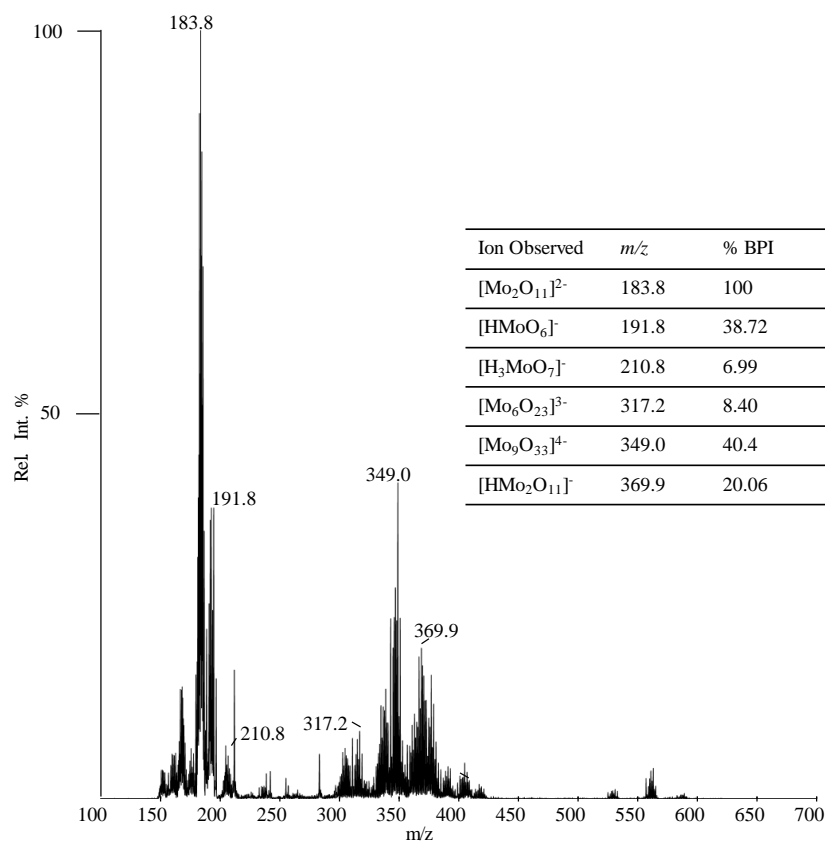
Figure C.4 NanoESI mass spectra of **2b** 1 min after the addition of H_2O_2.

Ion Observed	m/z	% BPI
[Mo$_2$O$_{11}$]$^{2-}$	183.8	100
[HMoO$_6$]$^-$	191.8	38.72
[H$_3$MoO$_7$]$^-$	210.8	6.99
[Mo$_6$O$_{23}$]$^{3-}$	317.2	8.40
[Mo$_9$O$_{33}$]$^{4-}$	349.0	40.4
[HMo$_2$O$_{11}$]$^-$	369.9	20.06
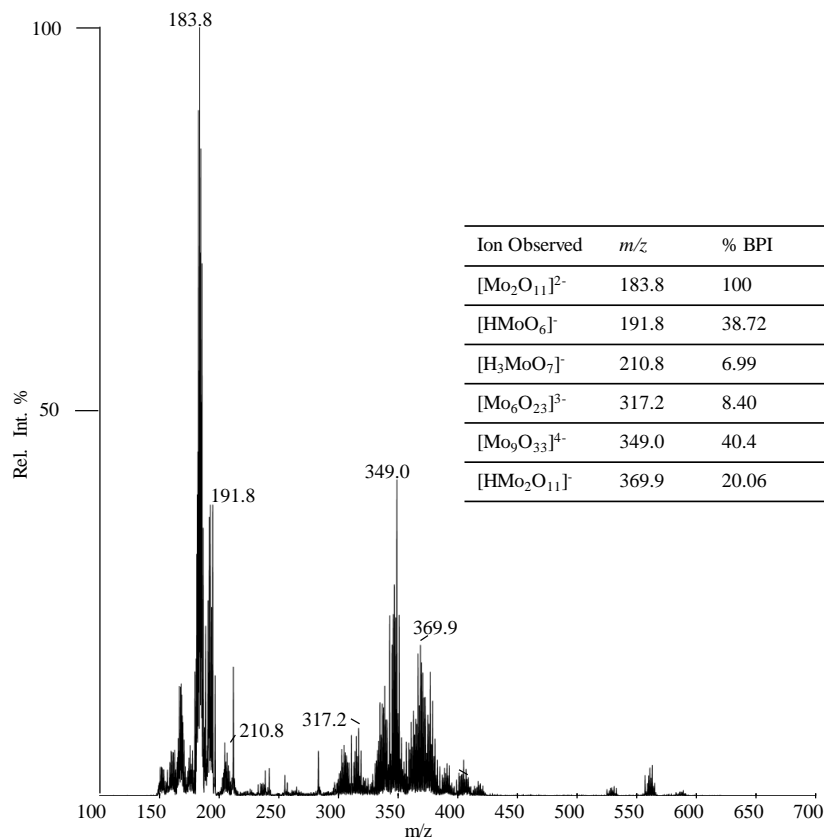
Figure C.5 NanoESI mass spectra of **2b** 1 min after the addition of both H$_2$O$_2$ and MPS.
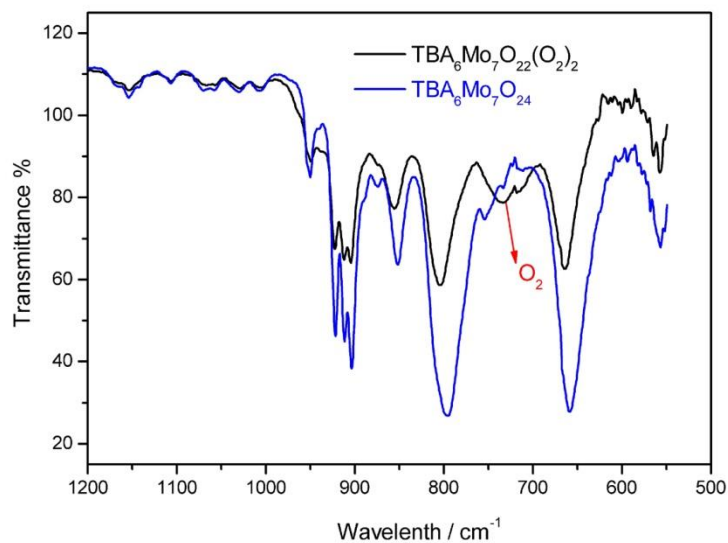
Figure C.6 FT-IR spectra of **1b** and **2b**

C.1 Instrumental information for all ESI-MS of **2b**

All the MS data were collected using a QTRAP 4000 hybrid triple quadrupole/linear ion using nano-electrospray ionization in the negative ion mode. The characteristic parameters of the MS were: spray voltage, -1400-1600 V, curtain gas, 20 psi; declustering potential (DP), 20V. Data shown here were typically averages of 50-100 scans. MS1 mass analysis was performed in LIT mode in Q3. Data acquisition, processing, and instrument control were performed using Analyst software.

C.1 Crystallographic Details

Crystallization: Ammonium molybdate tetrahydrate $(NH_4)_6Mo_7O_{24}\cdot4H_2O$ 2.472 g (2.0 mmol) was dissolved in 20 mL water, then excessive 30% hydrogen peroxide 2.0 mL (20 mmol) and $CH_5N_3\cdot HCl$ 0.478 g (5.0 mmol) were added. The resultant reaction mixture was further stirred for 1h. After filtration, the yellow filtration was sealed by parafilm with a few tiny pores and very slowly evaporated at the room temperature. Two weeks later, yellow single-crystalline blocks suitable for X-ray crystallography products were obtained and afforded powder samples 1.687 g (yield 65% based on Mo)

Structural characterization: Crystal structure of compound **2a** consists of heptamolybdate anion, two guanidine $CH_6N_3^+$, four ammonium NH_4^+ cations and lattice water molecules. The heptamolybdate $Mo_7O_{24}^{6-}$ is well-known as the fundamental units in the polyoxomolybdate anions. The molybdenum atom coordinated by peroxo group was hepta-coordinated. The pentagonal bipyramidal arrangement of coordination was frequently observed in peroxo complexes. The bond distances of the peroxo groups in **2a** are 1.443(16) and 1.342(19) Å, respectively, falling in the range of peroxo compounds.

Crystal data for **2a**: Monoclinic, space group $P21/c$, a = 13.6678(14) Å, b = 10.8474(11) Å, c = 30.014(3) Å, β = 113.895(4), V = 4068.5(7) Å^3, Z = 4, ρ_{calcd} = 2.102 g·cm^{-3}, μ = 2.178 mm^{-1}. A single crystal of dimensions 0.35 x 0.28 x 0.24 mm^3 for 1 was selected for indexing and intensity data collection on a Bruker SMART APEX CCD diffractometer using graphite-monochromatized Mo Kα radiation (λ = 0.71073 Å) at room temperature. Numbers of collected and observed independent [I > 2σ(I)] reflections are 21742 and 6213 (R_{int} = 0.038). Full matrix least-squares refinements were based on F^2 and converged at R$_1$ = 0.0599 and wR$_2$ = 0.1878.

REFERENCES

(1)   Mann, J. A.; Dichtel, W. R. Noncovalent Functionalization of Graphene by Molecular and Polymeric Adsorbates. *J. Phys. Chem. Lett.* **2013**, *4* (16), 2649–2657.

(2)   MacLeod, J. M.; Rosei, F. Molecular Self-Assembly on Graphene. *Small* **2014**, *10* (6), 1038–1049.

(3)   Huang, X.; Qi, X.; Boey, F.; Zhang, H. Graphene-Based Composites. *Chem. Soc. Rev.* **2012**, *41* (2), 666–686.

(4)   Russell, S. R.; Claridge, S. A. Peptide Interfaces with Graphene: An Emerging Intersection of Analytical Chemistry, Theory, and Materials. *Anal. Bioanal. Chem.* **2016**, *408* (11), 2649–2658.

(5)   Cyr, D. M.; Venkataraman, B.; Flynn, G. W. STM Investigations of Organic Molecules Physisorbed at the Liquid-Solid Interface. *Chem. Mater.* **1996**, *8* (8), 1600–1615.

(6)   Grim, P. C. M.; De Feyter, S.; Gesquiere, A.; Vanoppen, P.; Rucker, M.; Valiyaveettil, S.; Moessner, G.; Mullen, K.; De Schryver, F. C. Submolecularly Resolved Polymerization of Diacetylene Molecules on the Graphite Surface Observed with Scanning Tunneling Microscopy. *Angew. Chemie-International Ed.* **1997**, *36* (23), 2601–2603.

(7)   Okawa, Y.; Aono, M. Linear Chain Polymerization Initiated by a Scanning Tunneling Microscope Tip at Designated Positions. *J. Chem. Phys.* **2001**, *115* (5), 2317–2322.

(8)   Brockman, H. Dipole Potential Of Lipid-Membranes. *Chem. Phys. Lipids* **1994**, *73* (1–2), 57–79.

(9)   Luckey, M. *Membrane Structural Biology: With Biochemical and Biophysical Foundations, Second Edition*; Membrane Structural Biology: with Biochemical and Biophysical Foundations, Second Edition; 2014.

(10)   Seelig, J.; Macdonald, P. M.; Scherer, P. G. Phospholipid Head Groups as Sensors of Electric Charge in Membranes. *Biochemistry* **1987**, *26* (24), 7535–7541.

(11)   Boles, M. A.; Engel, M.; Talapin, D. V. Self-Assembly of Colloidal Nanocrystals: From Intricate Structures to Functional Materials. *Chem. Rev.* **2016**, *116* (18), 11220–11289.

(12)   Rao, C. N. R.; Nag, A. Inorganic Analogues of Graphene. *Eur. J. Inorg. Chem.* **2010**, 4244–4250.

(13)   Davis, T. C.; Russell, S. R.; Claridge, S. A. Edge-on Adsorption of Multi-Chain Functional Alkanes Stabilizes Noncovalent Monolayers on MoS2. *Chem. Commun.* **2018**, No. 54, 11709–11712.

(14) Fernandez, I.; Khiar, N. Recent Developments in the Synthesis and Utilization of Chiral Sulfoxides. *Chem. Rev.* **2003**, *103* (9), 3651–3705.

(15) Babich, I. V; Moulijn, J. A. Science and Technology of Novel Processes for Deep Desulfurization of Oil Refinery Streams: A Review. *Fuel* **2003**, *82* (6), 607–631.

(16) Yang, Y. C. Chemical Detoxification of Nerve Agent VX. *Acc. Chem. Res.* **1999**, *32* (2),

(17) Wagner, G. W.; Yang, Y. C. Rapid Nucleophilic/Oxidative Decontamination of Chemical Warfare Agents. *Ind. Eng. Chem. Res.* **2002**, *41* (8), 1925–1928.

(18) Kim, K.; Tsay, O. G.; Atwood, D. A.; Churchill, D. G. Destruction and Detection of Chemical Warfare Agents. *Chem. Rev.* **2011**, *111* (9), 5345–5403.

(19) Wang, S.-S.; Yang, G.-Y. Recent Advances in Polyoxometalate-Catalyzed Reactions. *Chem. Rev.* **2015**, *115* (11), 4893–4962.

(20) Kozhevnikov, I. V. Catalysis by Heteropoly Acids and Multicomponent Polyoxometalates in Liquid-Phase Reactions. *Chem. Rev.* **1998**, *98* (1), 171–198.

(21) Hill, C. L.; Prossermccartha, C. M. Homogeneous Catalysis By Transition-Metal Oxygen Anion Clusters. *Coord. Chem. Rev.* **1995**, *143*, 407–455.

(22) Cotton, F. A.; Wilkinson, G. *Advanced Inorganic Chemistry*; Wiley, 1988.

(23) Li, L.; Kopf, M. H.; Svetlana, G. V.; Friedrich, R.; Chi, L. Structure Formation by Dynamic Self-Assembly. *Small* **2012**, *8* (4), 488–503.

(24) Paivanranta, B.; Langner, A.; Kirk, E.; David, C.; Ekinci, Y. Sub-10 Nm Patterning Using EUV Interference Lithography. *Nantechnology* **2011**, *22*, 375302.

(25) Gates, B. D.; Xu, Q.; Stewart, M.; Ryan, D.; Wilson, G. C.; Whitesides, G. M. New Appoarches to Nanofabrication: Molding, Printing, and Other Techniques. *Chem. Rev.* **2005**, *105* (4), 1171–1196.

(26) Ito, T.; Okazaki, S. Pushing the Limits of Lithography. *Nature* **2000**, *406*, 1027–1031.

(27) Geissler, M.; Xia, Y. N. Patterning: Principles and Some New Developments. *Adv. Mater.* **2004**, *16* (15), 1249–1269.

(28) Lee, A. Y.; Ulman, A.; Myerson, A. S. Crystallization of Amino Acids on Self-Assembled Monolayers of Rigid Thiols on Gold. *Langmuir* **2002**, *18* (15), 5886–5898.

(29) Singh, A.; Lee, I. S.; Kin, K.; Myerson, A. S. Crystal Growth on Self-Assembled Monolayers. *CrystEngComm* **2011**, *13* (1), 24–32.

(30) Giancarlo, L. C.; Flynn, G. W. Scanning Tunneling and Atomic Force Microscopy Probes of Self-Assembled, Physisorbed Monolayers: Peeking at the Peaks. *Annu. Rev. Phys. Chem.* **1998**, *49*, 297–+.

(31)   Wei, Y.; Kannappan, K.; Flynn, G. W.; Zimmt, M. B. Scanning Tunneling Microscopy of Prochiral Anthracene Derivatives on Graphite: Chain Length Effects on Monolayer Morphology. *J. Am. Chem. Soc.* **2004**, *126* (16), 5318–5322.

(32)   Blodgett, K. B. Monomolecular Films of Fatty Acids on Glass. *J. Am. Chem. Soc.* **1934**, *56*, 495.

(33)   Langmuir, I.; Schaefer, V. J. Activities of Urease and Pepsin Monolayers. *J. Am. Chem. Soc.* **1938**, *60*, 1351–1360.

(34)   Choong, S. W.; Russell, S. R.; Bang, J. J.; Patterson, J. K.; Claridge, S. A. Sitting Phase Monolayers of Polymerizable Phospholipids Create Dimensional, Molecular-Scale Wetting Control for Scalable Solution Based Patterning of Layered Materials. *ACS Appl. Mater. Interfaces* **2017**, *9* (22), 19326–19334.

(35)   Villarreal, T. A.; Russell, S. R.; Bang, J. J.; Patterson, J. K.; Claridge, S. A. Modulating Wettability of Layered Materials by Controlling Ligand Polar Headgroup Dynamics. *J. Am. Chem. Soc.* **2017**, *139* (34), 11973–11979.

(36)   Dubrovin, E. .; Speller, S.; Yaminsky, I. V. Statistical Analysis of Molecular Nanotemplate Driven DNA Adsorption on Graphite. *Langmuir* **2014**, *30* (51), 15423–15432.

(37)   Rabe, J. P.; Buchholz, S. Commensurability And Mobility In 2-Dimensional Molecular-Patterns On Graphite. *Science (80-.).* **1991**, *253* (5018), 424–427.

(38)   Severin, N.; Zhuang, W.; Ecker, C.; Kalachev, A. A.; Sokolov, I. M.; Rabe, J. P. Blowing DNA Bubbles. *Nano Lett.* **2006**, *6* (11), 2561–2566.

(39)   Dubrovin, E. V.; Gerritsen, J. W.; Zivkovic, J.; Yaminsky, I. V.; Speller, S. The Effect of Underlying Octadecylamine Monolayer on the DNA Conformation on the Graphite Surface. *Colloids Surfaces, B Biointerfaces* **2010**, *76* (1), 63–69.

(40)   Lei, S.-B.; Wang, C.; Yin, S.-X.; Wan, L.-J.; Bai, C.-L. Assembling Nanometer Nickel Partickes into Ordered Arrays. *Chem Phys Chem* **2003**, No. 4, 1114–1117.

(41)   Claridge, S. A. Standing, Lying, and Sitting: Translating Building Principles of the Cell Membrane to Synthetic 2D Material Interfaces. *Chem. Commun.* **2018**, *54* (50), 6681–6691.

(42)   Mali, K. S.; Pearce, N.; De Feyter, S.; Champness, N. R. Frontiers of Supramolecular Chemistry at Solid Surfaces. *Chem. Soc. Rev.* **2017**, *46* (9), 2520–2542.

(43)   Bang, J. J.; Russell, S. R.; Rupp, K. K.; Claridge, S. A. Multimodal Scanning Probe Imaging: Nanoscale Chemical Analysis from Biology to Renewable Energy. *Anal. Methods* **2015**, *7* (17), 7106–7127.

(44) Hayes, T. R.; Bang, J. J.; Davis, T. C.; Peterson, C. F.; McMillan, D. G.; Claridge, S. A. Multimicrometer Noncovalent Monolayer Domains on Layered Materials through Thermally Controlled Langmuir-Schaefer Conversion for Noncovalent 2D Functionalization. *ACS Appl. Mater. Interfaces* **2017**, *9* (41), 36409–36416.

(45) Bnag, J. J.; Rupp, K. K.; Russell, S. R.; Choong, S. W.; Claridge, S. A. Sitting Phases of Polymerizable Amphiphiles for Controlled Functionalization of Layered Materials. *J. Am. Chem. Soc.* **2016**, *138* (13), 4448–4457.

(46) Bang, J. J.; Rupp, K. K.; Russell, S. R.; Choong, S. W.; Claridge, S. A.; Davis, T. C.; Bang, J. J.; Brooks, J. T.; McMillan, D. G.; Claridge, S. A.; et al. Molecular Doping of MoS2 Transistors by Self-Assembled Oleylamine Networks. *Langmuir* **2007**, *46* (4), 173–175.

(47) Okawa, Y.; Akai-Kasaya, M.; Kuwahara, Y.; Mandal, S. K.; Aono, M. Controlled Chain Polymerisation and Chemical Soldering for Single-Molecule Electronics. *Nanoscale* **2012**, *4* (10), 3013–3028.

(48) Verveniotis, E.; Okawa, Y.; Makarova, M. V.; Koide, Y.; Liu, J.-W.; Smd, B.; Watanabe, K.; Taniguchi, T.; Komats, K.; Minari, T.; et al. Self-Assembling Diacetylene Molecules on Atomically Flat Insulators. *Phys. Chem. Chem. Phys.* **2016**, *46* (18), 31600–31605.

(49) Tieke, B.; Wegner, G.; Naegele, D.; Ringsdorf, H. Polymerization of Tricosa-10,12-Diynoic Acid in Multilayers. *Angew. Chemie-International Ed. English* **1976**, *15* (12), 764–765.

(50) Tieke, B.; Graf, H. J.; Wegner, G.; Naegele, B.; Ringsdorf, H.; Banerjie, A.; Day, D.; Lando, J. B. Polymerization Of Monolayer And Multilayer Forming Diacetylenes. *Colloid Polym. Sci.* **1977**, *255* (6), 521–531.

(51) Bader, H.; Dorn, K.; Hupfer, B.; Ringsdorf, H. Polymeric Monolayers and Liposomes as Models for Biomembranes - How to Bridge the Gap between Polymer Science and Membrane Biology. *Adv. Polym. Sci.* **1985**, *64*, 1–62.

(52) Laibinis, P. E.; Whitesides, G. M.; Allara, D. L.; Tao, Y. T.; Parikh, A. N.; Nuzzo, R. G. Comparison Of The Structures And Wetting Properties Of Self-Assembled Monolayers Of Normal-Alkanethiols On The Coinage Metal-Surfaces, Cu, Ag, Au. *J. Am. Chem. Soc.* **1991**, *113* (19), 7152–7167.

(53) Lee, T. R.; Carey, R. I.; Biebuyck, H. A.; Whitesides, G. M. The Wetting Of Monolayer Films Exposing Ionizable Acids And Bases. *Langmuir* **1994**, *10* (3), 741–749.

(54) Fears, K. P.; Creager, S. E.; Latour, R. A. Determination of the Surface PK of Carboxylic- and Amine-Terminated Alkanethiols Using Surface Plasmon Resonance Spectroscopy. *Langmuir* **2008**, *24* (3), 837–843.

(55) Wang, B.; Zhang, L. F.; Bae, S. C.; Granick, S. Nanoparticle-Induced Surface Reconstruction of Phospholipid Membranes. *Proc. Natl. Acad. Sci. U. S. A.* **2008**, *105* (47), 18171–18175.

(56) Murray, C. B.; Norris, D. J.; Bawendi, M. G. Synthesis and Characterization of Nearly Monodisperse CdE (E = Sulfur, Selenium, Tellurium) Semiconductor Nanocrystallites. *J. Am. Chem. Soc.* **1993**, *115* (19), 8706–8715.

(57) Huo, Z. Y.; Tsung, C. K.; Huang, W. Y.; Zhang, X. F.; Yang, P. D. Sub-Two Nanometer Single Crystal Au Nanowires. *Nano Lett.* **2008**, *8* (7), 2041–2044.

(58) Bachman, R. E.; Fioritto, M. S.; Fetics, S. K.; Cocker, T. M. The Structural and Functional Equivalence of Aurophilic and Hydrogen Bonding: Evidence for the First Examples of Rotator Phases Induced by Aurophilic Bonding. *J. Am. Chem. Soc.* **2001**, *123* (22), 5376–5377.

(59) Feng, H.; Yang, Y.; You, Y.; Li, G.; Guo, J.; Yu, T.; Shen, Z.; Wu, T.; Xing, B. Simple and Rapid Synthesis of Ultrathin Gold Nanowires, Their Self-Assembly and Application in Surface-Enhanced Raman Scattering. *Chem. Commun.* **2009**, No. 15, 1984–1986.

(60) Kisner, A.; Heggen, M.; Mayer, D.; Simon, U.; Offenhaeusser, A.; Mourzina, Y. Probing the Effect of Surface Chemistry on the Electrical Properties of Ultrathin Gold Nanowire Sensors. *Nanoscale* **2014**, *6* (10), 5146–5155.

(61) Maurer, J. H. M.; Gonzalez-Garcia, L.; Reiser, B.; Kanelidis, I.; Kraus, T. Templated Self-Assembly of Ultrathin Gold Nanowires by Nanoimprinting for Transparent Flexible Electronics. *Nano Lett.* **2016**, *16* (5), 2921–2925.

(62) Gong, S.; Zhao, Y.; Yap, L. W.; Shi, Q.; Wang, Y.; Bay, J. A. P. B.; Lai, D. T. H.; Uddin, H.; Cheng, W. Fabrication of Highly Transparent and Flexible NanoMesh Electrode via Self-Assembly of Ultrathin Gold Nanowires. *Adv. Electron. Mater.* **2016**, *2* (7).

(63) Wang, C.; Hu, Y. J.; Lieber, C. M.; Sun, S. H. Ultrathin Au Nanowires and Their Transport Properties. *J. Am. Chem. Soc.* **2008**, *130* (28), 8902.

(64) Halder, A.; Ravishankar, N. Ultrafine Single-Crystalline Gold Nanowire Arrays by Oriented Attachment. *Adv. Mater.* **2007**, *19* (14), 1854–+.

(65) Loubat, A.; Imperor-Clerc, M.; Pansu, B.; Meneau, F.; Raquet, B.; Viau, G.; Lacroix, L. M. Growth and Self-Assembly of Ultrathin Au Nanowires into Expanded Hexagonal Super Lattice Studied by in Situ SAXS. *Langmuir* **2014**, *30* (14), 4005–4012.

(66) Ulman, A. Formation and Structure of Self-Assembled Monolayers. *Chem. Rev.* **1996**, *96* (4), 1533–1554.

(67)   Templeton, A. C.; Wuelfing, W. P.; Murray, R. W. Monolayer Protected Cluster Molecules. *Acc. Chem. Res.* **2000**, *33* (1), 27–36.

(68)   Love, J. C.; Estroff, L. A.; Kriebel, J. K.; Nuzzo, R. G.; Whitesides, G. M. Self-Assembled Monolayers of Thiolates on Metals as a Form of Nanotechnology. *Chem. Rev.* **2005**, *105* (4), 1103–1170.

(69)   Reiser, B.; Gerstner, D.; Gonzalez-Garcia, L.; Maurer, J. H. M.; Kanelidis, I.; Kraus, T. Multivalent Bonds in Self-Assembled Bundles of Ultrathin Gold Nanowires. *Phys. Chem. Chem. Phys.* **2016**, *18* (39), 27165–27169.

(70)   Groszek, A. J. Preferential Adsorption of Normal Hydrocarbons on Cast Iron. *Nature* **1962**, *196* (4854), 531-.

(71)   de la Rosa, C. J. L.; Phillipson, R.; Teyssandier, J.; Adisoejoso, J.; Balaji, Y.; Huyghebaert, C.; Radu, I.; Heyns, M.; De Feyter, S.; De Gendt, S. Molecular Doping of MoS2 Transistors by Self-Assembled Oleylamine Networks. *Appl. Phys. Lett.* **2016**, *109* (25).

(72)   Groszek, A. J. Preferential Adsorption Of Long-Chain Normal Paraffins On Mos2 Ws2 + Graphite From N-Heptane. *Nature* **1964**, *204* (495), 680-.

(73)   Grzelczak, M.; Perez-Juste, J.; Mulvaney, P.; Liz-Marzan, L. M. Shape Control in Gold Nanoparticle Synthesis. *Chem. Soc. Rev.* **2008**, *37* (9), 1783–1791.

(74)   Iritani, K.; Tahara, K.; De Feyter, S.; Tobe, Y. Host-Guest Chemistry in Integrated Porous Space Formed by Molecular Self-Assembly at Liquid-Solid Interfaces. *Langmuir* **2017**, *33* (19), 4601–4618.

(75)   Tahara, K.; Katayama, K.; Blunt, M. O.; Iritani, K.; De Feyter, S.; Tobe, Y. Functionalized Surface-Confined Pores: Guest Binding Directed by Lateral Noncovalent Interactions at the Solid-Liquid Interface. *ACS Nano* **2014**, *8* (8), 8683–8694.

(76)   Mezour, M. A.; Perepichka, I. I.; Zhu, J.; Lennox, R. B.; Perepichka, D. F. Directing the Assembly of Gold Nanoparticles with Two-Dimensional Molecular Networks. *ACS Nano* **2014**, *8* (3), 2214–2222.

(77)   Claridge, S. A.; Castleman A. W., J.; Khanna, S. N.; Murray, C. B.; Sen, A.; Weiss, P. S. Cluster-Assembled Materials. *ACS Nano* **2009**, *3* (2), 244–255.

(78)   Zhai, T.; Li, L.; Wang, X.; Fang, X. S.; Bando, Y.; Golberg, D. Recent Developments in One-Dimensional Inorganic Nanostructures for Photodetectors. *Adv. Funct. Mater.* **2010**, *20* (24), 4233–4248.

(79)   Burrows, N. D.; Vartanian, A. M.; Abadeer, N. S.; Grzincic, E. M.; Jacob, L. M.; Lin, W. N.; Li, J.; Dennison, J. M.; Hinman, J. G.; Murphy, C. J. Anisotropic Nanoparticles and Anisotropic Surface Chemistry. *J. Phys. Chem. Lett.* **2016**, *7* (4), 632–641.

(80) Reiser, B.; Gerstner, D.; Gonzalez-Garcia, L.; Maurer, J. H. M.; Kanelidis, I.; Kraus, T. Spinning Hierarchical Gold Nanowire Microfibers by Shear Alignment and Intermolecular Self-Assembly. *ACS Nano* **2017**, *11* (5), 4934–4942.

(81) Glor, E. C.; Ferrier, R. C.; Li, C.; Composto, R. J.; Fakhraai, Z. Out-of-Plane Orientation Alignment and Reorientation Dynamics of Gold Nanorods in Polymer Nanocomposite Films. *Soft Matter* **2017**, *13* (11), 2207–2215.

(82) Hoeppener, S.; Chi, L. F.; Fuchs, H. Formation of Au-55 Strands on a Molecular Template at the Solid-Liquid Interface. *Nano Lett.* **2002**, *2* (5), 459–463.

(83) Geng, Y. F.; Liu, M. Q.; Xue, J. D.; Xu, P.; Wang, Y. F.; Shu, L. J.; Zeng, Q. D.; Wang, C. A Template-Confined Fabrication of Controllable Gold Nanoparticles Based on the Two-Dimensional Nanostructure of Macrocycles. *Chem. Commun.* **2015**, *51* (31), 6820–6823.

(84) Cui, D.; MacLeod, J. M.; Ebrahimi, M.; Perepichka, D. F.; Rosei, F. Solution and Air Stable Host/Guest Architectures from a Single Layer Covalent Organic Framework. *Chem. Commun.* **2015**, *51* (92), 16510–16513.

(85) Mann, J. A.; Rodriguez-Lopez, J.; Abruna, H. D.; Dichtel, W. R. Multivalent Binding Motifs for the Noncovalent Functionalization of Graphene. *J. Am. Chem. Soc.* **2011**, *133* (44), 17614–17617.

(86) De Feyter, S.; De Schryver, F. C. Two-Dimensional Supramolecular Self-Assembly Probed by Scanning Tunneling Microscopy. *Chem. Soc. Rev.* **2003**, *32* (3), 139–150.

(87) Giridharagopal, R.; Kelly, K. F. Substrate-Dependent Properties of Polydiacetylene Nanowires on Graphite and MoS2. *ACS Nano* **2008**, *2* (8), 1571–1580.

(88) Bang, J. J.; Porter, A. G.; Davis, T. C.; Hayes, T. R.; Claridge, S. A. Spatially Controlled Noncovalent Functionalization of 2D Materials Based on Molecular Architecture. *Langmuir* **2018**, *34* (19), 5454–5463.

(89) Jiang, H.; Jelinek, R. Dramatic Shape Modulation of Surfactant/Diacetylene Microstructures at the Air-Water Interface. *Chem. Eur. J.* **2014**, *20* (50), 16747–16752.

(90) Yang, Y.; Zimmt, M. B. Shape-Directed Patterning and Surface Reaction of Tetra-Diacetylene Monolayers: Formation of Linear and Two-Dimensional Grid Polydiacetylene Alternating Copolymers. *Langmuir* **2015**, *31* (45), 12408–12416.

(91) Akai-Kasaya, M.; Shimizu, K.; Watanabe, Y.; Saito, A.; Aono, M.; Kuwahara, Y. Electronic Structure of a Polydiacetylene Nanowire Fabricated on Highly Ordered Pyrolytic Graphite. *Phys. Rev. Lett.* **2003**, *91* (25).

(92) Li, B.; Tahara, K.; Adisoejoso, J.; Vanderlinden, W.; Mali, K. S.; De Gendt, S.; Tobe, Y.; De Feyter, S. Self-Assembled Air-Stable Supramolecular Porous Networks on Graphene. *ACS Nano* **2013**, *7* (12), 10764–10772.

(93) Davis, T. C.; Bang, J. J.; Brooks, J. T.; McMillan, D. G.; Claridge, S. A. Hierarchically Patterned Noncovalent Functionalization of 2D Materials by Controlled Langmuir-Schaefer Conversion. *Langmuir* **2018**, *34* (4), 1353–1362.

(94) Miura, A.; De Feyter, S.; Abdel-Mottaleb, M. M. S.; Gesquiere, A.; Grim, P. C. M.; Moessner, G.; Sieffert, M.; Klapper, M.; Mullen, K.; De Schryver, F. C. Light- and STM-Tip-Induced Formation of One-Dimensional and Two-Dimensional Organic Nanostructures. *Langmuir* **2003**, *19* (16), 6474–6482.

(95) Venkatesh, R.; Kundu, S.; Pradhan, A.; Sai, T. P.; Ghosh, A.; Ravishankar, N. Directed Assembly of Ultrathin Gold Nanowires over Large Area by Dielectrophoresis. *Langmuir* **2015**, *31* (33), 9246–9252.

(96) Rand, R. P.; Tinker, D. O.; Fast, P. G. Polymorphism of Phosphatidylethanolamines from Two Natural Sources. *Chem. Phys. Lipids.* **1971**, *6*, 333–342.

(97) Jendrasiak, G. L.; Mendible, J. C. The Effect of the Phase Transition on the Hydration and Electrical Conductivity of Phospholipids. *Biochim. Biophys. Act* **1976**, *424*, 133–148.

(98) Hsu, M. F.; Dufresne, E. R.; Weitz, D. . Reverse Micelles Enable Strong Electrostatic Interactions between Colloidal Particles in Nonpolar Solvents. *Langmuir* **2005**, *21*, 4881–4887.

(99) Muskens, O. L.; Bachelier, G.; Del Fatti, N.; Vallee, F.; Brioude, A.; Jiang, X. C.; Pileni, M. P. Quantitative Absorption Spectroscopy of a Single Gold Nanorod. *J. Phys. Chem. C* **2008**, *112* (24), 8917–8921.

(100) Wang, S.; Yu, L. P.; Li, P.; Meng, L.; Wang, L. Copper(I) Iodide Catalyzed Cross-Coupling Reaction of Terminal Alkynes with 1-Bromoalkynes: A Simple Synthesis of Unsymmetrical Buta-1,3-Diynes. *Synthesis (Stuttg).* **2011**, *10*, 1541–1546.

(101) Perttu, E. K.; Kohli, A. G.; Soka Jr., F. . Inverse-Phosphocholine Lipids: A Remix of Common Phospholipid. *J. Am. Chem. Soc.* **2012**, *134* (4485–4488).

(102) Steger, C. An Unbiased Detector of Curvilinear Structures. *IEEE Trans. Pattern Anal. Mach. Intell.* **1998**, *20*, 113–125.

(103) Das, S.; Gulotty, R.; Sumant, A. V; Roelofs, A. All Two-Dimensional, Flexible, Transparent, and Thinnest Thin Film Transistor. *Nano Lett.* **2014**, *14* (5), 2861–2866.

(104) Lee, G.-H.; Yu, Y.-J.; Cui, X.; Petrone, N.; Lee, C.-H.; Choi, M. S.; Lee, D.-Y.; Lee, C.; Yoo, W. J.; Watanabe, K.; et al. Flexible and Transparent MoS2 Field-Effect Transistors on Hexagonal Boron Nitride-Graphene Heterostructures. *ACS Nano* **2013**, *7* (9), 7931–7936.

(105) Chang, H.-Y.; Yang, S.; Lee, J.; Tao, L.; Hwang, W.-S.; Jena, D.; Lu, N.; Akinwande, D. High-Performance, Highly Bendable MoS2 Transistors with High-K Dielectrics for Flexible Low-Power Systems. *ACS Nano* **2013**, *7* (6), 5446–5452.

(106) Wang, Q.; Xu, K.; Wang, Z.; Wang, F.; Huang, Y.; Safdar, M.; Zhan, X.; Wang, F.; Cheng, Z.; He, J. Van Der Waals Epitaxial Ultrathin Two-Dimensional Nonlayered Semiconductor for Highly Efficient Flexible Optoelectronic Devices. *Nano Lett.* **2015**, *15* (2), 1183–1189.

(107) Mak, K. F.; Lee, C.; Hone, J.; Shan, J.; Heinz, T. F. Atomically Thin MoS2: A New Direct-Gap Semiconductor. *Phys. Rev. Lett.* **2010**, *105* (13).

(108) Splendiani, A.; Sun, L.; Zhang, Y.; Li, T.; Kim, J.; Chim, C.-Y.; Galli, G.; Wang, F. Emerging Photoluminescence in Monolayer MoS2. *Nano Lett.* **2010**, *10* (4), 1271–1275.

(109) Radisavljevic, B.; Radenovic, A.; Brivio, J.; Giacometti, V.; Kis, A. Single-Layer MoS2 Transistors. *Nat. Nanotechnol.* **2011**, *6* (3), 147–150.

(110) Kim, S.; Konar, A.; Hwang, W.-S.; Lee, J. H.; Lee, J.; Yang, J.; Jung, C.; Kim, H.; Yoo, J.-B.; Choi, J.-Y.; et al. High-Mobility and Low-Power Thin-Film Transistors Based on Multilayer MoS2 Crystals. *Nat. Commun.* **2012**, *3*.

(111) Lee, H. S.; Min, S.-W.; Chang, Y.-G.; Park, M. K.; Nam, T.; Kim, H.; Kim, J. H.; Ryu, S.; Im, S. MoS2 Nanosheet Phototransistors with Thickness-Modulated Optical Energy Gap. *Nano Lett.* **2012**, *12* (7), 3695–3700.

(112) Lopez-Sanchez, O.; Lembke, D.; Kayci, M.; Radenovic, A.; Kis, A. Ultrasensitive Photodetectors Based on Monolayer MoS2. *Nat. Nanotechnol.* **2013**, *8* (7), 497–501.

(113) Choi, W.; Cho, M. Y.; Konar, A.; Lee, J. H.; Cha, G.-B.; Hong, S. C.; Kim, S.; Kim, J.; Jena, D.; Joo, J.; et al. High-Detectivity Multilayer MoS2 Phototransistors with Spectral Response from Ultraviolet to Infrared. *Adv. Mater.* **2012**, *24* (43), 5832–5836.

(114) Kang, D.-H.; Kin, M.-S.; Shim, J.; Jeon, J.; Park, H.-Y.; Jung, W.-S.; Yu, H.-Y.; Pang, C.-H.; Lee, S.; Park, J.-H. High-Performance Transition Metal Dichalcogenide Photodetectors Enhanced by Self-Assembled Monolayer Doping. *Adv. Funct. Mater.* **2015**, *25*, 4209–4227.

(115) Kiriya, D.; Zhou, Y.; Nelson, C.; Hettick, M.; Madhvapathy, S. R.; Chen, K.; Zhao, P.; Tosun, M.; Minor, A. M.; Chrzan, D. C.; et al. Oriented Growth of Gold Nanowires on MoS2. *Adv. Funct. Mater.* **2015**, No. 25, 6257–6264.

(116) Li, Z.; Wang, Y.; Kozbial, A.; Shenoy, G.; Zhou, F.; McGinley, R.; Ireland, P.; Morganstein, B.; Kunkel, A.; Surwade, S. P.; et al. Effect of Airborne Contaminants on the Wettability of Supported Graphene and Graphite. *Nat. Mater.* **2013**, *12* (10), 925–931.

(117) Kozbial, A.; Gong, X.; Liu, H.; Li, L. UnderStanding the Intrinsic Water Wettability of Molybdenum Disulfide (MoS2). *Langmuir* **2015**, *31*, 8429–8435.

(118) Sheldon, R. A.; Arends, I.; Handfeld, U. *Green Chemistry and Catalysis*; Wiley-VCH: Weinheim, 2007.

(119) Romao, C. C.; Kuhn, F. E.; Herrmann, W. A. Rhenium(VII) Oxo and Imido Complexes: Synthesis, Structures, and Applications. *Chem. Rev.* **1997**, *97* (8), 3197–3246.

(120) Livingston, S. R.; Landry, C. C. Oxidation of a Mustard Gas Analogue Using an Aldehyde/O-2 System Catalyzed by V-Doped Mesoporous Silica. *J. Am. Chem. Soc.* **2008**, *130* (40), 13214–13215.

(121) Livingston, S. R.; Kumar, D.; Landry, C. C. Oxidation of 2-Chloroethyl Ethyl Sulfide Using V-APMS. *J. Mol. Catal. a-Chemical* **2008**, *283* (1–2), 52–59.

(122) Ringenbach, C. R.; Livingston, S. R.; Kumar, D.; Landry, C. C. Vanadium-Doped Acid-Prepared Mesoporous Silica: Synthesis, Characterization, and Catalytic Studies on the Oxidation of a Mustard Gas Analogue. *Chem. Mater.* **2005**, *17* (22), 5580–5586.

(123) Zhang, B.; Li, S.; Poethig, A.; Cokoja, M.; Zang, S.-L.; Herrmann, W. A.; Kuehn, F. E. Oxidation Reactions Catalyzed by Polyoxomolybdate Salts. *Zeitschrift Fur Naturforsch. Sect. B-a J. Chem. Sci.* **2013**, *68* (5–6), 587–597.

(124) Buru, C. T.; Li, P.; Mehdi, B. L.; Dohnalkoya, A.; Platero-Prats, A. E.; Browning, N. D.; Chapman, K. W.; Hupp, J. T.; Farha, O. K. Adsorption of a Catalytically Accessible Polyoxometalate in a Mesoporous Channel-Type Metal-Organic Framework. *Chem. Mater.* **2017**, *29* (12), 5174–5181.

(125) Cantwell, K. E.; Fanwick, P. E.; Abu-Omar, M. M. Mild, Selective Sulfoxidation with Molybdenum(VI) Cis-Dioxo Catalysts. *Acs Omega* **2017**, *2* (5), 1778–1785.

(126) Phan, T. D.; Kinch, M. A.; Barker, J. E.; Ren, T. Highly Efficient Utilization of H2O2 for Oxygenation of Organic Sulfides Catalyzed by Gamma-SiW10O34(H2O)2 (4-). *Tetrahedron Lett.* **2005**, *46* (3), 397–400.

(127) Thompson, D. J.; Zhang, Y.; Ren, T. Polyoxometalate Gamma-SiW10O34(H2O)(2) (4-) on MCM-41 as Catalysts for Sulfide Oxygenation with Hydrogen Peroxide. *J. Mol. Catal. a-Chemical* **2014**, *392*, 188–193.

(128) Thompson, D. J.; Cao, Z.; Judkins, E. C.; Fanwick, P. E.; Ren, T. Peroxo-Dimolybdate Catalyst for the Oxygenation of Organic Sulfides by Hydrogen Peroxide. *Inorganica Chim. Acta* **2015**, *437*, 103–109.

(129) Trost, B. M.; Masuyama, Y. Molybdenum Catalyzed-Reactions Selectivity In Oxidations With Hydrogen-Peroxide And Ammonium Molybdate. *Isr. J. Chem.* **1984**, *24* (2), 134–143.

(130) Lu, H.; Deng, C.; Ren, W.; Yang, X. Oxidative Desulfurization of Model Diesel Using (C4H9)(4)N (6)Mo7O24 as a Catalyst in Ionic Liquids. *Fuel Process. Technol.* **2014**, *119*, 87–91.

(131) Absillis, G.; Cartuyvels, E.; Van Deun, R.; Parac-Vogt, T. N. Hydrolytic Cleavage of an RNA-Model Phosphodiester Catalyzed by a Highly Negatively Charged Polyoxomolybdate Mo7O24 (6-) Cluster. *J. Am. Chem. Soc.* **2008**, *130* (51), 17400–17408.

(132) Trost, B. M.; Masuyama, Y. Chemoselectivity in Molybdenum Catalyzed Alcohol and Aldehyde Oxidations. *Tetrahedron Lett.* **1984**, *25* (2), 173–176.

(133) Sergienko, V. S. Structural Chemistry of Peroxo Compounds of Group VI Transition Metals: II. Peroxo Complexes of Molybdenum and Tungsten: A Review. *Crystallogr. Reports* **2008**, *53* (1), 18–46.

(134) Carreno, M. C. Applications of Sulfoxides to Asymmetric-Synthesis of Biologically-Active Compounds. *Chem. Rev.* **1995**, *95* (6), 1717–1760.

(135) Yang, Y. C. Chemical Detoxification of Nerve Agent VX. *Acc. Chem. Res.* **1998**, No. 32, 109–115.

(136) Kamata, K.; Hirano, T.; Ishimoto, R.; Mizuno, N. Sulfoxidation with Hydrogen Peroxide Catalyzed by SeO4{WO(O-2)(2)}(2) (2-). *Dalt. Trans.* **2010**, *39* (23), 5509–5518.

(137) Wilm, M.; Mann, M. Analytical Properties of the Nanoelectrospray Ion Source. *Anal. Chem.* **1996**, *68* (1), 1–8.

(138) Chen, P. Electrospray Ionization Tandem Mass Spectrometry in High-Throughput Screening of Homogeneous Catalysts. *Angew. Chemie-International Ed.* **2003**, *42* (25), 2832–2847.

(139) Walanda, D. K.; Burns, R. C.; Lawrance, G. A.; von Nagy-Felsobuki, E. I. Electrospray Mass Spectral Study of Isopolyoxomolybdates. *J. Chem. Soc. Trans.* **1999**, No. 3, 311–321.

(140) Mimoun, H.; Deroch, I. S.; Sajus, L. New Molybdenum-6 and Tungsten-6 Peroxy-Complexes. *Bull. Soc. Chim. Fr.* **1969**, No. 5, 1481.

(141) Bregeault, J. M.; Vennat, M.; Salles, L.; Piquemal, J. Y.; Mahha, Y.; Briot, E.; Bakala, P. C.; Atlamsani, A.; Thouvenot, R. From Polyoxometalates to Polyoxoperoxometalates and Back Again; Potential Applications. *J. Mol. Catal. a-Chemical* **2006**, *250* (1–2), 177–189.

(142) O'Hair, R. A. J. The 3D Quadrupole Ion Trap Mass Spectrometer as a Complete Chemical Laboratory for Fundamental Gas-Phase Studies of Metal Mediated Chemistry. *Chem. Commun.* **2006**, No. 14, 1469–1481.

(143) O'Hair, R. A. J.; Khairallah, G. N. Gas Phase Ion Chemistry of Transition Metal Clusters: Production, Reactivity, and Catalysis. *J. Clust. Sci.* **2004**, *15* (3), 331–363.

Dalton Transactions

PAPER

Check for updates

Heptamolybdate: a highly active sulfide oxygenation catalyst†‡

Ashlin G. Porter,[a] Hanfeng Hu,[a] Xuemei Liu,[b] Adharsh Raghavan,[a] Sarju Adhikari,[a] Derrick R. Hall,[a] Dylan J. Thompson,[a] Bin Liu,[a] Yu Xia*[a] and Tong Ren ⓘ*[a]

The sulfide oxygenation activities of both heptamolybdate ($[Mo_7O_{24}]^{6-}$, $[\mathbf{1}]^{6-}$) and its peroxo adduct $[Mo_7O_{22}(O_2)_2]^{6-}$ ($[\mathbf{2}]^{6-}$) were examined in this contribution. $[Mo_7O_{22}(O_2)_2]^{6-}$ was prepared in a yield of 65% from $(NH_4)_6[Mo_7O_{24}]$ (**1a**) upon treatment of 10 equiv. of H_2O_2 and structurally identified through single crystal X-ray diffraction study. $(nBu_4N)_6[Mo_7O_{22}(O_2)_2]$ (**2b**) is an efficient catalyst for the sequential oxygenation of methyl phenyl sulfide (MPS) by H_2O_2 to the corresponding sulfoxide and subsequently sulfone with a 100% utility of H_2O_2. Surprisingly, $(nBu_4N)_6[Mo_7O_{24}]$ (**1b**) is a significantly faster catalyst than **2b** for MPS oxygenation under identical conditions. The pseudo-first order k_{cat} constants from initial rate kinetics are 54 M^{-1} s^{-1} and 19 M^{-1} s^{-1} for **1b** and **2b**, respectively. Electrospray ionization mass spectrometry (ESI-MS) investigation of **1b** under the catalytic reaction conditions revealed that $[Mo_2O_{11}]^{2-}$ is likely the main active species in sulfide oxygenation by H_2O_2.

Introduction

The oxygenation of organic sulfides is a transformation key to medicinal chemistry,[1] petroleum desulfurization,[2] and nerve agent detoxification.[3–5] Highly relevant to the latter two applications are both the reaction rates and the use of inexpensive oxidants and catalysts. Hydrogen peroxide and *tert*-butyl hydroperoxide (TBHP) are among the desired oxidants because of their low costs and environmentally friendly nature.[6] Hydrogen peroxide is the most studied oxidant, and can be activated with a variety of transition metal based homogeneous catalysts. Among a plethora of catalysts reported,[7] homo- and hetero-polyoxometalates (POMs) stand out due to both the ease of preparation and their chemical robustness.[8–10] Recent examples of sulfide oxygenation catalyzed by both POMs and related species include the degradation of mustard agent simulants,[11–13] oxygenation of thioanisole with $(Bmim)_2[Mo_6O_{19}]$ (Bmim = 1-butyl-3-methylimidazolium),[14] conversion of 2-chloroethyl ethyl sulfide to its sulfoxide using $H_3PW_{12}O_{40}$ embedded in a MOF,[15] and the selective formation of sulfoxide as the precursor of vinyl glycine.[16] Contributions from our laboratory include the early demonstration of excellent chemical selecti-

vity and efficient use of H_2O_2 in sulfide oxygenation using $[\gamma\text{-}SiW_{10}O_{34}(H_2O)_2]^{4-}$,[17] its subsequent heterogenization in amine functionalized MCM-41,[18] and the recent discovery of peroxo-dimolybdate as a highly efficient catalyst.[19]

Heptamolybdate, $[Mo_7O_{24}]^{6-}$ (also known as paramolybdate), is the lowest member of the isopolymolybdate family,[20] and its ammonium salt $((NH_4)_6[Mo_7O_{24}]$, **1a**) is commercially available and inexpensive. While heteropolyoxometallates have attracted intense interest as oxygenation catalysts,[9,10] the role of heptamolybdate as an oxygenation catalyst has been sparingly explored. Noteworthy among a handful of examples using $[Mo_7O_{24}]^{6-}$ as a catalyst are the olefin epoxidation and alcohol oxidation by H_2O_2[21] and the conversion of dibenzothiophene and derivatives to corresponding sulfones by H_2O_2 in ionic liquid.[22] Also noteworthy is the ability of heptamolybdate to promote hydrolysis of phosphoesters.[23] Reported herein are the preparation and structural characterization of a di-peroxo derivative of heptamolybdate, $[Mo_7O_{22}(O_2)_2]^{6-}$ (2^{6-}), and its activity in promoting sulfide oxygenation by H_2O_2. It was discovered in the process of performing control experiments that the parent heptamolybdate is a far more active catalyst. The reactivity scope, catalytic rates and the nature of the active species under the catalytic conditions were carefully examined.

[a]Department of Chemistry, Purdue University, 560 Oval Drive, West Lafayette, IN 47906, USA. E-mail: yxia@purdue.edu, tren@purdue.edu

[b]College of Chemistry and Chemical Engineering, Xi'an Shiyou University, Xi'an, China

†Dedicated to Professor Kim Dunbar on the occasion of her 60th Birthday.
‡Electronic supplementary information (ESI) available. CCDC 1839304. For ESI and crystallographic data in CIF or other electronic format see DOI: 10.1039/c8dt00583d

Results and discussion

Synthesis and structural identification of $[Mo_7O_{22}(O_2)_2]^{-}$ (2^{6-})

Curious about the nature of the active species in the aforementioned olefin epoxidation and alcohol oxidation reactions cata-

lyzed by heptamolybdate,[21,24] we first sought to identify the predominant species produced upon treatment of $[Mo_7O_{24}]^{6-}$ with H_2O_2. Hence, an aqueous solution of $(NH_4)_6[Mo_7O_{24}]$ (**1a**) was treated with 10 equiv. of H_2O_2 in the presence of 2.5 equiv. guanidinium $(CH_6N_3^+)$ chloride, and $(NH_4)_4(CH_6N_3)_2[Mo_7O_{22}(O_2)_2]$ (**2a**) was isolated as yellow crystalline materials in a yield of 65% upon slow evaporation of the reaction mixture. X-ray diffraction study verified the above-mentioned formula of **2a** with lattice water molecules. Compared to the parent ion $[Mo_7O_{24}]^{6-}$, one of the terminal oxos on both the Mo3 and Mo5 centers were replaced by a peroxo group in forming the di-peroxo heptamolybdate anion $[Mo_7O_{22}(O_2)_2]^{6-}$, as shown in Fig. 1. Both of the peroxo-bound molybdenum centers (Mo3 and Mo5) are seven-coordinated. The pentagonal bipyramidal arrangement of coordination is frequently observed in peroxo complexes. The bond lengths of the peroxo moiety in **2a** are 1.44(2) and 1.34(2) Å, respectively, falling in the expected range for Mo/W peroxo compounds.[25]

Sulfide oxygenation activity of $[Mo_7O_{22}(O_2)_2]^{6-}$ and $[Mo_7O_{24}]^{6-}$

Upon the structural identification of the di-peroxo species $[2]^{6-}$, its activity in facilitating H_2O_2 oxygenation was examined with methyl phenyl sulfide (MPS, also known as thioanisole) as the substrate. With **2b** $((Bu_4N)_6[Mo_7O_{22}(O_2)_2])$ at 1 mol% loading and the use of two equiv. of H_2O_2, MPS was completely consumed in 10 min as indicated by GC analysis (Table 1), demonstrating the efficacy of $[2]^{6-}$ in promoting H_2O_2 oxygenation. Furthermore, full conversion of MPS to sulfone (MPSO$_2$) was accomplished in 5 h in the same reaction, indicating a 100% utility of active oxygen in H_2O_2. Previously, our laboratory reported that a divacant lacunary silicotungstate, $[\gamma\text{-}SiW_{10}O_{34}(H_2O)_2]^{4-}$, catalyzes H_2O_2 oxygenation of organic sulfides with a 100% utility of H_2O_2.[17] However, the catalytic reaction with divacant silicotungstate is significantly slower than those with **2b** even in the presence of the best co-catalyst,

Fig. 1 Structural plot of $[Mo_7O_{22}(O_2)_2]^{6-}$ in **2a**. Counter ions and lattice water molecules were omitted for clarity; the CIF has been deposited with the Cambridge crystallographic data centre (CCDC 1839304‡).

Table 1 Sulfide oxidation of MPS catalysed by **1b** and **2b**[a]

Time (min)	Catalyst	MPS (%)	MPSO (%)	MPSO₂ (%)
2	1b	1	71	28
	2b	37	60	3
5	1b	0	46	54
	2b	4	81	14
8	1b	0	40	59
	2b	1	79	20
10	1b	0	38	62
	2b	0	69	30
15	1b	0	29	71
	2b	0	56	44
30	1b	0	12	88
	2b	0	34	66
60	1b	0	2	98
	2b	0	16	84
120	1b	0	1	99
	2b	0	2	98
180	1b	0	1	99
	2b	0	1	99
240	1b	0	0	100
	2b	0	1	99
300	1b	0	0	100
	2b	0	0	100

[a] Each reaction was carried out with 0.50 mmol MPS, 1.0 mmol H_2O_2, and 0.0050 mmol **1b**/**2b** (1 mol% loading) in 5 mL CH_3CN at room temperature.

and the preparation of divacant silicotungstate is laborious. Clearly, **2b** is a simple and yet much more efficient catalyst for H_2O_2 oxygenation.

Encouraged by the performance of **2b**, the activity of heptamolybdate was examined in a control experiment. Similar to the conditions used with **2b**, MPS was treated with two equiv. of H_2O_2 in the presence of 1 mol% $(Bu_4N)_6[Mo_7O_{24}]$ (**1b**). Surprisingly, **1b** is significantly faster than **2b**, consuming almost all MPS in 2 min with 100% consumption achieved in under 5 min (Table 1). It is clear from Table 1 that **1b** is also significantly faster than **2b** in converting sulfoxide (MPSO) to sulfone (MPSO$_2$).

The fast oxygenation facilitated by **1b** also prompted further exploration into whether the oxygenation occurs in a stepwise fashion. The reaction was conducted at a reduced level of catalyst loading (0.2 mol% with respect to MPS), and the distribution of products was monitored with GC. The resultant speciation curves are shown in Fig. 2, which indicates the presence of MPSO$_2$ (ca. 20%) at the time of full consumption of MPS around 10 min. Clearly, the oxygenation catalyzed by **1b** is not step-wise. It is also apparent from Fig. 2 that there is no observable induction period.

Catalytic oxygenation of other organic sulfides with $[Mo_7O_{24}]^{6-}$

Oxygenation of organic sulfides is relevant to current technologies such as the preparation of chiral sulfoxides in medicinal chemistry,[26] chemical degradation of V-type nerve agents,[27] and deep desulfurization of fossil fuels.[2] Hence, the proficiency of **1** in facilitating deep oxygenation was tested using a variety of sulfide substrates including DBT (dibenzothio-
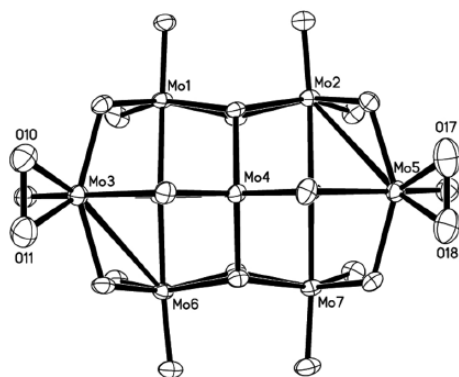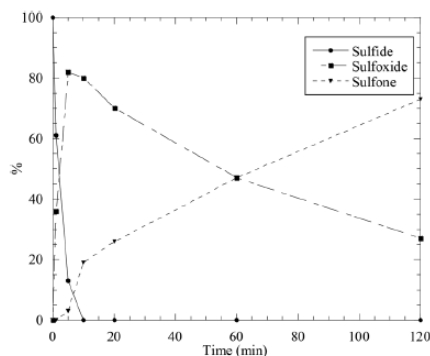
Dalton Transactions

Fig. 2 Speciation curve of H_2O_2-oxygenation of MPS catalyzed by **1b** conducted with 0.50 mmol MPS, 1.0 mmol H_2O_2 and 0.0010 mmol **1b** in 5 mL CH_3CN at room temperature.

phene), and results are collected in Table 2. All entries in Table 2 are equal in catalyst loading (0.1 mol%) and use of two equiv. of H_2O_2 except DBT. It is clear from Table 2 that the fastest conversions to sulfone were accomplished within one hour for PTE (phenyl thioethanol) and BPS (benzyl phenyl sulfide), which are the most electron-rich among the substrates listed. Electron poor 4BT (4-bromothioanisole) and PPS (phenylsulfide) required longer reaction times to fully convert. Plausibly, the faster electrophilic oxygenation of the more electron rich sulfides resulted in a faster formation of sulfone. Being the most sterically hindered substrate DBT required a much longer conversion time and H_2O_2 in 100% excess. DBT and its methyl derivatives, known as refractory sulphides, are the primary targets of fuel desulfurization,[2] and **1** could be a relevant catalyst. In addition, oxygenation of sulphides catalyzed by **2b** were carried out under the same conditions as those for reactions with **1b** and the times required for complete conversion to the corresponding sulphone (Table 2) are

much longer than those with **1b**, consistent with the result of MPS oxygenation.

Initial rate kinetics

Given the extraordinary efficiency of both $[1]^{6-}$ and $[2]^{6-}$ in promoting sulfide oxygenation and a potentially complex reaction mechanism due to their multinuclear nature, the reaction rate dependence on catalyst concentration was investigated based on the initial rate method. While both MPS (1.21 mM) and H_2O_2 (23 mM) were present in large excess in order to maintain pseudo first order conditions, the concentration of **1b** was varied from 0.003 mM to 0.036 mM (0.25 to 3.0 mol% loading with respect to MPS), and that of **2b** from 0.024 mM to 0.12 mM (2.0 to 10 mol% with respect to MPS). Monitoring the disappearance of MPS at 290 nm, the k_{obs} at a specific catalyst concentration was determined by fitting the first 15 min trace using a first order equation ($\ln(Abs)$ versus t), and the resultant k_{obs} vs. [cat] plots are shown in Fig. 3 for both **1b** and **2b**. It is clear from Fig. 3 that fitting both k_{obs} vs. [cat] data sets yielded excellent linear correlations, and the slopes yielded k_{cat} values of 54 M^{-1} s^{-1} and 19 M^{-1} s^{-1} for **1b** and **2b**, respectively. Consistent with the data presented in Table 1, k_{cat}(**1b**) is significantly larger than k_{cat}(**2b**). Previously, k_{cat} for the same H_2O_2 oxygenation of MPS was reported to be about 11 M^{-1} min^{-1} for $[\{MoO(O_2)_2\}_2(\mu\text{-O})]^{2-}$ by our laboratory[19] and 9.3 M^{-1} s^{-1} for $[SeO_4\{\mu\text{-WO}(O_2)_2\}_2]^{2-}$ by Kamata et al.,[28] which were among the fastest oxygenation catalysts based on molybdates/tungstates. Clearly, heptamolybdate offers the advantage of being a superior catalyst without the requirement of elaborate synthesis.

The significant contrast in k_{cat} between $[1]^{6-}$ and $[2]^{6-}$ may signal a difference in the active catalytic species. To gain an insight into the nature of possible active species, UV-vis spectra of **1b** and **2b** as pure compounds and in the presence of H_2O_2 in large excess were examined, and the results are

Table 2 Oxygenation of additional sulfides with **1b** and **2b**[a]

Sulfide	Abbreviation	H_2O_2 equiv.	$1b^b$ t/h	$2b^b$ t/h
	PTE	2	1	2
	BPS	2	1	3
	4BT	2	2	4
	PPS	2	3.5	7
	DBT[c]	4	9	36

[a] The reaction was carried out with 0.5 mmol sulfide, 1.0 mmol H_2O_2 and 0.1 mol% **1b/2b** in 5 mL MeCN at 22 °C. [b] Time for complete conversion to sulfone. [c] 4 equiv. of H_2O_2 was used for the DBT reaction.
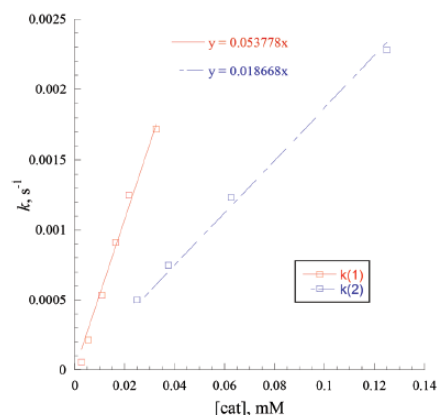

Fig. 3 Rate dependence on the concentrations of **1b** (red) and **2b** (blue) under pseudo-first order conditions.

shown in Fig. 4. Compound **1b** (blue solid, A) has a broad peak with a λ_{max} of 220 nm, while compound **2b** displays a sharper peak with a λ_{max} of 252 nm (red solid, C). Upon the addition of H_2O_2 (232 equiv.) to **1b** and a five min incubation time, the broad peak at 220 nm disappeared and a weaker, broader peak appeared at a λ_{max} of 330 nm (blue dash, B). Interestingly, the addition of H_2O_2 (232 equiv.) to **2b** only led to a slight intensification of the 252 nm peak, but no new features. Clearly, while both **1b** and **2b** catalyze oxygenation reactions efficiently, the active species generated in the presence of excess H_2O_2 are different. More importantly, the treatment of **1b** with excess H_2O_2 does *not* result in **2b** *in acetonitrile*.

Identification of intermediates though mass spectrometry

It became clear from both the kinetics and UV-vis studies that the active intermediate is not the same for **1b** and **2b**. Hence, the *in situ* nano-electrospray ionization mass spectrometric (nanoESI-MS) technique[29,30] was utilized to identify the active intermediate(s) for both $[1]^{6-}$ and $[2]^{6-}$ under three sets of experimental conditions: (I) **1b** and **2b** alone in acetonitrile; (II) **1b** and **2b** with H_2O_2 in large excess in acetonitrile and (III) **1b** and **2b** with MPS and H_2O_2 in large excess, *i.e.* the conditions of a typical catalytic reaction.

The negative mode ESI-MS spectrum of neat **1b** in acetonitrile (Fig. S1 in the ESI‡) features major ion fragments $[Mo_4O_{13}]^{2-}$ (m/z 295.9), $[Mo_3O_{10}]^{2-}$ (m/z 225.0) and $[Mo_5O_{16}]^{2-}$ (m/z 368.4), while the parent ion $[Mo_7O_{24}]^{6-}$ (m/z 175.9) was not detected. Previously, Walanda *et al.* studied the aqueous solution of isopolyoxomolybdates using ESI-MS and reported the omnipresence of the $[Mo_mO_{3m+1}]^{2-}$ type ions and the detection of parent ion $[Mo_7O_{24}]^{6-}$ at pH = 6.[31] Our detection of $[Mo_3O_{10}]^{2-}$, $[Mo_4O_{13}]^{2-}$ and $[Mo_5O_{16}]^{2-}$ despite the difference in solvent conditions indicates a similar fragmentation pattern of $[Mo_7O_{24}]^{6-}$ in acetonitrile. The absence of the parent ion peak likely reflects the fragility of $[Mo_7O_{24}]^{6-}$ in a non-aqueous

media. The negative mode ESI-MS spectrum of neat **2b** (Fig. S2 in the ESI‡) contains a noteworthy fragment corresponding to $[Mo_2O_{11}]^{2-}$ (m/z 183.8), and it does not display any of the significant ion fragment peaks identified for **1b**.

The negative mode ESI-MS spectrum of **1b** in the presence of 100-fold H_2O_2 was acquired to gain insight into the interaction between H_2O_2 and isopolymolybdate species, as well as the likely resultant species. Strikingly but unsurprisingly, most of the afore-mentioned $[Mo_mO_{3m+1}]^{2-}$ type ions vanished with $[Mo_4O_{13}]^{2-}$ remaining as the only observable member. The spectrum (Fig. 5a) features three main ions at m/z values of 183.8, 191.8 and 210.8, which correlate respectively to the $[Mo_2O_{11}]^{2-}$, $[HMoO_6]^-$ and $[H_3MoO_7]^-$. Interestingly, the $[Mo_2O_{11}]^{2-}$ ion (see Scheme 1) was previously prepared and characterized as an active catalyst for H_2O_2 oxygenation by our laboratory.[19] The appearance of both $[H_3MoO_7]^-$ (Scheme 1) and $[HMoO_6]^-$ is also noteworthy, as the former is a member

a)

Ion Observed	m/z	% BPI
$[Mo_2O_{11}]^{2-}$	183.8	100
$[HMoO_6]^-$	191.8	64.79
$[H_3MoO_7]^-$	210.8	37.56
$[Mo_4O_{13}]^{2-}$	295.9	16.74

b)

Ion Observed	m/z	% BPI
$[HMoO_6]^-$	191.8	31.66
$[H_3MoO_7]^-$	210.8	19.38
$[Mo_4O_{13}]^{2-}$	295.9	100
$[HMo_2O_{11}]^-$	369.9	49.41
$[Mo_6O_{19}]^{2-}$	440.3	11.69
$[HMo_3O_{10}]^-$	447.7	12.72
$[HMo_4O_{13}]^-$	591.6	10.06

Fig. 5 NanoESI mass spectra of **1b** (a) 1 min after the addition of H_2O_2; (b) 1 min after the addition of both H_2O_2 of MPS.
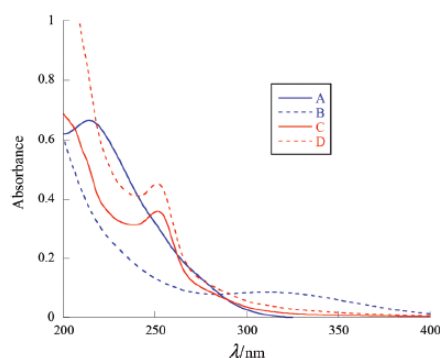

Fig. 4 Absorption spectra in acetonitrile of **1b** before (A, 1.75 mM) and after the addition of 232 equiv. of H_2O_2 (B); **2b** before (C, 3.27 mM) and after the addition of 232 equiv. of H_2O_2 (D).
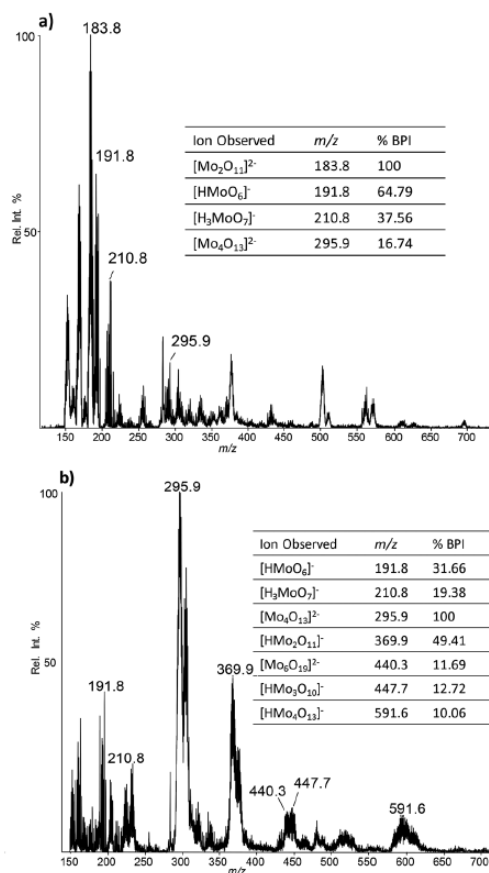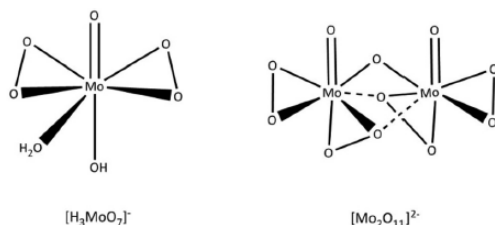
Dalton Transactions

$[H_3MoO_7]^-$ $[Mo_2O_{11}]^{2-}$

Scheme 1 Peroxy-intermediate derived from $[Mo_7O_{24}]^{6-}$.

of the Mimoun species, *i.e.* $M(=O)(\eta^2\text{-}O_2)_2(H_2O)_2$ (M = Cr, Mo and W),[32,33] and the latter is its dehydrated form. As shown in Fig. S3,‡ collision-induced dissociation (CID) of the ion at *m/z* 210.8 ($[H_3MoO_7]^-$) produced a loss of water (−18 Da), further corroborating the aforementioned assignments of $[HMoO_6]^-$ and $[H_3MoO_7]^-$. It is noteworthy that the $[Mo_2O_{11}]^{2-}$ peak also appeared in the ESI-MS spectrum of **2b** in the presence of H_2O_2 (Fig. S4‡), but in significantly reduced abundance (BPI = 32.7%). The *in situ* ESI-MS technique was finally extended to the catalytic oxygenation of MPS, namely a solution containing MPS and H_2O_2 in 1 : 1 mole ratio and 1 mol% of **1b**. Similar to the spectrum obtained in II, the predominant species observed are $[HMo_2O_{11}]^-$, $[HMoO_6]^-$ and $[H_3MoO_7]^-$ with respective BPIs of 49.4%, 31.7% and 19.4% shown in Fig. 5b. Interestingly, the most abundant species (BPI = 100%) from experiment III is $[Mo_4O_{13}]^{2-}$ (*m/z* 295.9), which is also present in spectrum II but at a much lower abundance (BPI = 16.7%, see Fig. 5a). For comparison purpose, ESI-MS spectrum of **2b** under catalytic conditions was also taken (Fig. S5‡), which reveals the presence of $[H_3MoO_7]^-$ and $[HMo_2O_{11}]^-$ similar to the case of **1b** at relatively low BPI percentages of 6.99 and 20.06%, respectively. This result indicated that the lower activity of **2b** is likely due to the insufficient production of $[Mo_2O_{11}]^{2-}$ ion.

Experimental

Materials and instrumentation

Acetonitrile, ammonium heptamolybdate tetrahydrate and guanidine hydrochloride were purchased from Sigma Aldrich. Tetra-*n*-butylammonium bromide was purchased from Alfa Aesar. Methyl phenyl sulfide, phenyl sulfide, benzyl phenyl sulfide, 4-bromothioanisole, phenylthioethanol and dibenzothiophene were purchased from ACROS Organics. Hydrogen peroxide (30%) was purchased from Macron Fine Chemicals and standardized *via* iodometric titration. Oxygenation reaction samples were analyzed using an Agilent 7890A GC system equipped with a flame ionization detector. The separation of substrate and products was achieved using an Agilent HP-5 column with dimensions of 30 m × 0.320 mm with 25 micron film thickness. Reaction progress was monitored at 290 nm *via* UV-Vis spectroscopy on a JASCO V-670 Spectrophotometer.

Synthesis of (*n*-Bu$_4$N)$_6$[Mo$_7$O$_{24}$] (1b)

Ammonium heptamolybdate tetrahydrate (500 mg, 0.405 mmol) was dissolved in water (4 mL). In a separate round bottom flask tetrabutylammonium bromide (0.789 g, 2.43 mmol) was dissolved in water (4 mL). The two solutions were mixed together and stirred for 10 minutes, with a white precipitate forming immediately. The precipitate was allowed to settle in the vial and collected by filtration and dried. Yield: 81% based on Mo.

Synthesis of (*n*-Bu$_4$N)$_6$[Mo$_7$O$_{22}$(O$_2$)$_2$]·*n*H$_2$O (2b)

Ammonium heptamolybdate tetrahydrate (2.472 g; 2.0 mmol) was dissolved in 20 mL water, to which were slowly added with stirring 2.0 mL 30% hydrogen peroxide (20 mmol) and tetrabutylammonium bromide (4.832 g, 15 mmol) in 10 mL water. After 30 min, the yellow precipitate was collected by filtering through a sintered glass filter, washed with 20 mL water, and air dried to afford powder samples 3.98 g of **2b** (yield 78% based on Mo). Elemental analysis calcd (%) for $C_{96}H_{216}N_6Mo_7O_{26}$: C, 45.4; H, 8.6; N, 3.3; Mo, 26.4. Found (%): C, 43.8; H, 9.0; N, 3.1; Mo, 25.6. IR for 1 (KBr, cm^{-1}): 3394 (s), 2964 (m), 2940 (m), 2874 (m), 1647 (m), 1483 (m), 1460 (m), 1381 (m), 1348 (w), 1281 (w), 1152 (w), 1158 (w), 1069 (w), 1030 (w), 1004 (w), 949 (m), 922 (s), 903 (s), 852 (s), 797 (vs), 730 (s), 657 (vs), 583 (s), 556 (s).

Catalytic conversion of sulfide

The catalyst (**1b/2b**) (0.005 mmol, 1 mol%) was dissolved in 5 mL of acetonitrile. Substrate sulfide (0.5 mmol) and internal standard 1,2-dichlorobenzene (0.4 mmol) were added to the reaction solution. H_2O_2 (1 mmol) was added to the solution drop wise, and the solution turned yellow. In the case of DBT additional equivalents of H_2O_2 (2 mmol total) were added in order to achieve complete conversion. Aliquots were taken at different time periods, quenched using MnO_2, and analyzed using GC.

Initial rate kinetics of 1b and 2b

Standard acetonitrile solutions utilized were prepared for **1b** at 1.75 mM, **2b** at 3.27 mM, MPS at 39 mM, and hydrogen peroxide at 0.37 M. Solutions for kinetic studies were prepared combining 200 μL of MPS and a specific volume of **1b** in a quartz cuvette, the volume of which was adjusted to 3.22 mL with additional acetonitrile. The reaction was initiated by the addition of 200 μL of the H_2O_2 stock solution. The absorbance of the solution at 290 nm was measured every 20 seconds for 30 minutes. The initial *in situ* concentrations upon the addition of H_2O_2 to the cuvette are 2.43 mM for MPS, 23 mM for H_2O_2, with a range of concentrations for **1b** (0.027–0.0326 mM) or **2b** (0.025–0.125 mM).

Nano-electrospray ionization mass spectra of 1b and 2b

For a typical measurement, a 5 mL solution of **1b** or **2b** (0.005 mmol in acetonitrile), 59 μL of MPS (0.5 mmol in aceto-nitrile) and 51 μL of H_2O_2 (0.5 mmol in acetonitrile) were com-

bined. These same concentrations and volumes were used for the neat **1b/2b** (Experiment I) and **1b/2b** plus H$_2$O$_2$ (Experiment II) spectra collected. An aliquot (5 μL) was removed and promptly diluted in 1 mL acetonitrile, then sprayed using a home-built nano-ESI source.[29] All ESI-MS experiments for **1b** were performed in the negative ion mode on a 4000 QTRAP triplequadrupole/linear ion trap mass spectrometer (Sciex, Toronto, Canada). The characteristic parameters of the MS during this study were set as follows: spray voltage, 1500 V; curtain gas, 5 psi; declustering potential (DP), 20 V. Mass analysis was achieved by using Q3 as a linear ion trap at a scan rate of 1000 Da s^{-1}. Data shown here were typically averages of 50 scans. ESI-MS experimental conditions for **2b** are provided in the ESI.‡ Data acquisition, processing, and instrument control were performed using Analyst 1.6 software.

Conclusions

It has been shown in this contribution that commodity chemical heptamolybdate is a highly efficient catalyst for hydrogen peroxide oxygenation of organic sulfides in terms of both the reaction rate and the hydrogen peroxide utility (100%). Electrospray ionization mass spectrometry studies revealed that the heptamolybdate ion undergoes significant fragmentation under the catalytic reaction conditions. One of the major ions detected in ESI-MS, [Mo$_2$O$_{11}$]$^{2-}$, has been identified as the main active species based on the consideration of catalytic rates. Our success herein will hopefully encourage further applications of ESI-MS and other MS techniques[34,35] in polyoxometallate catalysis.

Conflicts of interest

There are no conflicts to declare.

Acknowledgements

Notes and references

1 I. Fernandez and N. Khair, *Chem. Rev.*, 2003, **103**, 3651.
2 I. V. Babich and J. A. Moulijn, *Fuel*, 2003, **82**, 607–631.
3 Y.-C. Yang, *Acc. Chem. Res.*, 1999, **32**, 109–115.
4 G. W. Wagner and Y. C. Yang, *Ind. Eng. Chem. Res.*, 2002, **41**, 1925–1928.
5 K. Kim, O. G. Tsay, D. A. Atwood and D. G. Churchill, *Chem. Rev.*, 2011, **111**, 5345–5403.
6 R. A. Sheldon, I. Arends and U. Hanefeld, *Green Chemistry and Catalysis*, Wiley-VCH, Weinheim, 2007.
7 C. C. Romao, F. E. Kuhn and W. A. Herrmann, *Chem. Rev.*, 1997, **97**, 3197–3246.
8 S.-S. Wang and G.-Y. Yang, *Chem. Rev.*, 2015, **115**, 4893–4962.
9 I. V. Kozhevnikov, *Chem. Rev.*, 1998, **98**, 171–198.
10 C. L. Hill and C. M. Prossermccartha, *Coord. Chem. Rev.*, 1995, **143**, 407–455.
11 S. R. Livingston and C. C. Landry, *J. Am. Chem. Soc.*, 2008, **130**, 13214–13215.
12 S. R. Livingston, D. Kumar and C. C. Landry, *J. Mol. Catal. A: Chem.*, 2008, **283**, 52–59.
13 C. R. Ringenbach, S. R. Livingston, D. Kumar and C. C. Landry, *Chem. Mater.*, 2005, **17**, 5580–5586.
14 B. Zhang, S. Li, A. Pothig, M. Cokoja, S. L. Zang, W. A. Herrmann and F. E. Kuhn, *Z. Naturforsch., B: J. Chem. Sci.*, 2013, **68**, 587–597.
15 C. T. Buru, P. Li, B. L. Mehdi, A. Dohnalkoya, A. E. Platero-Prats, N. D. Browning, K. W. Chapman, J. T. Hupp and O. K. Farha, *Chem. Mater.*, 2017, **29**, 5174–5181.
16 K. E. Cantwell, P. E. Fanwick and M. M. Abu-Omar, *ACS Omega*, 2017, **2**, 1778–1785.
17 T. D. Phan, M. A. Kinch, J. E. Barker and T. Ren, *Tetrahedron Lett.*, 2005, **46**, 397–400.
18 D. Thompson, Y. Zhang and T. Ren, *J. Mol. Catal. A: Chem.*, 2014, **392**, 188–193.
19 D. J. Thompson, Z. Cao, E. C. Judkins, P. E. Fanwick and T. Ren, *Inorg. Chim. Acta*, 2015, **437**, 103–109.
20 F. A. Cotton and G. Wilkinson, *Advanced Inorganic Chemistry*, Wiley, 1988.
21 B. M. Trost and Y. Masuyama, *Isr. J. Chem.*, 1984, **24**, 134–143.
22 H. Y. Lu, C. L. Deng, W. Z. Ren and X. Yang, *Fuel Process. Technol.*, 2014, **119**, 87–91.
23 G. Absillis, E. Cartuyvels, R. Van Deun and T. N. Parac-Vogt, *J. Am. Chem. Soc.*, 2008, **130**, 17400–17408.
24 B. M. Trost and Y. Masuyama, *Tetrahedron Lett.*, 1984, **25**, 173–176.
25 V. S. Sergienko, *Crystallogr. Rep.*, 2008, **53**, 18–46.
26 M. C. Carreno, *Chem. Rev.*, 1995, **95**, 1717–1760.
27 Y.-C. Yang, *Acc. Chem. Res.*, 1998, **32**, 109–115.
28 K. Kamata, T. Hirano, R. Ishimoto and N. Mizuno, *Dalton Trans.*, 2010, **39**, 5509–5518.
29 M. Wilm and M. Mann, *Anal. Chem.*, 1996, **68**, 1–8.
30 P. Chen, *Angew. Chem., Int. Ed.*, 2003, **42**, 2832–2847.
31 D. K. Walanda, R. C. Burns, G. A. Lawrance and E. I. von Nagy-Felsobuki, *J. Chem. Soc., Dalton Trans.*, 1999, 311–321.
32 H. Mimoun, I. S. Deroch and L. Sajus, *Bull. Soc. Chim. Fr.*, 1969, 1481.
33 J. M. Bregeault, M. Vennat, L. Salles, J. Y. Piquemal, Y. Mahha, E. Briot, P. C. Bakala, A. Atlamsani and R. Thouvenot, *J. Mol. Catal. A: Chem.*, 2006, **250**, 177–189.
34 R. A. J. O'Hair, *Chem. Commun.*, 2006, 1469–1481.
35 R. A. J. O'Hair and G. N. Khairallah, *J. Cluster Sci.*, 2004, **15**, 331–363.